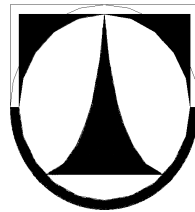


TECHNICAL UNIVERSITY OF LIBEREC
FACULTY OF MECHANICAL ENGINEERING
Department of Power Engineering Equipment



Experimental Investigation
of Synthetic Jets in a Laminar Channel Flow

Ph.D. Thesis
by Ing. Petra Dančová

Doctoral Degree Programme:
Applied Mechanics – Fluid mechanics and Thermomechanics

Supervisor:
Ing. Zdeněk Trávníček, CSc.

Supervisor specialist: Doc. Ing. Tomáš Vít, Ph.D.

DECLARATION OF AUTHORSHIP

I hereby confirm that the submitted work is entirely my own and was written only with help of referenced literature.

In Liberec, _____

Petra Dančová

ACKNOWLEDGMENTS

I would like to thank many people who helped me to prepare, write, and handle this thesis. Above all, I would like to thank my supervisor, Ing. Zdeněk Trávníček, CSc., for his help, advice, ideas, and consultations.

My thanks go to Doc. Ing. Tomáš Vít, Ph.D. for his help and advice, not only during the preparation of the experiments, but also for the patience he exhibited in answering my many questions.

I would like to thank Jaroslav Kneř and Petr Jerje for completing the experimental setup. My thanks also go to Ing. Michal Kotek, Ph.D. for his advice and assistance with the PIV system.

I would also like to thank Dr. ir H.C. de Lange for his kind supervision during my externship at the Eindhoven University of Technology in the Netherlands. Hierbij wil ik mijn vrienden uit Eindhoven bedanken.

Many thanks to all my colleagues and friends at the Technical University of Liberec, at the Institute of Thermomechanics of the Academy of Sciences of the Czech Republic, and at Warmnis, especially to Ing. Jiří Lenkvík.

Last but not least, none of this would have been possible without the support of my parents during my studies. Thank you.

This work has been supported by grants GAASCR (IAA200760801) and GA CR (P101/11/J019).

Petra Dančová

CONTENTS

Acknowledgement	5
Contents	7
Summary	9
Anotace (in Czech)	11
List of selected symbols	13
List of figures	17
CHAPTER 1: Introduction	19
1.1 Component tasks	19
1.1.1 Channel flow	19
1.1.2 Synthetic jet	23
1.1.3 Synthetic jet in cross flow	30
1.2 Motivation of the work	31
1.3 Aims of the work	31
1.4 Problem parameterization	32
CHAPTER 2: Experimental setup and methods	37
2.1 Experimental setup	37
2.1.1 Synthetic jet actuator	37
2.1.2 Tested channel for single synthetic jet actuator	38
2.1.3 Synthetic jet array setup	38
2.1.4 Circulation water channels	40
2.2 Signal (e.g. velocity) decomposition	41
2.2.1 Continuous sampling	41
2.2.2 Conditional sampling	41
2.2.3 Phase averaging	42
2.2.4 Time averaging	43
2.3 Experimental methods	44
2.3.1 Hot wire anemometry	44
2.3.1.1 Principle	44
2.3.1.2 Overheat ratio	46
2.3.1.3 Velocity calibration	46
2.3.1.4 Using HWA in water	47
2.3.1.5 HWA setup used	47
2.3.2 Laser Doppler vibrometry	47
2.3.2.1 Principle	47
2.3.2.2 Vibrometer parameters	48
2.3.3 Tin ion visualization	48
2.3.4 Particle image velocimetry	49
2.3.4.1 Principle	49
2.3.4.2 Images analysis	50
2.3.4.3 Laser and system synchronization	53
2.3.4.4 Setup parameters	54

2.3.5	Uncertainty analysis	54
2.3.5.1	Uncertainty of CTA measurements	54
2.3.5.2	Uncertainty of LDV measurements	57
2.3.5.3	Uncertainty of PIV measurements	57
2.3.5.4	Uncertainty of used measuring devices	58
CHAPTER 3:	Experimental results	61
3.1.	Channel flow	61
3.1.1	Channel flow using channel at TU/e (Eindhoven)	61
3.1.2	Channel flow using channel at IT CAS (Prague)	62
3.2.	Single synthetic jet	63
3.2.1	Frequency characteristic (using HWA)	64
3.2.2	Flow visualization using tin ion method	64
3.2.3	PCT behavior using laser Doppler vibrometry	65
3.2.4	HWA velocity measurement	66
3.2.5	PIV experiments of a single SJ in quiescent fluid	68
3.2.6	PIV experiments of a single SJ in a channel flow	68
3.3.	Synthetic jet array	75
3.3.1.	Synchronization of the piezoceramic system (using LDV)	75
3.3.1.1	Unselected piezoceramic transducers	75
3.3.1.2	Selected piezoceramic transducers – different power of SJ actuators	75
3.3.1.3	Selected piezoceramic transducers – similar power of SJ actuators	76
3.3.2.	Flow visualization of a SJ array using the tin ion method	76
3.3.3.	SJ array velocity measurement using HWA	77
3.3.4.	PIV experiments of a SJ array in quiescent fluid	78
3.3.5.	PIV experiments of a synthetic jet array in a channel flow	82
3.4	Overview of the main results	92
CHAPTER 4	Conclusions	95
4.1	Summary and evaluation of the work	95
4.2	Future work	97
REFERENCES		99
PUBLICATIONS OF AUTHOR		105
APPENDIX		107

SUMMARY

The thesis is focused on an impinging synthetic jet, namely on the case of a synthetic jet or a synthetic jet array interacting with a laminar channel flow. The thesis is mainly experimental.

The synthetic jet (SJ) was generated by the oscillating motion of the fluid. The fluid was periodically sucked into or pushed out of an actuator cavity. Vortex rings formed at the lip of the orifice. As these vortices developed and dissipated, the SJ took on the character of a conventional steady fluid jet when it was far enough from the end of the orifice. For the SJ actuator to operate optimally, it was important to find a driving frequency near the resonance, i.e. near the natural frequency of the pulsating fluid. An actuator, which works under these conditions, achieves the highest amplitude of fluid flow velocity at the same power. A typical feature of a SJ is that the time-mean mass flux through the nozzle is zero. Although the actuator works with zero time-mean mass flux, the momentum and the mass flux at a specific distance from the lip in the axis direction is non-zero. This feature of a SJ helps to place fluid sources anywhere without the need for piping. Another advantage, which is used in different applications, is the high value of turbulence intensity of a generated jet flow. This property is used mainly for heating or cooling.

This arrangement can be useful in many micro-scale applications, such as the cooling of microelectronics or the detection of various (biological, biomedical, or chemical) species. The flow regime on a micro-scale is usually laminar with very small Reynolds numbers; therefore, a SJ or SJ array can be used for profile disturbance and heat transfer enhancement.

The thesis focuses on low Reynolds numbers (in order 10^2). The channel was designed, manufactured, and tested. A piezoceramic transducer (PCT) was used as a moving membrane of the SJ actuator. The working fluid was water.

The thesis presents the following results:

- Design and construction of the tested equipment: a SJ actuator, device with a single SJ actuator, and a device with a SJ array.
- Determination of SJ actuator resonance frequency (theoretical analysis based on energy conservation and experimental evaluation by means of hot wire anemometry).
- Investigation of piezoceramic transducers (PCTs) by means of laser Doppler vibrometry (LDV). Design of well-synchronized SJs in the array.
Using LDV, the membrane centre velocity was measured and, consequently, diaphragm displacement was quantified. Considering continuity equation, the jet velocity was evaluated during the period. The results are in reasonable agreement (quite sufficient) with HWA experiments.
- Tin ion visualization to determine the basic character of the flow structure.
This method confirmed the proper functioning of SJ actuators, including their synchronization, before more complicated experiments (HWA and PIV) were performed.
- Hot wire anemometry (HWA) experiments for evaluating the resonance frequency and for measuring velocity profiles.
The HWA results of flow field velocity were used to select the correct PIV post-processing setting, namely for range validation. Particle image velocimetry (PIV) experiments on a channel flow, a single SJ, or SJ array in quiescent fluid or with affection of a channel flow.

Two PIV systems were used for the experiments – one at TU/e (Netherlands) and one at TUL.

The use of all these methods represented a complex approach to the problem. The main part of experiments were made using PIV. Moreover, many auxiliary experiments were also performed to find a properly functioning SJ actuator. The following paragraph outlines the experiments as performed consecutively.

After SJ actuator construction, it was important to find an actuator with a natural frequency, on which the SJ actuator could work with the highest velocity magnitude. Theoretically, the natural frequency can be found using HWA experiments. The first view of the SJ flow field was obtained using tin ion visualization. LDV helped to understand the behavior of the actuator membrane, and, in the case of the SJ array, it showed if all the PCTs were working in phase. HWA was also used for flow velocity measurement, with the results from this experiment being used for range validation in PIV post-processing. Thereafter, the main part of the experiments could be performed by means of PIV.

Keywords

Synthetic jet, synthetic jet array, active flow control, channel flow, actuator, piezoceramic transducer, particle image velocimetry, hot wire anemometry, laser Doppler vibrometry

ANOTACE

Disertační práce je experimentální a je zaměřena na vyšetřování případů, kdy jeden syntetizovaný proud či pole syntetizovaných proudů ovlivňuje laminární proudění v kanále.

Syntetizovaný proud (anglicky synthetic jet - SJ) je speciální případ turbulentního proudu, který je generován z periodických pulsací tekutiny, která je cyklicky vyfukována a nasávána vhodným otvorem (tryskou). Na okraji akčního členu se fázi vyfukování začínají tvořit vírové prstence. Vlivem disipativních procesů probíhajících v tekutině se tyto zprvu velmi zřetelné vírové struktury rozpadají a ve větší vzdálenosti od trysky se ztrácí periodický charakter proudění a proud tekutiny je svým charakterem velmi blízký stacionárnímu výtoku z trysky. Důležité pro optimální funkci SJ je provést konstrukci a zvolit budící frekvenci tak, aby zařízení pracovalo blízko rezonance, tj. zvolit frekvenci blízko vlastní frekvence pulzující tekutiny. Zařízení pracující v takovémto stavu dosahuje při stejném příkonu nejvyšší amplitudu rychlosti výtoku, a tak je hmotnostní tok tekutiny při daném výkonu maximální. Zařízení se vyznačuje generací proudu bez přívodu tekutiny. Ačkoliv je střední hmotnostní tok tryskou nulový, v dostatečné vzdálenosti od trysky jsou hmotnostní tok i hybnost proudu ve směru osy trysky nenulové. Tato vlastnost eliminuje potřebu potrubí pro přívod tekutiny a dává tak možnost mít proud tekutiny v zařízení k dispozici na právě požadovaném místě. Další z vlastností, která bývá využívána v aplikacích, je vysoká hodnota intenzity turbulence takto generovaného proudu tekutiny, což bývá využíváno hlavně při ohřevu či chlazení.

Takováto zařízení mohou být velmi dobře použitelná v různých aplikacích při rozměrech řádu mikrometrů, kdy režim proudění v kanálech mikro rozměrů je obvykle laminární s velmi nízkým Re . Tyto aplikace jsou např. chlazení mikro-elektroniky, použití v biologických, biomedicínkách či chemických odvětvích a v oblasti přenosu tepla/hmoty, např. chlazení nebo směšování.

Tato práce je zaměřena na nízká Reynoldsova čísla (v řádu 10^2). Pracovní látkou je voda. Jako periodicky se pohybující membrána akčního členu je použit piezokeramický měnič (piezoceramic transducer – PCT).

Práce obsahuje následující výsledky:

- Návrh a konstrukce testovacího zařízení: akční člen, zařízení se samostatnou tryskou SJ a zařízení s polem syntetizovaných proudů.
- Určení rezonanční (vlastní) frekvence akčního členu (teoretickým výpočtem ze zákona zachování energie a experimentem pomocí metody termoanemometrie).
- Vyšetřování chování a zřívání piezokeramických měničů pomocí metody laserové Dopplerovské vibrometrie (laser Doppler vibrometry - LDV). Nejprve je pomocí LDV změřena rychlost středu membrány PCT a z ní následně vypočten průhyb (posunutí) středu membrány. Pomocí rovnice kontinuity je z rychlosti membrány vypočtena střední rychlost syntetizovaného proudu. Tyto výsledky přijatelně souhlasí s výsledky přímého měření rychlosti v ose trysky pomocí termoanemometrie (hot wire anemometry - HWA).
- Nastínění základního charakteru proudění pomocí vizualizace metodou cínových iontů.
Pro pole syntetizovaných proudů ukazuje, že trysky SJ pracují ve stejné fázi a navzájem se ovlivňují. Zároveň je vizualizace použita jako příprava pro složitější experimenty HWA a PIV.

- Experimenty pomocí metody žhaveného drátku (HWA) pro určení rezonanční (vlastní) frekvence akčního členu a měření rychlostních profilů.
Kromě toho, měření rychlosti pomocí HWA slouží pro správné nastavení parametrů experimentů PIV – především funkce „range validation“ v programu DynamicStudio v.2.30, DANTEC (PIV post-processing).
- Particle image velocimetry (PIV) pro měření neovlivněného kanálového proudění a proudění v kanále, které je ovlivňováno syntetizovaným proudem, popř. polem těchto proudů.
Experimenty jsou provedeny dvěma PIV systémy, systém používaný na TU/e (Nizozemí) a systém používaný na TUL.

Použití výše uvedených metod představuje komplexní přístup k řešení problému. Hlavní experimenty byly provedeny metodou PIV. Pro celkové pochopení problému a jeho správné řešení však bylo nutné provést i mnoho dílčích a pomocných měření. V následujícím odstavci jsou experimenty uvedeny postupně tak, jak byly prováděny a proč, nikoliv v závislosti na jednotlivých metodách.

Po návrhu a výrobě akčního členu SJ je důležité zjistit jeho vlastní frekvenci, při které akční člen pracuje s nejvyšší amplitudou rychlosti proudu. Vlastní frekvenci je možné zjistit teoreticky a zároveň experimentálně, např. s použitím metody HWA. Prvotní představu o syntetizovaném proudu lze získat pomocí vizualizace metodou cínových iontů. Metodou laserové Dopplerovské vibrometrie lze zjistit chování piezokeramického měniče použitého jako pohybující se membrána akčního členu. Pro pole syntetizovaných proudů je LDV použita pro zjištění, zda piezokeramické měniče pracují ve fázi. Metoda HWA je použita pro zjištění rychlostních profilů a zároveň poslouží pro PIV post-processing při použití funkce „range validation“. Po těchto přípravných experimentech již bylo možno provést hlavní experimenty pomocí metody PIV.

Klíčová slova

Syntetizované proudy, pole syntetizovaných proudů, aktivní řízení proudění, proudění uzavřeným kanálem, akční člen, piezokeramický měnič, particle image velocimetry, metoda žhaveného drátku (hot wire anemometry), laserová Dopplerovská vibrometrie (laser Doppler vibrometry)

LIST OF SELECTED SYMBOLS

A, B, C, D	[1]	calibration constant
A	[m ²]	area
a_h	[1]	overheat ration; $a_h = R_{\text{wire}} / R_{\infty}$
A_m	[m ²]	area of the membrane
B	[m]	the channel width (Fig. 2.4)
b	[m]	width
C, c	[1]	constant
c	[m.s ⁻¹]	sound speed
c_p	[J.kg ⁻¹ K ⁻¹]	specific isobaric heat capacity
c_U, c_Q, c_M	[1]	ratio of velocities, flow rates, and momentum
D	[m]	diameter of the actuator orifice
d	[m]	diameter
D_{CH}	[m]	hydraulic diameter of the channel
D_D	[m]	cavity diameter
D_m	[m]	diameter of the membrane
dx	[m]	elementary length
d_{wire}	[m]	diameter of the wire (in HWA)
E	[J]	total energy
E	[V]	voltage
E_k	[J]	kinetic energy
E_p	[J]	potential energy
E_{wire}	[V]	voltage in a wire
F	[N]	force
F_p	[N]	pressure force
F_t	[N]	frictional force
f	[Hz]	frequency
f_D	[Hz]	Doppler frequency
$f(x)$		function of x
H	[m]	the channel height (Fig. 2.4)
h	[m]	height
I	[A]	electric current
k_p	[N.m ⁻³]	stiffness of the membrane
L	[m]	length
L_e	[m]	equivalent length; $L_e = L + (8D) / (3\pi)$
L_0, L_{0A}	[m]	“stroke length” – Eq. (1.14)
k, l	[m]	pixel position
l_{wire}	[m]	length of the hot wire
m	[1]	constant
M	[kg.m.s ⁻²]	momentum flux
n	[1]	calibration exponent in King’s law
n	[1]	constant
N	[1]	number of acquired periods
p	[Pa]	pressure
p	[Pa]	static pressure
P	[W]	electric power
\dot{Q}	[W]	heat flux

\dot{Q}_{ac}	[W]	accumulated heat flux
\dot{Q}_{cond}	[W]	conductive heat flux
\dot{Q}_{conv}	[W]	convective heat flux
\dot{Q}_J	[W]	heat flux generated on a wire
\dot{Q}_{rad}	[W]	heat radiated into surroundings
\dot{Q}	[kg.s ⁻¹]	mass flux
R, r	[m]	radius
R_0	[Ω]	resistance of wire at 0°C
R_{20}	[Ω]	resistance of wire at 20°C
R_{wire}	[Ω]	wire resistance
R_{∞}	[Ω]	resistance of wire at ambient temperature T_{∞}
$S_{u,CT}$	[V.m ⁻¹ .s]	CT mode velocity sensitivity
$S_{\theta,CT}$	[V.K ⁻¹]	CT mode temperature sensitivity
S_{wire}	[m ²]	wire cross-section
t	[s]	time
t	[s]	time in the period; the origin ($t = 0$) is chosen at the beginning of the extrusion stroke
T	[s]	time period
T	[K]	temperature
T_{wire}	[K]	wire surface temperature
T_{∞}	[K]	ambient temperature
T_0	[K]	ambient reference temperature
U_0, U_{0A}	[m.s ⁻¹]	time-mean orifice velocity of SJ – Eq. (1.13)
U, u, v	[m.s ⁻¹]	velocity
V	[m ³]	volume
\dot{V}	[m ³ .s ⁻¹]	volume flux
x, y, z	[m]	coordinate system
y	[m]	water level height
z	[m]	membrane displacement

Greek symbols

α	[W.m ⁻² .K ⁻¹]	heat transfer coefficient
α	[°, rad]	angle
θ	[°, rad]	angle
λ	[m]	wavelength
μ	[Pa.s]	dynamic viscosity
ν	[m ² .s ⁻¹]	kinematic viscosity
ρ	[kg.m ⁻³]	density
τ	[Pa]	shear stress
χ_{wire}	[Ω.m]	specific resistance of wire material
ω	[rad.s ⁻¹]	rotating velocity

Abbreviations

A/D		analog/digital
CC		constant current
CCD		charge-coupled device
CT		constant temperature
CTA		constant temperature anemometry
FFT		fast Fourier transformation
HWA		hot wire anemometry
LDV		laser Doppler vibrometry
MEMS		micro-electro-mechanical systems
PCT		piezoceramic transducer
PIV		particle image velocimetry
SJ		synthetic jet
ZNMF		zero-net-mass-flux
Nu	[1]	Nusselt number
Re	[1]	Reynolds number
Re _{SJ}	[1]	Reynolds number of a synthetic jet – Eq. (1.15)
Re _C	[1]	Reynolds number of a channel flow - Eq. (1.32, 1.33)
St	[1]	Strouhal number
1D		one dimensional
2D		two dimensional
3D		three dimensional

Subscripts

C	channel
E	extrusion
j	jet
k	kinetic
M	mean
M	momentum
m	membrane
max	maximal
min	minimal
p	periodic
p	potential
rms	root-mean-square value
Q	flow rate
U	velocity
∞	surroundings

Superscripts

'	fluctuation component
---	-----------------------

LIST OF FIGURES

1.1	(a) Velocity profiles of developed channel flow, (b) Developed and developing laminar flow	19, 20
1.2	Laminar flow between parallel walls	21
1.3	A rectangular duct	22
1.4	Basic principle of SJ	24
1.5	Creation of vortex rings by fluid extrusion from the cavity of an actuator	24
1.6	One of the working cycles of a SJ	24
1.7	Fluid flow vectoring by a SJ	25
1.8	Schematics of the synthetic jet control module	25
1.9	Using a SJ to increase lift force on a wing profile	26
1.10	Wake past a bluff body in form of x velocity	27
1.11	Principle of an impinging jet	29
1.12	Principle of valveless pump	29
1.13	Double-acting hybrid SJ actuator	30
1.14	Schematic view of the formulation of the time-mean velocity U_0	32
2.1	SJ actuator	37
2.2	Piezoceramic transducer	38
2.3	Tested channel	38
2.4	Schematic view of the present configuration	39
2.5	Horizontal projection (a) single SJ, (b) SJ array	39
2.6	SJ array equipment	39
2.7	Schematic view of the water channel at TU/e	40
2.8	(a) Circulation channel at IT CAS, (b) drawing of circulation channel at IT CAS	40
2.9	(a) Continuous sampling: acquired CTA and TTL signals, (b) acquired signal divided into N individual periods, (c) time-mean depended signal	41
2.10	Schematic of conditional sampling	42
2.11	SJ phase average of 100 periods in $t/T = 0.25$	43
2.12	Schematic view of HWA (CT) measurement	44
2.13	Wheatstone bridge for anemometer operating in CT mode	46
2.14	Schematic drawing of visualization	49
2.15	Principle of PIV measurement	49
2.16	Interrogation areas	49
2.17	Graphical presentation of autocorrelation	50
2.18	Graphical presentation of cross-correlation	50
2.19	Computation of vector map with use of FFT	51
2.20	Principle of interrogation areas overlap	52
2.21	Unit <i>Timer box</i> with signals for laser and camera	53
2.22	Schematic of basic synchronization for PIV measurement	53
3.1	Visualization of the laminar channel flow at Reynolds number $Re_c = 480$	62
3.2	Velocity profile of a channel flow without SJ	62
3.3	(a) Velocity profile of a channel flow without SJ, (b) PIV results of velocity laminar profile in the form of velocity magnitude vectors	62, 63
3.4	Comparison of channel velocity profiles from TU/e and IT CAS	63
3.5	Velocity profile of a channel flow without a SJ	63
3.6	(a) Frequency characteristic of a SJ actuator, (b) detailed view	64

3.7	Tin ion visualization of a single SJ	65
3.8	Results of LDV measurement of the oscillating membrane center. Phase shift between LDV membrane center velocity measurement and its position calculation, TTL and driving sinusoidal signal	65
3.9	Oscillating membrane center: (a) LDV measured velocity, (b) calculated displacement	66
3.10	Results of CTA experiments: (a) dependence of the phase-averaged velocity magnitude at different instances in the period and of the time-mean velocity on the distance from the actuator orifice, (b) dependence of the time-mean velocity on the distance from the orifice on a logarithmic scale	67
3.11	Phase-averaged velocity magnitude profiles and time-mean velocity magnitude profile at distance $y/D = 1.5$	68
3.12	(a) Single SJ – vectors of the phase-averaged velocity magnitude, (b) single SJ – contours of the phase-averaged velocity magnitude	69, 70
3.13	Phase-averaged velocity magnitude profiles of a single SJ during the actuation cycle	71
3.14	Velocity magnitude contours of the channel flow interacting with a single SJ. Phase-averaged for $t/T = 0.25$	72
3.15	Phase-averaged velocity magnitude profiles of channel flow interaction with a single SJ, $t/T = 0.25$	73
3.16	Unselected PCT - oscillating membrane center in time (a) measured velocity, (b) calculated displacement	74
3.17	Selected PCT, different power - oscillating membrane center in time (a) measured velocity, (b) calculated displacement	74
3.18	Selected PCT, similar power - oscillating membrane center in time (a) measured velocity, (b) calculated displacement	74
3.19	Tin ion visualization of a SJ array in quiescent water on plane III	76
3.20	Dependence of the phase-averaged velocity magnitude at different instances in the period and of the time-mean velocity magnitude on the distance from the SJ array actuator orifices	77
3.21	Dependence of the time-mean velocity magnitude on the distance from the SJ actuator orifices on a logarithmic scale	78
3.22	Phase-averaged velocity magnitude profiles and time-mean velocity magnitude profile at distance $y/D = 0.5$	79
3.23	Phase-averaged velocity magnitude profiles and time-mean velocity magnitude profile at distance $y/D = 1.5$	79
3.24	SJ array – contours in discrete drawing style and vectors of the phase-averaged velocity magnitude	80, 81
3.25	Phase-averaged velocity magnitude profiles of a SJ array during the actuation cycle at $y/D = 1.5$	82
3.26	Phase-averaged velocity magnitude profiles of a SJ array at the instant of maximum extrusion velocity	83
3.27	Velocity magnitude contours of the channel flow interacting with a SJ array	84, 85
3.28	Phase-averaged velocity magnitude profiles of the channel flow measured in the plane of SJ 1	86
3.29	Phase-averaged velocity magnitude profiles of the channel flow measured in the plane of SJ 2	87, 88
3.30	Phase-averaged velocity magnitude profiles of the channel flow measured in the plane of SJ 3	89
3.31	Phase-averaged velocity magnitude profiles of the channel flow measured in the plane of SJ 4	90
3.32	SJ array – contours in discrete drawing style of the phase-averaged velocity magnitude on plane I	91

CHAPTER 1

INTRODUCTION

This thesis deals with synthetic jets, namely with a synthetic jet and a synthetic jet array in a channel flow. The research is focused on low Reynolds numbers. Chapter 1 describes the terms “channel flow”, “impinging jet”, and “synthetic jet”. It also incorporates historical contents, the state of the art, and the aims of this work.

The motivation behind this work is to demonstrate an arrangement in which a SJ or a SJ array interacting with a laminar channel flow can be useful for micro-scale applications, such as cooling in micro-electronics. The flow regime in micro-scale is usually laminar with very small Reynolds numbers and cooling is typically based on gradient diffusion. Therefore, this study focuses on low Reynolds numbers; more specifically, current Reynolds numbers are so low that they cannot initiate a transition to turbulence. Therefore, a SJ/SJ array is used as a disturbance of laminar channel flow. A potential application of this method is to increase heat transfer using the flow control of a main flow, as discussed in paragraph 1.1.2 below.

A Reynolds number of a channel flow is assumed for 2D simplification.

1.1. COMPONENT TASKS

1.1.1 CHANNEL FLOW

As is mentioned above, this work focuses on low Reynolds numbers. In other words, on the laminar channel flow. The flow of real fluid is supposed (the fluid has internal friction and the surrounding fluid elements interact with frictional force). The real flow can be laminar or turbulent. In a laminar case, fluid elements move in layers without transfer through a cross section (of a channel or assumed stream tube). On the other hand, fluid elements in a turbulent flow have a fluctuation velocity, which enables moving through the cross section (of the channel or assumed stream tube), [1].

Laminar flow in a channel can be shown in the Reynolds test: Colored fluid is put into a running flow. At low velocities, the color fiber stays intact – this implies that the fluid elements move in layers. At increased velocity (over a critical value), the fluid elements start to become highly mixed. The fluid elements continuously move from one layer to another, exchanging kinetic energy. Therefore, velocities through the cross section start

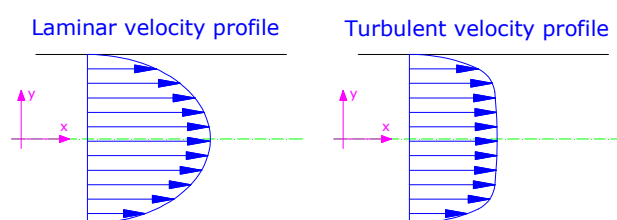


Fig.1.1a Velocity profiles of developed channel flow

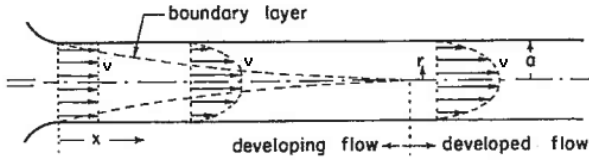


Fig.1.1b Developed and developing laminar flow, [80]

to be more flat. Due to the movement of the fluid elements, the momentum changes, resulting in higher movement resistance than that experienced in laminar flow. Laminar and turbulent flows have different velocity profiles and different hydraulic losses. In laminar channel flow, the velocity profile is

parabolic (see Figure 1.1a). In turbulent channel flow, the velocity profile is more flat, [1].

Laminar flow in a two-dimensional stationary straight duct is designated as hydrodynamically fully developed (or established) when the fluid velocity distribution at a cross section is of an invariant form, i.e. independent of the axial distance x (as shown in Figure 1.1b) $v = v(y,z)$. The fluid particles move in definite paths called streamlines, and there are no components of fluid velocity normal to the duct axis. In a fully developed laminar flow, the fluid appears to move by sliding laminae of infinitesimal thickness relative to adjacent layers. Depending upon the smoothness of the tube inlet and the inside wall of the tube, a fully developed laminar flow persists up to $Re \leq 2300$ for a duct length L greater than the hydrodynamic entry length L_{hy} , [80].

The hydrodynamic entrance region of the duct is where the velocity boundary layer develops; for example, from zero thickness at the entrance to a thickness equal to the pipe radius far downstream. In this region, the fluid velocity profile changes from the initial profile at the entrance to an invariant form downstream. The flow in this region, as a result of the viscous fluid behavior, is designated as hydrodynamically developing (or establishing) flow, as also shown in Figure 1.1b, [80].

The hydrodynamic entrance length L_{hy} is defined as the duct length required to achieve a maximum duct section velocity of 99% of that for fully developed flow when the entering fluid velocity profile is uniform. The maximum velocity occurs at the centroid for the ducts symmetrical about two axes (e.g. circular tube and rectangular ducts). The L_{hy} is a function of the Reynolds number. For example, a two-dimensional case of low flow between parallel walls can be correlated [80] as

$$\frac{L_{hy}}{D_{CH}} = \frac{0.315}{0.0175 Re + 1} + 0.011 Re \quad (1.1)$$

where D_{CH} is the hydrodynamic diameter, $D_{CH} = 2H$.

Laminar channel flow

A) Two-dimensional case of two parallel walls

Between two parallel walls (a 2D simplification of this work), the laminar channel flow in a horizontal direction is created with a pressure drop $\Delta p = p_1 - p_2$. When flow is created with a pressure drop (pressure difference) over the distance l , the specific pressure drop i is constant, [1]:

$$i = \frac{\Delta p}{l} = \frac{dp}{dx} = const. \quad (1.2).$$

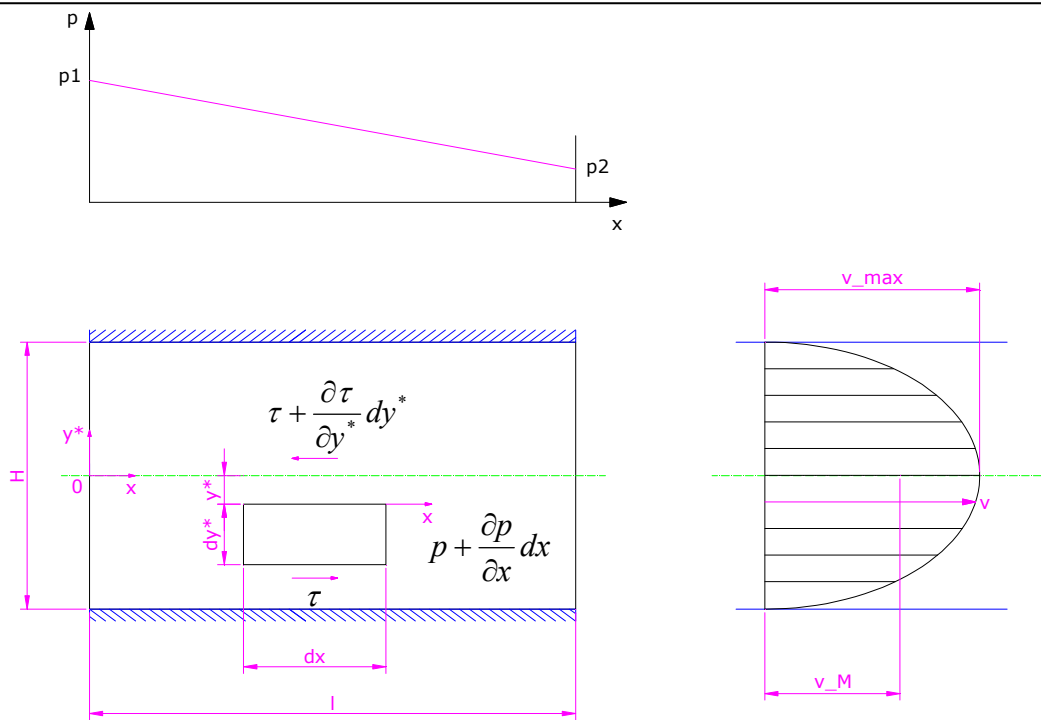


Fig.1.2 Laminar flow between parallel walls

An isotherm flow with constant viscosity is assumed. The balance of forces for the element of the developed channel flow is expressed by means of pressure (F_p) and frictional forces (F_t) (see Figure 1.2):

$$dF_p = pb dy^* - \left(p + \frac{\partial p}{\partial x} dx\right) b dy^* \quad (1.3a, b),$$

$$dF_t = \tau b dx - \left(\tau + \frac{\partial \tau}{\partial y} dy^*\right) b dx$$

where b is unit width, p is pressure, and τ is shear stress [Pa], [1].

The balance can be written as $dF_p + dF_t = 0$, which can be rearranged as:

$$\frac{\partial p}{\partial x} + \frac{\partial \tau}{\partial y^*} = 0 \quad (1.4a).$$

By means of replacing partial derivations with total derivations (since $\tau = \tau(y^*)$, $p = p(x)$) and with Equation (1.2), the Equation (1.4a) can be written as:

$$\frac{d\tau}{dy^*} = -i \quad (1.4b, c),$$

$$\tau = -iy^* + C$$

In a slot axis ($y^* = 0$), the velocity is maximal and shear $\tau = 0$, the constant of integration $C = 0$.

With substitution of $\tau = \eta \frac{dv}{dy^*}$ into Equation (1.4c), after integration, the velocity in a slot is evaluated as:

$$v = \frac{1}{\eta} \left(-\frac{i}{2} y^{*2} + C y^* + C_1 \right) \quad (1.5a).$$

Constants of integration C and C_1 are set by boundary conditions. On walls, the flow velocity is zero, i.e. for $y^* = \frac{H}{2}$ and $y^* = -\frac{H}{2}$ is $v = 0$, then $C = 0$ and $C_1 = \frac{iH^2}{8}$. Then Equation (1.5a) is written as:

$$v = \frac{i}{2\eta} \left[\left(\frac{H}{2} \right)^2 - y^{*2} \right] \quad (1.5b).$$

Velocity profile is parabolic (see Figure 1.2), [1].

Flow rate through the slot is determined by the integration of Equation $d\dot{V} = v b dy^*$ over the channel cross section $H \times b$, in which Equation (1.5b) is inserted:

$$\dot{V} = \frac{ib}{2\eta} \int_{-H/2}^{H/2} \left[\left(\frac{H}{2} \right)^2 - y^{*2} \right] dy^* = \frac{ib}{12\eta} H^3 \quad (1.6).$$

The average velocity v_M (averaged across the channel cross section) is defined from the equality $\dot{V} = b H v_M$, therefore $v_M = \frac{i}{12\eta} H^2$. The maximal velocity v_{max} is calculated from

Equation (1.5b) for $y^* = 0$, then $v_{max} = \frac{i}{8\eta} H^2$.

Ratio of mean and maximal velocity is:

$$\frac{v_M}{v_{max}} = \frac{2}{3} \quad (1.7).$$

B) Three-dimensional case

Consider the cross section of a rectangular duct, characterized by its aspect ratio $\alpha^* = 2b/2a$, see Figure 1.3, with flow direction along the x axis (perpendicular to the plane of paper), [80].

The velocity profile, provided by the solution of Equation $\frac{\partial^2 v}{\partial y^{*2}} + \frac{\partial^2 v}{\partial z^2} = c_1$ with the boundary condition

$v = 0$ on the walls, is:

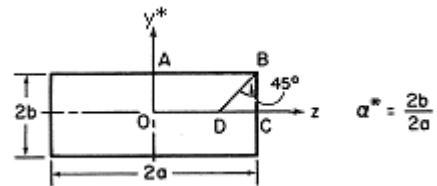


Fig.1.3 A rectangular duct

$$v = -\frac{16c_1 a^2}{\pi^3} \sum_{n=1,3,\dots}^{\infty} \frac{1}{n^3} (-1)^{(n-1)/2} \left[1 - \frac{\cosh(n\pi y^* / 2a)}{\cosh(n\pi b / 2a)} \right] \cos\left(\frac{n\pi z}{2a}\right) \quad (1.8),$$

$$v_M = -\frac{c_1 a^2}{3} \left[1 - \frac{192}{\pi^5} \left(\frac{a}{b}\right) \sum_{n=1,3,\dots}^{\infty} \frac{1}{n^5} \tanh\left(\frac{n\pi b}{2a}\right) \right] \quad (1.9).$$

Since Equation (1.8) involves considerable computational complexity, in [80] a simple approximation in the following form for the aspect ratio $\alpha^* \leq 0.5$ is proposed:

$$\frac{v}{v_{\max}} = \left[1 - \left(\frac{y^*}{b}\right)^n \right] \left[1 - \left(\frac{z}{a}\right)^m \right] \quad (1.10),$$

where $m = 1.7 + 0.5(\alpha^*)^{-1.4}$ and $n = 2$ for $\alpha^* \leq 1/3$ or $n = 2 + 0.3(\alpha^* - 1/3)$ for $\alpha^* \geq 1/3$.

The integration of Equation (1.10) over the duct cross section yields:

$$\frac{v}{v_M} = \left(\frac{m+1}{m}\right) \left(\frac{n+1}{n}\right) \left[1 - \left(\frac{y^*}{b}\right)^n \right] \left[1 - \left(\frac{z}{a}\right)^m \right] \quad (1.11),$$

$$\frac{v_{\max}}{v_M} = \left(\frac{m+1}{m}\right) \left(\frac{n+1}{n}\right) \quad (1.12).$$

For channels used in this work, $\frac{v_{\max}}{v_M} = 1.73$, $\frac{v_M}{v_{\max}} = 0.58$ respectively, where $\alpha^* = 0.2$.

The problem is also described in [81, 82, and 83].

1.1.2 SYNTHETIC JET

A synthetic jet (SJ) is generated by the periodic motion of an actuator oscillating membrane. A SJ is synthesized by the interactions within a train of vortex rings or counter-rotating vortex pairs in axis-symmetric or two-dimensional geometry; see Smith and Glezer [4]. Vortex rings are formed at the lip of the orifice (see Figures 1.4 and 1.5). These rings move in y direction with a velocity, which must be high enough to prevent interaction with suction in the orifice. It was observed that an SJ far enough from the orifice has a character of a conventional steady jet. This is caused by the development and dissipation of vortices. One of the main advantages of a SJ is that the time-mean mass flux of the oscillatory flow in the orifice is zero; hence the other common expression is a zero-net-mass-flux (ZNMF) jet. A ZNMF eliminates the requirement of a blower and piping for the fluid inlet. Though the SJ actuator works with a ZNMF at the orifice, the momentum of the resultant SJ at a specific distance from the lip in y is non-zero [4-6].

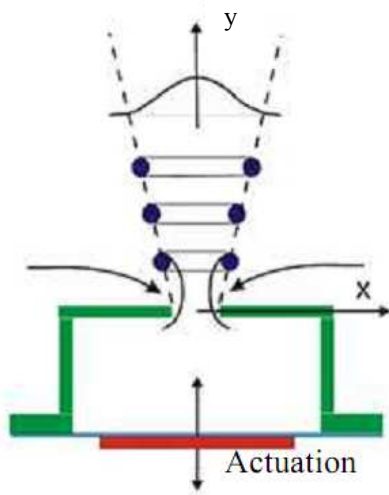


Fig.1.4 Basic principle of SJ

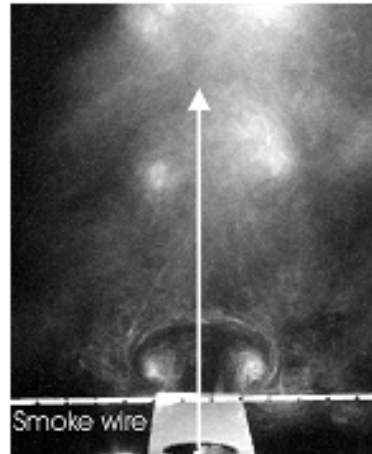


Fig.1.5 Creation of vortex rings by fluid extrusion from the cavity of an actuator. Results of “smoke wire” visualization [A2]

The equipment for a SJ can have various designs, but the main mechanism and principle is primarily the same. Figure 1.4 shows the simplest setting: There is an orifice at one end of the actuator, whereby the fluid is periodically sucked/exhausted to/from an actuator cavity. The pulsation generator of the fluid can work on the principle of loudspeaker, piezo crystal, electromagnet, piston, or other device. It is necessary to choose an optimal type and construction of actuator in relation to the supposed working frequency range, working temperature, kind of working medium, and required load of the unit.

Figure 1.6 shows details of the working cycle of a SJ. The working cycle starts with a diaphragm motion from its zero position (position $0a$) in $-y$ direction. This motion causes fluid movement into an actuator cavity. If the diaphragm deviation is maximum (position 1), the fluid is extruded from the orifice of an actuator. The highest velocity of extrusion is when the diaphragm experiences zero deviation (position $0b$). Then the diaphragm moves in $+y$ direction to position 2 . When the diaphragm reaches position 2 , the fluid is sucked in again, and the cycle is repeated.

The first pilot projects about the problems of SJ began before the term SJ was even established. One of the first successful applications was already described 50 years ago:

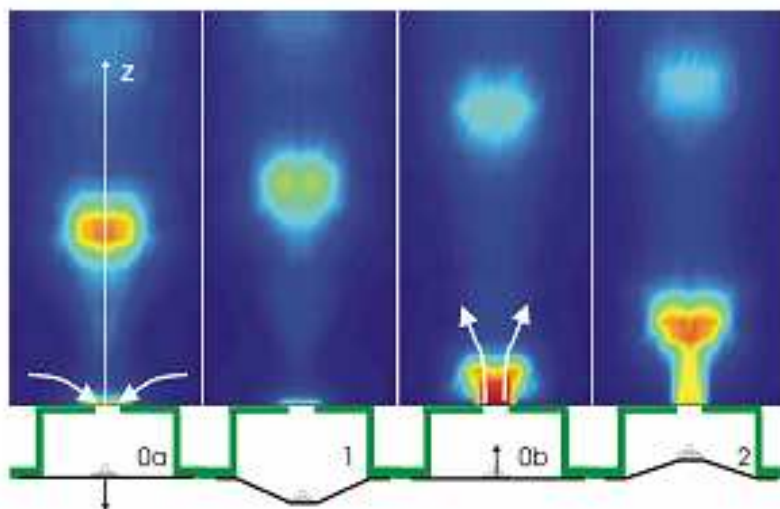


Fig.1.6 One of the working cycles of a SJ. Experimental results measured by CTA with an X-wire probe. $2 \rightarrow 0a \rightarrow 1$ suction; $1 \rightarrow 0b \rightarrow 2$ extrusion. Colorized according to the velocity magnitude [A1]

Dauphinee [7] used an oscillating membrane for air jet creation in calibration equipment for a temperature probe. The heat transfer on the wall in the presence of a SJ and the boundary layer control using a SJ are described in articles [8 and 9].

The creation of fluid jets by means of pulsating pistons was published by e.g. Mednikov and Novitskii [10] and Tesař [11, 12]. Closely related phenomena are the so-called “acoustic streaming”, see Meissner [13] and Lighthill [14], flows caused by oscillating bodies (Stuart [15]; Davidson and Riley [16]), and flows created by acoustic waves – either by standing (Ingard [17]) or traveling (Lebedeva [18]) ones.

Research linked to the problems of oscillating flow and acoustic streaming became a topic of intensive research at the end of 20th century. The English term “Synthetic Jet” was introduced by R.D. James, J.W. Jacobs, A. Glezer: A round turbulent jet produced by an oscillating diaphragm, *Phys. Fluids*, Vol. 8, No. 9 (1996), 2484–2495, [84].

The term “Synthetic Jet” is translated to the Czech language as “*Syntetizovaný proud*”. This term was suggested in 2001 [19, research report] and published in 2002 [20, journal paper] for the first time.

A SJ has many significant applications and the number of applications is increasing all the time. The most important applications can be divided into two main groups:

- I. Main (primary) flow control.
- II. The use of a stand-alone SJ or a system of synthetic jets.

I. Main (primary) flow control

I.1 Jet vectoring

This category of applications includes the control of flow, which is parallel or perpendicular to the driving jet. Figure 1.7 shows the principle of jet vectoring. Figure 1.7a shows the case with an activated SJ when the main flow is deflected from its direct course and falls into a so-called collector by which the flow leaves away. If the SJ is inactive, the main flow is not affected by the SJ and continues on a direct course (Figure 1.7b). This principle can be used, for example, in air distributors. In this case, the SJ equipment is driven electrically, and it is possible to vector substantial flow volumes without the need for complicated mechanical components. Details on this application of a

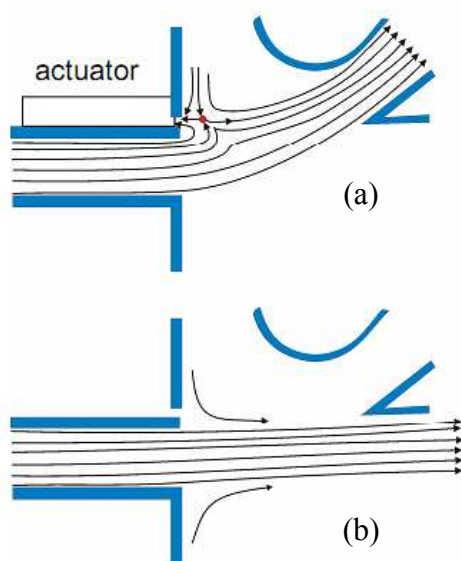


Fig.1.7 Fluid flow vectoring by a SJ, (a) activated SJ, (b) closed SJ, Smith and Glezer, [21]

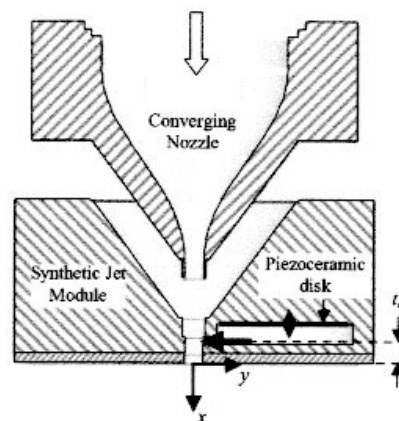


Fig. 1.8 Schematics of the synthetic jet control module, [23]

SJ are described in [21, 22].

Tamburelo and Amitay [23] investigated the effect of the upstream location of a synthetic jet inside the nozzle of a main jet. Synthetic jet actuators (see Figure 1.8) were used to manipulate the downstream development of a free jet by capitalizing both on the direct impact (similar to continuous control jets) of the synthetic jet and the manipulation of large-scale, global instabilities within the main jet flow (due to their near-field periodic flow field) [23].

I.2 Flow field control in external aerodynamics

SJs can be used to control turbulence, boundary layer separation, and drag reduction, as well as to increase lift force and/or enable noise suppression [24, 25]. An interesting application is a concept incorporated in the Renault Altica sports car [26], which was presented at the 2006 Geneva Motor Show. A SJ was used to reduce drag force and thereby decrease fuel consumption. This SJ equipment, which consists of slot for air outflow and air sucking from surroundings, is integrated on the roof of the Renault Altica close to the trailing edge. The designers of this car concept presume a very optimistic fuel consumption reduction of around 15 percent, whereas the SJ equipment power requirement is only 10 W [26]. Further applications of SJs can be found on airfoils [27] (Figure 1.9) or propellers of helicopters; some of these examples are inscribed as a “virtual shaping effect” of an airfoil [28, 29].

Recently, the so-called “smart control” of airfoil shape came under intensive discussion. This equipment allows the main characteristics of the airfoil to be adapted to instantaneous conditions in the boundary layer or to the requirements of an external control unit. It is possible to improve airfoil parameters and system maneuverability or to simplify or completely remove mechanical control systems from the wings. These technologies are perspective in small and very small pilotless planes (Micro Air Vehicle MAV, Unmanned Aerial Vehicle UAV), and eventually in analogous underwater vehicles (Autonomous Underwater Vehicle [30]).

Another possible application of SJs aims to improve the properties of the propeller wind turbines (recently analyzed at IT CAS). The main objective of this research is to increase the lift to drag ratio and to decrease aerodynamic noise [31, 32, and 33].

The influence of a SJ on the aerodynamic drag of a “bluff body” is described in [34]. Figure 1.10 shows the results of a numerical simulation of flow past a bluff body, which has SJ nozzles at the trailing edge; see Vít, Dančová, and Trávníček, [A8]. These nozzles alternately push and pull the flow of fluid. The figure shows a flow field past a rectangular bluff body in three cases: (a) nozzles do not work, (b) nozzles work in phase, i.e. nozzles push the fluid at the same time and then pull the fluid at the same time, (c) nozzles work in antiphase, i.e. if one of nozzles pushes the fluid, the second pulls the fluid and conversely. Results show a possibility to decrease drag coefficient by about 25 percent with the application of this equipment. It is necessary to regulate both the frequency and

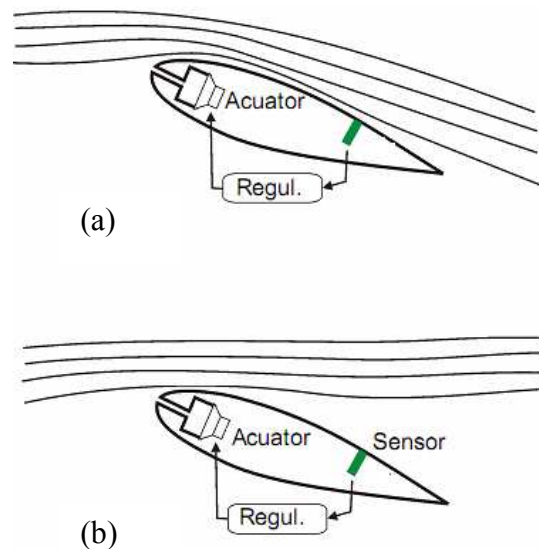


Fig.1.9 Using a SJ to increase lift force on a wing profile, (a) activated SJ, (b) closed SJ, Nishizava *et al* [27]

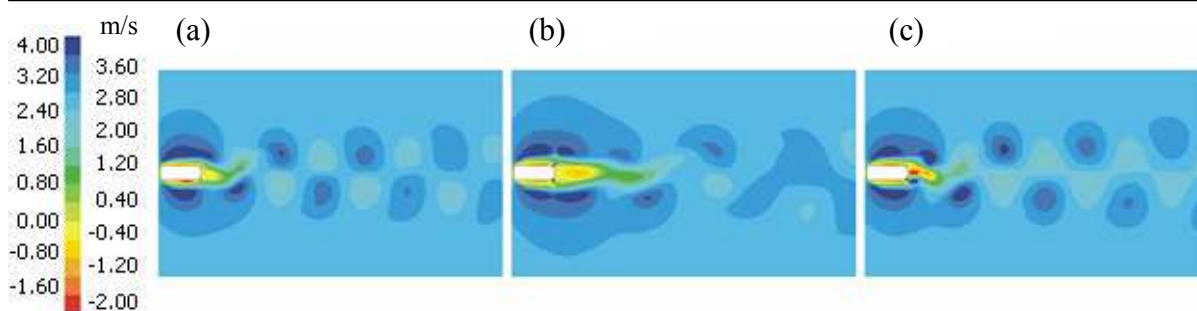


Fig.1.10 Wake past a bluff body in form of contours of x velocity – numerical simulation by Dančová *et al.* [A8], inspired by [26] and [34],

(a) without SJ, (b) SJ nozzles work in phase, (c) SJ nozzles work in phase opposition

power of the SJ in relation to fluid velocity in order to achieve optimal drag reduction. A rectangular profile represents a car model in this case.

I.3 Flow field control in internal aerodynamics

Turbulence control and control of boundary layer separation is another typical example of SJ application. Fluid flow through a wide-open diffuser, which is susceptible to separation from the wall, can be stabilized by using a SJ [35]. Suppression of undesirable flow separation effectively increases efficiency while decreasing power loss.

I.4 Increase of mixing intensity

The increase of mixing intensity is important to many chemical processes, such as in combustion [35]. A typical configuration is numerically solved in paper [36]. Air and fuel flows move into a combustion chamber where a SJ improves their mixing. It is possible to improve the parameters of the combustion equipment, e.g. to increase power, to decrease NO_x emissions, or to decrease overall dimensions.

A concept of a micromixer with a SJ placed at the bottom of a rectangular channel is discussed in paper [76]. Mixing was improved noticeably by the actuation of the SJ, and mixing efficiency was also improved by using an asymmetrical arrangement of a SJ outlet in the channel, [76]. The numerical simulation of flow mixing in a channel using a SJ for biosensor systems is described in [77].

The combination of a SJ and ejectors is described in [A17 and A21]. The aim of the SJ is to excite the mixing layer in the ejector and intensify the mixing process. For ejectors regimes with high ejection ratios, the SJ stabilizes the flow fluctuations in the diffuser, thus achieving higher back pressure and higher efficiency. A SJ placed in the beginning of the mixing chamber positively influences the flow in the diffuser. If the SJ is placed at the end of the mixing chamber, the improvements are reduced. The primary stream is deflected in the direction of the SJ outflow. Velocities of the primary nozzle in the centre of the mixing chamber are affected during the suction and the outflow period of the SJ, with the added effect of increasing velocity fluctuations in this area. The secondary stream and the mixing shear layer are affected by the SJ only in the immediate vicinity of the SJ and of course behind it.

I.5 Increasing heat transfer due to main flow control

A very interesting example of SJ application is the cooling of electronics of very small dimensions [37] (Micro-Electro-Mechanical Systems, MEMS). At these tiny dimensions,

there are often laminar flow regimes, and heat transfer is unacceptably small. Numerical study [37] simulates the intensification of an electronic processor's cooling: the laminar airflow is heated from one-side and affected by the SJ from the other side. Laminar flow is disturbed by the SJ (Timchenko *et al.* [87] suggest the term "quasi-turbulent flow"). The study [34] shows how it is possible to improve processor cooling, including the evaluation of effective geometry and parameters.

Fang *et al.* in [74] experimentally investigated the thermal effects of a synthetic jet actuator on the heat transfer performance of a single-phase water flow confined in a microchannel heat sink. The thermal effects of the SJ are a function of the Reynolds number. Fang's experiments demonstrate that the jet shows a larger improvement of heat transfer performance for the lower microchannel flow rates. He found that a hybrid cooling scheme can enhance the heat transfer performance at a very small penalty of pressure drop increase along the microchannel.

Chaudhari *et al.* [78] investigated heat transfer in a rectangular duct with and without cross-flow and an impinging SJ. Their experiments were performed for the jet Reynolds number in the range of 950-4000 at different offset positions of the SJ.

Trávníček *et al.* [A18] experimentally investigated heat and mass transfer caused by a SJ array, which affected a laminar channel flow. Experiments were focused on low Reynolds numbers and were made in air using the naphthalene sublimation method. An enhancement of local mass transfer was quantified on the opposite channel wall. Based on the heat/mass transfer analogy, mass data were converted to the corresponding heat transfer data.

II. The use of a stand-alone synthetic jet or system of synthetic jets

II.1 Action of force for control of motion, e.g. for autonomous vehicles in water or air

Recently, new generations of SJ generators have been developed, in particular a hybrid SJ and double-acting SJ [38-42] (IT CAS, TU Liberec, Univ. Sheffield, and National Taiwan Univ.). The purpose of these developments has been to improve SJ performance, especially in the field of electronics cooling. In addition, the improved geometry of a SJ generator can be used for nozzle design for an autonomous underwater vehicle (AUV) – [30].

The function of a SJ in water is specific. Although a SJ in water works at a relative low frequency (some tens of Hz on a macroscopic scale of centimeters), gases dissolved in the fluid are released and cavitation increases due to considerable acceleration of the fluid on the actuator surface. A pressure decrease in the actuator leads to the formation of cavitations bubbles – cf. James *et al.* [84]. These bubbles adversely affect the stiffness of the actuator diaphragm and operation of the actuator. The problems connected with the SJ in water are currently under study at the TU of Liberec, Dančová *et al.* [A1-A27].

II.2 Synthetic jet used for intensification of heat transfer. Impinging synthetic jet

This group of applications contains instances of impinging SJs [8, 43, 44, 45, 46, and 47] and instances of complex fluid fields generated solely by SJ [48]. An impinging jet (IJ) is a jet flow that impacts on a solid wall. An IJ achieves a very high forced convection heat/mass transfer rate onto the impingement wall [2, 3] (only two- of three- phase flows can achieve higher magnitudes of this rate). Figure 1.11 shows principle of an IJ. The jet

can be divided into three regions: free-jet region, stagnation region, and wall-jet region. There is a stagnation point on the impingement plate in the stagnation region; at this point, an enhancement of heat/mass transfer is expected.

The pulsation of the jet together with a high level of turbulence intensity leads to a significant increase of the heat transfer coefficient when the equipment is designed properly and the heated or cooled surface is placed in the correct position. Due to this advantage, there is a wide range of possible applications in the field of cooling heavy, thermally loaded parts in electronics or for cooling blades in combustion turbines. More details about these applications can be found in e.g. [38-42, 45, 46, and 47].

The effect of nanoparticle concentration on enhanced heat transfer performance and flow features of a submerged impinging jet system was experimentally investigated by Li *et al* in [72]. Li's experiments revealed that the suspended nanoparticles remarkably increase the heat transfer performance of the base fluid in the impinging jet system and that nanofluid has a larger heat transfer coefficient than pure water under the same Reynolds number. The heat transfer feature of a nanofluid increases with the volume fraction of nanoparticles, [72].

Rylatt and O'Donovan in [73] investigated the effects of confinement on the heat transfer of a synthetic air jet. They tested a passive ducting system designed to reduce the effect of confinement over a range of operating conditions. Their work showed that ducted synthetic air jets provided higher rates of heat transfer in confined conditions. This was attributed to the ducting reducing the recirculation of heated air.

II.3 Pulsatile jets used as valves pumps

The combination of a SJ with a pump or ejector offers further options. Figure 1.12 shows an example of a valve-less pump design [49]. This valve-less pump consists of two diffusers and of chamber with actuator. Diffusers are optimized to have more drag in one direction than in the opposite direction. Periodic motion of the actuator produces a sucking of fluid by the first diffusers and extrusion by the second diffusers. This

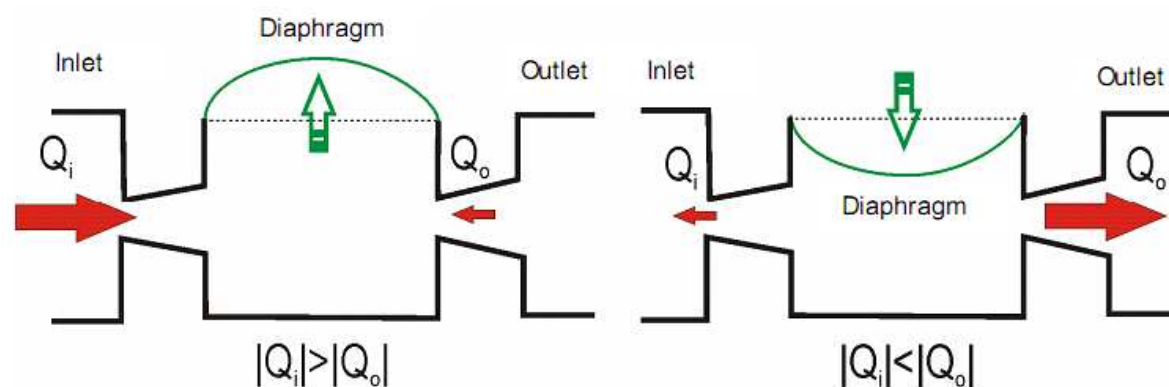


Fig.1.12 Principle of valveless pump, Olsson *et al* [49]

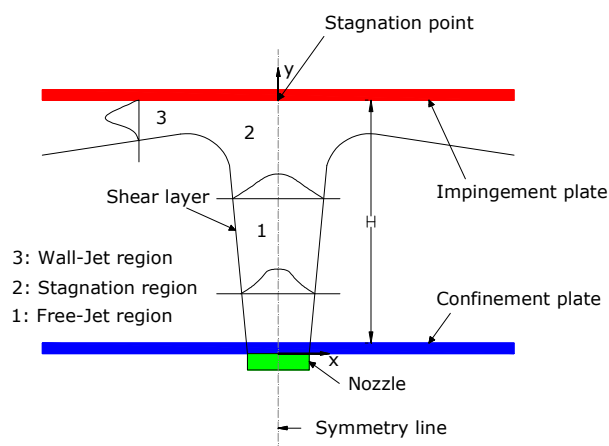


Fig.1.11 Principle of an impinging jet

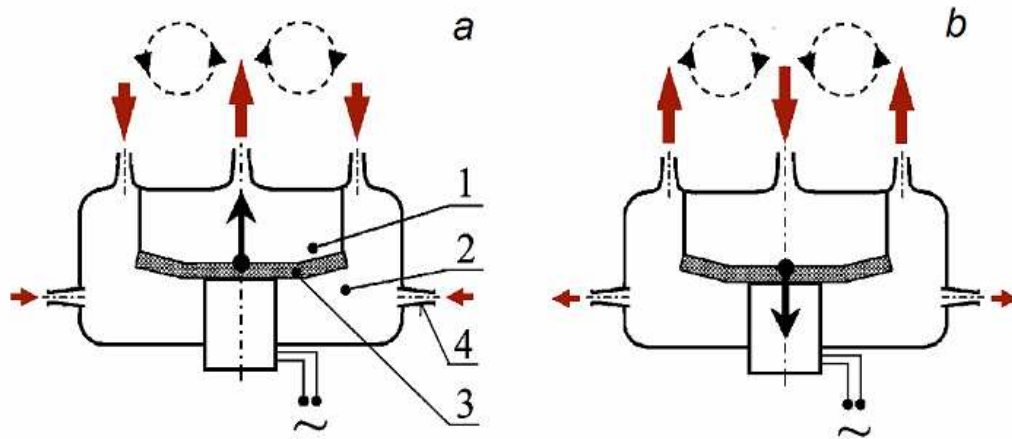


Fig.1.13 Double-acting hybrid SJ actuator, Trávníček *et al* [38, 39]

equipment can have a very high power in small dimensions. One improvement in particular is seen in MEMS systems.

The idea to combine a SJ and a valve-less pump led to the design of a hybrid synthetic jet actuator [50]. Figure 1.13 shows the design of a double-acting hybrid synthetic jet actuator. Figure 1.13a shows the extrusion stroke from the front chamber (1), when the fluid is sucked simultaneously into the back chamber (2). The opposite action (sucking fluid into the front chamber) is shown in Figure 1.13b. The resulting flow in the actuator orifice is non-zero-net-mass flux in character – enabling better results to be achieved in the noted applications [38, 39].

1.1.3 SYNTHETIC JET IN CROSS FLOW

The principle of this work is a SJ in a cross flow. Current literature more often describes the principle of a SJ without interaction of the other influences. Despite this, some authors have investigated this problem experimentally, but more frequently numerically.

Gordon *et al.* in [90] investigated two circular ZNMF¹ jets with parameters $Re_j = 1,240$, velocity ratio $c_U = U_j / U_\infty = 4.6$, $St = 0.016$ and $Re_j = 2,960$, $c_U = 7$, $St = 0.014$, in a cross flow via PIV and compared these with continuous and pulsed jets. In [91] Gordon *et al* investigated the mean passive scalar field in a round ZNMF in a cross flow. They used same actuator as in [90]. The critical Strouhal number was $St = 0.02$ in their work.

The effects of periodic disturbances of a round pulsed jet in a cross flow in water as a working fluid was investigated by Eroglu and Breidenthal in [92]. Flow visualization experiments revealed that the structure of a traverse jet is dominated by the formation of a curved shear layer, composed of distinct vortex loops around the jet in the near-field, as well as the subsequent interactions among neighboring loops as the jet bends over.

Vortex generating jets (VGJs) passing through a wall into a cross-flow was investigated experimentally Khan and Johnston in [93]. They changed VGJs configuration, including pitch, skew angles (Φ and Θ), and velocity ratio (c_U). For $c_U = 1$, the VGJs configuration of $\Phi = 30^\circ$ and $\Theta = 60^\circ$ has been identified to produce a vortex with the highest peak mean vorticity.

¹ ZNMF – zero-net-mass-flux is one of the main advantages of a SJ. It means that the time-mean mass flux of the oscillatory flow in the SJ actuator orifice is zero (described in Chapter 1.1.2).

In [94], Lai and Lee numerically investigated a multiple tandem jet in a cross flow and formulated a general, semi-analytical model.

1.2. MOTIVATION OF THE WORK

The thesis is focused on SJs, namely on SJs interacting with a laminar channel cross flow. One of the first studies focusing on a channel flow under acoustic control (for heat transfer enhancement) was presented in 1982 by Gutmark *et al.*, [51]. Another promising alternative is linked to the possibilities of synthetic jets – Timchenko *et al.*, [52].

The present study places emphasis on the problem of low Reynolds numbers. This arrangement can be useful in many applications, namely on a micro-scale, such as the cooling of micro-electronics and the detection of various (biological, biomedical, or chemical) matters. The flow regime on a micro-scale is usually laminar with very small Reynolds numbers. Therefore, the transfer processes such as mixing and cooling are typically based on gradient diffusion. It is worth mentioning that the current Reynolds numbers (in order of 10^2) are too low for an initiation of transition to turbulence. On the other hand, actuation of the laminar channel (Poiseuille) flow can essentially enhance the transport mixing creating the so-called “quasi-turbulent” flow character – Timchenko *et al.* [52]. Moreover, it should be noted that the current subject (a laminar channel flow controlled by SJs) is different from a “SJ in a boundary layer” or a “SJ in a cross flow”.

At the time of preparing and writing this PhD thesis (starting in 2006), studies of the effect of a SJ on channel flows were conducted solely by means of numeric simulations, e.g. [52]. Dančová *et al.* in works [A13 and A14] conducted the first experiments. The geometry of micro-electronic applications has been scaled to sufficiently large dimensions (in order of centimeters) to allow for experiments.

The thesis is an experimental investigation with water as the working fluid. Various experimental methods are used, namely tin ion visualization, laser Doppler vibrometry (LDV), hot-wire anemometry (HWA), and particle image velocimetry (PIV).

1.3. AIMS OF THE WORK

- Design and development of an experimental setup:
 - SJ actuator,
 - experimental channel with single SJ actuator,
 - experimental setup with SJ array.
- Clarification of the resonance behavior of the developed actuator:
 - theoretical analysis based on energy conservation,
 - experimental evaluation of frequency characteristics by means of hot wire anemometry (HWA).
- Preparation of the auxiliary experiments, and their carrying out:
 - visualization of single SJ and SJ array using tin ion method,
 - investigation of piezoceramic transducers using laser Doppler vibrometry,
 - evaluation of a SJ flow field using HWA.
- Main part of experiments will be performed by means of PIV, focusing on:
 - laminar channel flow itself,

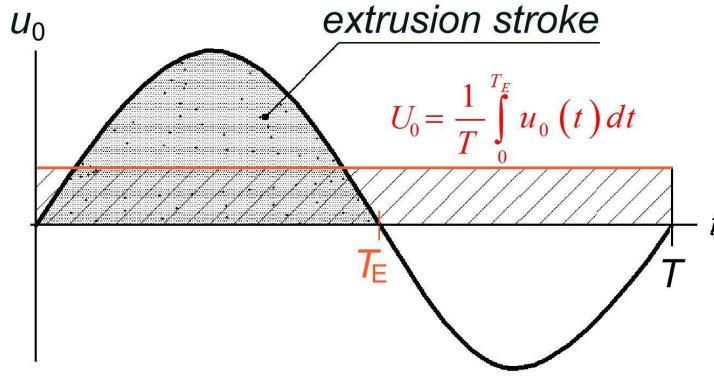


Fig.1.14 Schematic view of the formulation of the time-mean velocity U_0

- single SJ in quiescent fluid,
- single SJ in a laminar channel flow,
- SJ array in quiescent fluid,
- SJ array in a laminar channel flow.

- Analysis of results.

1.4. PROBLEM PARAMETERIZATION

A SJ is characterized by several independent parameters.

When considering the **plug flow model** (one-dimensional piston – like flow in the actuator orifice), the main parameters of a SJ are:

- The actuator orifice diameter D .
- The time-mean orifice velocity U_0 , U_{0A} , respectively (see Figure 1.14)

$$U_0 = \frac{1}{T} \int_0^{T_E} u_0(t) dt \quad (1.13a, b),$$

$$U_{0A} = \frac{1}{T} \int_0^{T_E} \left[\frac{1}{A} \int_0^A u_0(t, r) dA \right] dt$$

where T means the time period, i.e. $T = 1/f$ and f means the frequency, T_E means extrusion time ($T_E = T/2$ for the sinusoidal waveform or $T_E \neq T/2$ for the non-sinusoidal waveform), $u_0(t)$ means the periodical axial orifice velocity. For the sinusoidal waveform $u_0(t) = U_{\max} \sin(2\pi ft)$, one can easily derive $U_{\max} = \pi U_0$. A as the cross-section area of the exit orifice of the actuator and r as the orifice radius.

- The “stroke length” L_0 , L_{0A} , respectively

$$L_0 = U_0 \cdot T = \frac{U_0}{f} \quad (1.14a)$$

$$L_{0A} = U_{0A} \cdot T = \frac{U_{0A}}{f} \quad (1.14b),$$

- The Reynolds numbers of a SJ

$$\begin{aligned} \text{Re}_{\text{SJ}} &= \frac{U_0 \cdot D}{\nu} \\ \text{Re}_{\text{SJ}_A} &= \frac{U_{0A} \cdot D}{\nu} \end{aligned} \quad (1.15a, b),$$

where ν is the kinematic viscosity [m^2/s] and D is the orifice diameter.

- The Strouhal number is not an independent parameter; it depends on the above parameters (Eq. (1.14)). It has been defined by V. Tesař, S. Zhong, [53] as $St = fD/U_{\text{max}}$. For a sinusoidal waveform:

$$\begin{aligned} St &= \frac{1}{\pi} \frac{f \cdot D}{U_0} = \frac{1}{\pi} \frac{D}{L_0} \\ St_A &= \frac{1}{\pi} \frac{f \cdot D}{U_{0A}} = \frac{1}{\pi} \frac{D}{L_{0A}} \end{aligned} \quad (1.16a, b).$$

- Time-averaged SJ mass flux, averaged over the entire period (cf. Eq.(1.13a))

$$\dot{Q}_{\text{SJ}} = \rho U_0 \pi D^2 / 4 \quad (1.17),$$

where ρ is fluid density.

- Time-averaged SJ momentum flux (again, averaged over the entire period)

$$M_{\text{SJ}} = \frac{1}{T} 2\rho \int_0^R \int_0^{T_E} u_0^2(r, t) \pi r dr dt \quad (1.18a).$$

Assuming the plug flow model (i.e. the uniform profile of the instantaneous velocity, $u_0(r, t) = u_0(t)$) and the sinusoidal waveform in time $u_0(t) = U_{\text{max}} \sin(2\pi ft)$, where U_{max} is the velocity amplitude, the Equation (1.18a) can be expressed as:

$$M_{\text{SJ}} = \frac{1}{T} 2\rho \int_0^R \int_0^{T_E} U_{\text{max}}^2 \sin^2(2\pi ft) \pi r dr dt = \frac{\rho R^2 U_{\text{max}}^2}{2fT} \frac{2\pi f T_E}{2} = \frac{\rho \pi R^2 U_{\text{max}}^2}{4} \quad (1.18b).$$

- Derivation of the resonance frequency of a SJ actuator

A SJ actuator works with the highest efficiency at the resonance frequency. During the working cycle of a SJ actuator, the potential energy E_p of the actuator membrane is transformed into kinetic energy of the fluid E_k in the orifice. The kinetic energy of the fluid in the actuator cavity can be neglected compared to kinetic energy in the orifice. The total energy of the fluid can be defined as the sum [38]:

$$E = E_p + E_k \quad (1.19).$$

The oscillation of the membrane is assumed to be harmonic, and membrane displacement is defined as:

$$y = y_{\max} \sin(\omega t) \quad (1.20),$$

where y_{\max} is the amplitude of the membrane and $\omega = 2\pi f$. The velocity of the membrane motion is the derivative of its displacement:

$$\frac{dy}{dt} = \omega \cdot y_{\max} \cos(\omega t) \quad (1.21).$$

From the continuity equation for incompressible flow, the mean velocity of the flow in an orifice of the cross section area $A = \pi D^2 / 4$ can be calculated as:

$$u_0(t) = C \cdot \frac{A_m}{A} \omega \cdot y_{\max} \cos(\omega t) \quad (1.22),$$

where $A_m = \pi D_m^2 / 4$ is the area of the membrane with diameter D_m , and C is the constant, which corrects to the deformed membrane shape (for piston $C = 1$ and for a membrane with pyramid shape and approximately for a piezoelectric transducer $C = 1/3$).

The kinetic energy of the flow is defined as:

$$E_k = \frac{\rho L_e A u_0^2}{2} \quad (1.23)$$

where ρ is fluid density and L_e is the so-called ‘‘equivalent length’’ and can be calculated as:

$$L_e = L + \frac{8D}{3\pi} \quad (1.24)$$

where L is the orifice length and D is the orifice diameter.

When combining equations (1.22) and (1.23), the kinetic energy is written as:

$$E_k = \frac{\rho L_e A \left[C \frac{A_m}{A} \omega \cdot y_{\max} \cos(\omega t) \right]^2}{2} \quad (1.25).$$

The potential energy of the membrane can be written as:

$$E_p = \frac{1}{2} k_p A_m y^2 = \frac{1}{2} k_p A_m y_{\max}^2 \sin^2(\omega t) \quad (1.26),$$

where k_p is the stiffness of the membrane.

At maximum membrane deflection, the kinetic energy of the flow is zero, and potential energy is maximal. In a neutral (zero) membrane deflection, kinetic energy is maximal, and potential energy is zero. Therefore, it can be written as:

$$E = E_{k_{\max}} = E_{p_{\max}} \quad (1.27).$$

The maximum values of the kinetic and potential energies with respect to Equation (1.25) and (1.26) are:

$$E_{k_{\max}} = \frac{\rho L_e A \left[C \frac{A_m}{A} \omega \cdot y_{\max} \right]^2}{2} \quad (1.28),$$

$$E_{p_{\max}} = \frac{1}{2} k_p A_m y_{\max}^2 \quad (1.29).$$

From Equation (1.27), the value of the resonance frequency can be derived as:

$$f = \frac{1}{2\pi \cdot C} \frac{D}{D_m} \sqrt{\frac{k_p}{\rho L_e}} \quad (1.30).$$

The second resonance follows the Helmholtz resonator frequency, [71]. When considering isentropic expansion and compression during pressure oscillations in a cavity, the resonance frequency can be written as:

$$f_{\text{HELM}} = \frac{c}{2\pi} \sqrt{\frac{A}{L_e V}} \quad (1.31),$$

where c is the isentropic speed of sound (in water $c = 1435 \text{ m/s}$), $A = \pi D^2 / 4$ is the cross-sectional area of the actuator orifice and V is the actuator cavity volume.

Because the investigation is focused on a channel flow affected by either one SJ or an array of SJs, it is also necessary to define:

- The Reynolds number of the 2D channel flow, (2D simplification of the flow between **two parallel plates**)

$$\text{Re}_C = \frac{U_C \cdot D_{CH}}{\nu} = \frac{U_C \cdot 2H}{\nu} \quad (1.32),$$

where $U_C = (2/3) \cdot U_{C_max}$ (Eq. 1.7) is the time-mean velocity through the channel, U_{C_max} is the maximum velocity in the channel, and H is the channel height.

- The Reynolds number of the 3D channel flow

$$\text{Re}_{C_3D} = \frac{U_{C_3D} \cdot D_{CH}}{\nu} = \frac{U_{C_3D} \cdot 2HB/(H+B)}{\nu} \quad (1.33),$$

where D_{CH} is the hydraulic diameter of the channel cross-section, and B is the channel width.

- The strength of the control SJs can be quantified relative to the main channel flow in terms of the ratios of velocities, flow rates, and momentum:

$$c_U = \frac{1}{n} \sum_{i=1}^n \left(\frac{U_{0i}}{U_C} \right) \quad (1.34),$$

$$c_Q = \frac{A}{A_C} \sum_{n=1}^n \left(\frac{U_{0i}}{U_C} \right) \quad (1.35),$$

$$c_M = \frac{nM_{SJ}}{\rho B \int_{-H/2}^{H/2} U^2(y^*) dy^*} = n \frac{5\pi^2}{24} \left(\frac{A}{BH} \right) \left(\frac{U_0}{U_C} \right)^2 \quad (1.36a),$$

$$c_M = \frac{5\pi^2}{24} \left(\frac{A}{A_C} \right) \sum_{i=1}^n \left(\frac{U_{0i}}{U_C} \right)^2 \quad (1.36b),$$

where A is the cross-section area of the SJ actuator orifice ($A = \pi D^2 / 4$), n is the number of control SJs ($n = 1$ or 4 for the current study), and $A_C = BH$ is the cross section of the channel (width x height). In Equation (1.36), the laminar parabolic profile of two-dimensional flow is assumed – see Eq. (1.5b).

Eq. (1.36a) can be used if the individual SJ actuators have the same value of U_0 . Eq. (1.36b) has general validity, which is useful in the case of SJs with slightly different velocities (as will be evaluated in the current study).

CHAPTER 2

EXPERIMENTAL SETUP AND METHODS

2.1 EXPERIMENTAL SETUP

2.1.1 SYNTHETIC JET ACTUATOR

The first step of the SJ research was the development of a SJ actuator. The actuator (see Figure 2.1) consists of a sealed cavity, which was equipped with an emitting orifice (diameter $D = 3.0\text{mm}$) and with an actuating piezoelectric membrane (KINGSTATE KPS-100 – see Figure 2.2, diameter of the cavity $D_D = 36\text{mm}$). Appendix 1 shows the SJ actuator drawing with the exact dimensions.

The piezoelectric membrane (piezoceramic transducer – PCT – see Figure 2.2) was used because it offered several significant advantages, e.g. applicability in different fluids, in broad temperature ranges, and in heavy-duty facilities. Further advantages of a PCT include a long operational lifetime and low power consumption.

A PCT is composed of two basic layers – a piezoceramic layer and a metallic membrane. The piezoceramic material is based on the oxides of lead (Pb), zirconium (Zr), and titanium (Ti) solid solutions and is piezoelectrically active. The metallic membrane is piezoelectrically neutral. These two layers are fixed firmly together. A thin layer of silver is coated on one side of the piezoceramic to form an electrode. The second electrode is comprised of a piezoelectrically neutral metal plate.

All actuator sizes stem from the previous experiences of the author with SJ actuators, e.g. [A13 and A14].

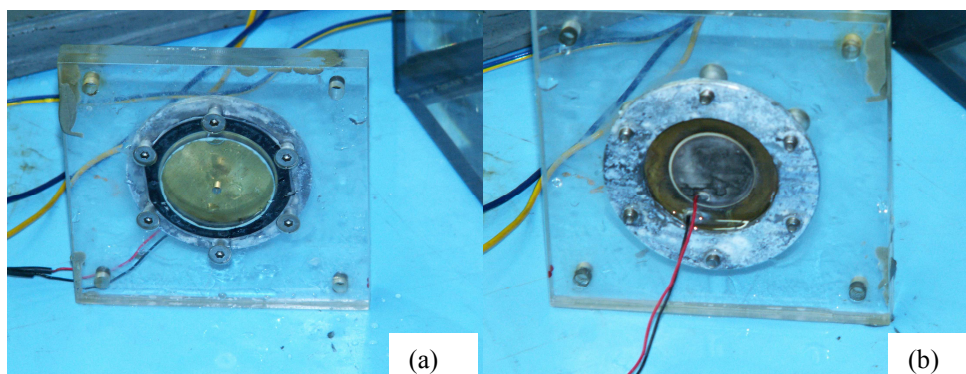


Fig.2.1 SJ actuator (a) front view, (b) view of the PCT

2.1.2 TESTED CHANNEL FOR SINGLE SYNTHETIC JET ACTUATOR

Figures 2.3 and 2.4 show the tested channel for a single SJ actuator. This tested channel was made for the PIV experiments at TU Eindhoven (Netherlands). The walls of the tested channel were made out of Plexiglas. Blackening of the bottom plate reduces laser reflections for PIV experiments. The channel inlet was carefully rounded to prevent flow separation, and its end was equipped with a grid (position 7 in Figure 2.4) to prevent flow separation at the inlet and to control flow velocity through the channel. The channel length, height, and width are $L_{UP} + L_{DOWN} = 1020\text{mm}$, $H = 40\text{mm}$, and $B = 200\text{mm}$, respectively. When conducting experiments, the channel was assembled with aluminum supports (Figure 2.3, not drawn in Figure 2.4) and was inserted into the water circulation channel (TU Eindhoven) with a cross section of $570\text{mm} \times 450\text{mm}$ (horizontal x vertical dimensions, respectively).



Fig.2.2 Piezoceramic transducer

Figure 2.4 shows a schematic view of the configuration – the tested channel inside the circulation water channel. In this setup, the synthetic jet actuator is located at position 4 (Figure 2.4). As mentioned in paragraph 2.1.1, the actuator consists of a sealed cavity, which was equipped with an emitting orifice and with an actuating piezoelectric membrane. The actuator orifice was oriented vertically upwards to the exposed channel.

2.1.3 SYNTHETIC JET ARRAY SETUP

In the next step of investigation, a SJ array of four SJ actuators was placed across the channel cross section. Figures 2.5a and b show the horizontal projection of a single SJ and SJ array, respectively. The coordinate system used is visible.

For the investigation, two experimental setups were made. The first setup (see Figure 2.6a) was made for LDV experiments to find four PCTs with the same characteristics and phase shift and to carry out flow visualization and PIV experiments of an SJ array without affecting the channel flow. This setup was made from Plexiglas; for exact dimensions see Appendix 3. The upper wall is bolted on with four screws, allowing the wall to be removed.

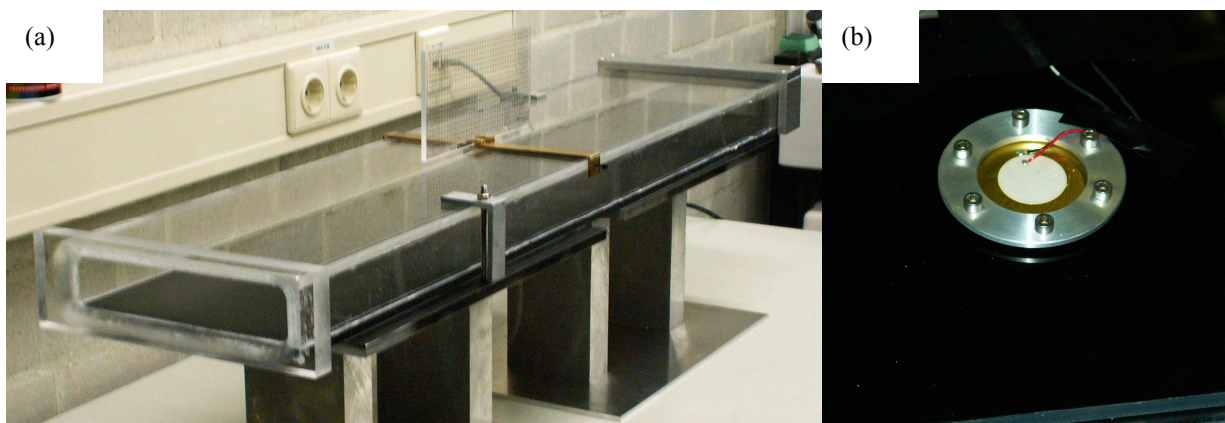


Fig.2.3 Tested channel (a) general view, (b) detailed view of the SJ actuator on the bottom

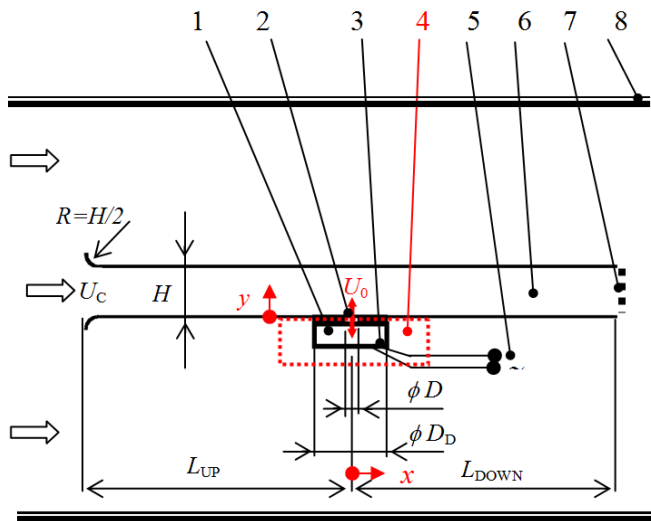


Fig.2.4 Schematic view of the present configuration. 1 – SJ cavity, 2 – SJ orifice, 3 – SJ membrane, 4 – SJ actuator, 5 – AC supply, 6 – tested channel, 7 – grid, 8 – water circulation channel

For the experiments with a SJ array in a channel, a Plexiglas wall (Fig.2.6b, for dimensions see Appendix 4) with dimensions: *length (length with start) x width x thickness* = (860 (880) x 200 x 10) mm was constructed. The wall inlet was carefully rounded, and the SJ array was placed 520mm from the beginning. The wall was put into a circulation water channel at the Institute of Thermodynamics (described in Chapter 2.1.4).

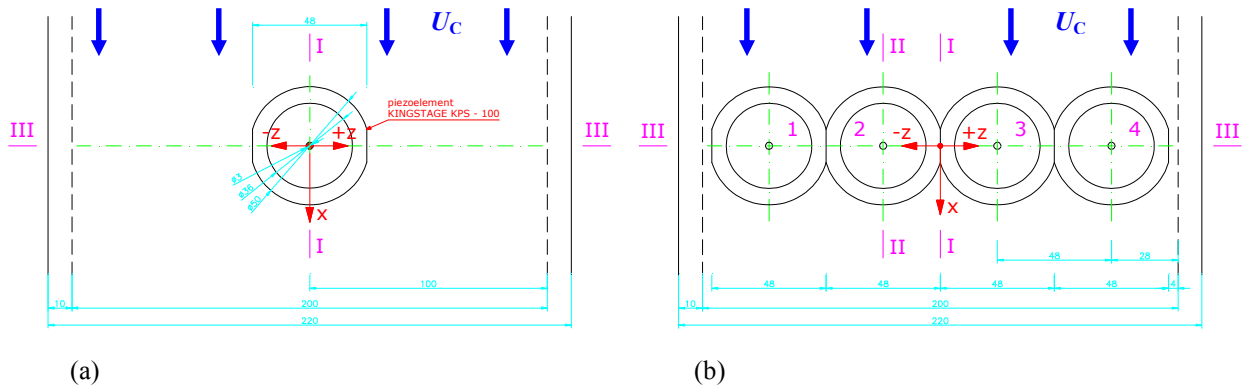


Fig.2.5 Horizontal projection (a) single SJ, (b) SJ array

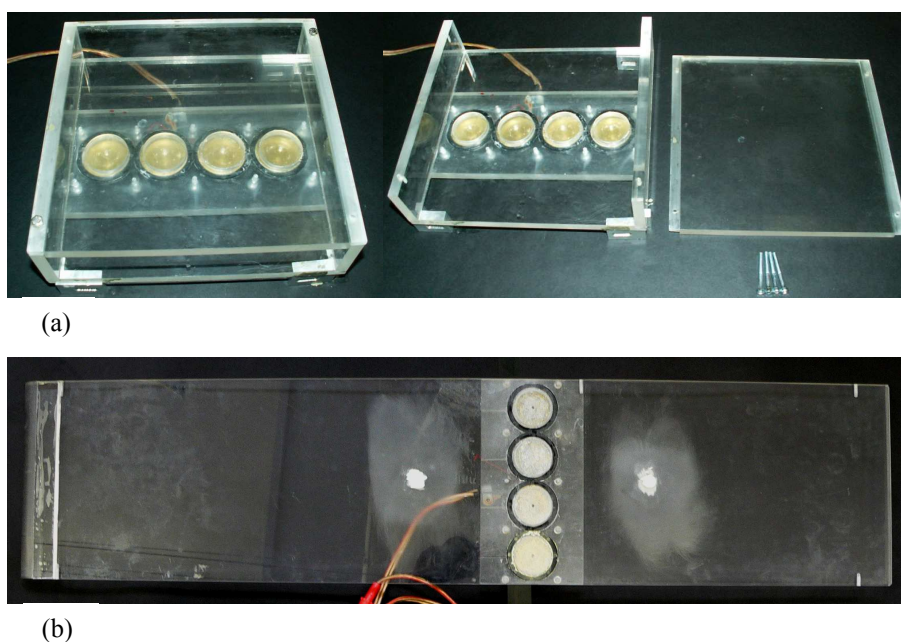


Fig.2.6 SJ array equipment (a) with and without the upper wall, (b) plexiglas wall

2.1.4 CIRCULATION WATER CHANNELS

Two circulation water channels were used for the experiments: at the Eindhoven University of Technology (TU/e) in the Netherlands, and at the Institute of Thermomechanics AS CR, v.v.i, (IT) in the Czech Republic (the PIV system used at IT was from Technical University of Liberec – TUL). Nevertheless, the channel with single SJ/SJ array device width and height were the same at both facilities (see Figs. 2.4 and 2.8): $B = 200\text{mm}$, and $H = 40\text{mm}$, respectively. The device length, $L_{UP} + L_{DOWN}$ was slightly larger at the TU/e facility (1020mm), while it was 880mm at the IT facility – see Figs. 2.4 and 2.8, respectively.

Note that the channel length upstream from the SJ location, L_{UP} , was designed to be longer than the hydrodynamic entrance length L_{hy} , which is discussed in part 1.1.1, Eq. (1.1) above.

The circulation water channel at TU/e (schematic view in Figure 2.7, see Appendix 5 for photos) has a cross section of 570mm x 450mm (horizontal x vertical dimensions, respectively); the length is approximately 2500mm. There are water tanks (approx. dimensions: diameter 1000mm, height 2200mm) at both sides of the channel. Three pumps on three sectional pipes control the water flow rate.

Figure 2.8 shows the circulation water channel used at IT. This vertical channel was made from Plexiglas. A pump pumps water to the top. Inside the channel, a Plexiglas plate with a SJ array is placed vertically.

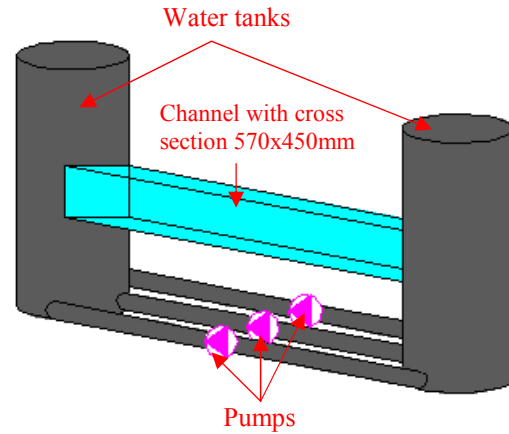


Fig.2.7 Schematic view of the water channel at TU/e

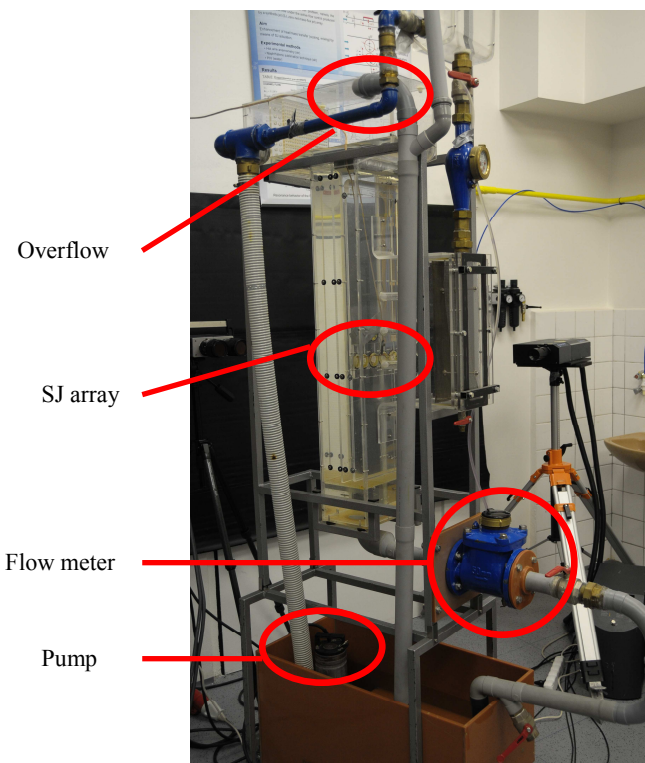


Fig.2.8a Circulation channel at IT CAS

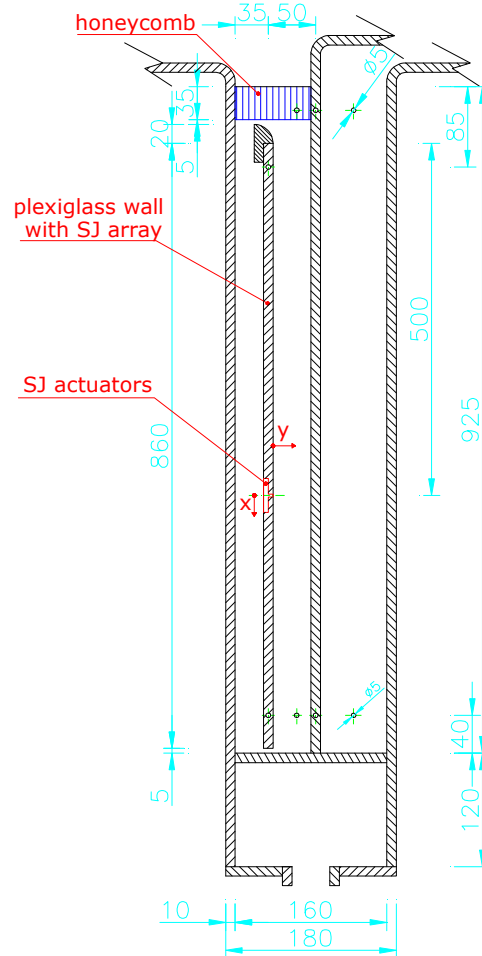


Fig.2.8b Drawing of circulation channel at IT CAS

2.2 SIGNAL (e.g. VELOCITY) DECOMPOSITION

2.2.1 CONTINUOUS SAMPLING

In continuous sampling, the data are recorded constantly. Moreover, the driving signal also has to be recorded (e.g. a TTL signal). This driving signal is used for measuring signal decomposition – the principle is shown in Figure 2.9, wherein the acquired signal is divided into N individual periods (Figure 2.9b) that are used to calculate the periodic part (Figure 2.9c). Triple decomposition was used for velocity analysis, as described in paragraph 2.2.3 below.

Continuous sampling was used for the HWA experiments in this work. For our experiments, the typical sampling frequency and number of samples were 7 kHz and 32 768, respectively.

2.2.2 CONDITIONAL SAMPLING

Conditional sampling is a sampling that depends on all conditions – i.e. sampling always has to occur at the same phase in a process. For example, the sampling starts with the beginning of the period given by an external periodical signal (TTL or pulse). In accordance with the external signal, the synchronization is performed. For more details, see Bruun [55].

Conditional sampling is used for PIV experiments. Figure 2.10 shows schematically the sinusoidal driving signal from the generator, which feeds the SJ (blue), the TTL signal (green) from the generator, which has a frequency identical to the driving signal, and the pulse signal from laser (red). The laser starts to work with the leading edge (our choice) of the TTL signal from the generator at the exactly set time (sampling starts at this time). Changing of this time enables the whole SJ period to be measured.

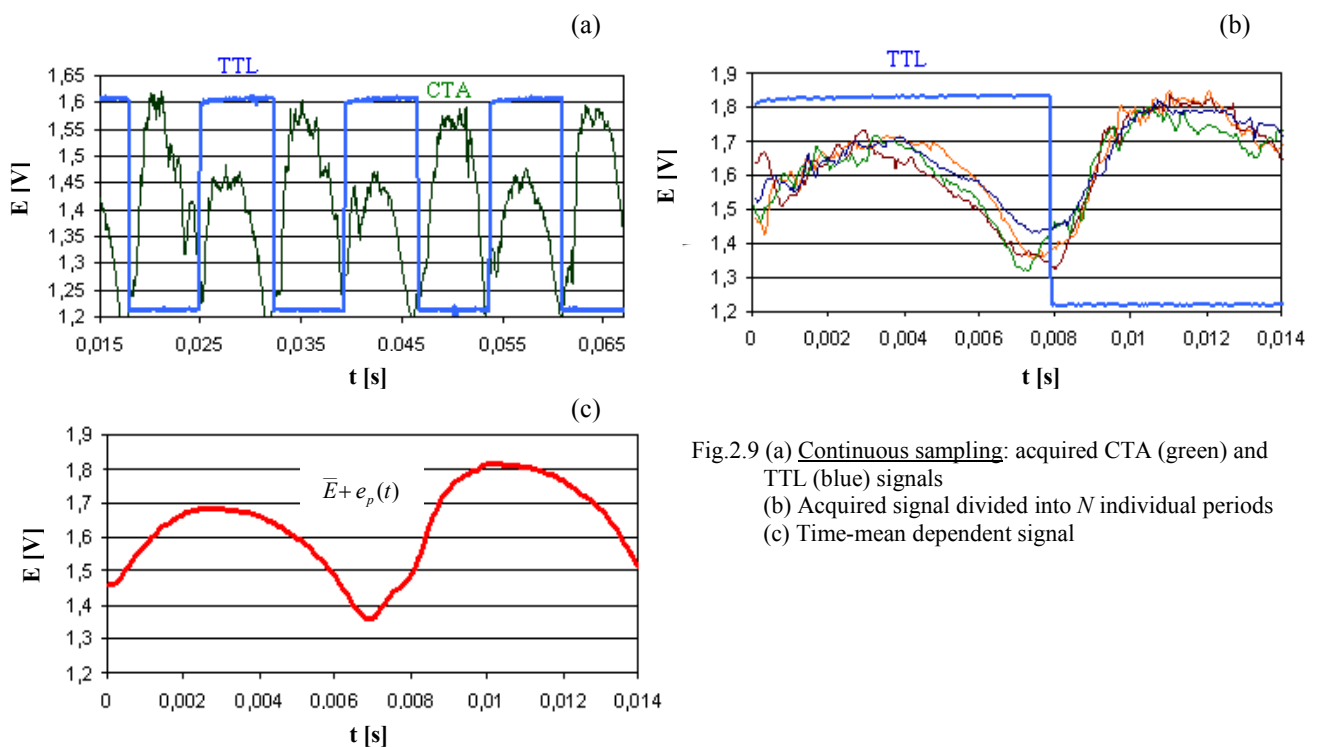


Fig.2.9 (a) Continuous sampling: acquired CTA (green) and TTL (blue) signals
 (b) Acquired signal divided into N individual periods
 (c) Time-mean dependent signal

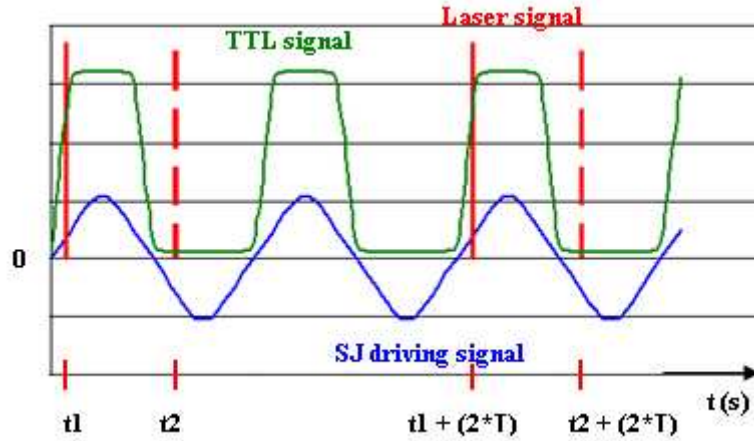


Fig. 2.10 Schematic of conditional sampling (t_1, t_2 is the exactly set time for sampling; T means the period)

2.2.3 PHASE AVERAGING

Phase averaging is used for measured signal decomposition. Signal decomposition is used to analyze the results of hot wire anemometry (constant temperature anemometry – CTA) experiments (principle of CTA is described in Chapter 2.3.1). During the measurement, two signals are recorded – the CTA signal and the TTL signal. The frequency of the TTL signal corresponds to the frequency of an actuator. The TTL signal jumps between a maximal and minimal value of 4.0V and 0.1V. The TTL signal is used to separate the individual periods recorded during CTA measurement.

The recorded, instantaneous signal $E(t)$ is the composition of the mean time, periodic, and fluctuating parts, i.e. \bar{E} , $e_p(t/T)$, $e'(t/T)$, respectively:

$$E(t) = \bar{E} + e_p(t/T) + e'(t/T) \quad (2.1).$$

The definition of the velocity components in the stream-wise direction is the following:

$$u(t) = U + U_p(t/T) + u'(t/T) \quad (2.2),$$

where $u(t)$ is the instantaneous velocity, U , U_p , and u' are the time-mean, periodic (coherent), and fluctuation (incoherent, random) components, respectively, and t/T indicates the phase during the cycle.

The time-mean component can be determined by:

$$\bar{E} = \lim_{T \rightarrow \infty} \frac{1}{T} \int_0^T E(t) dt \quad (2.3).$$

To quantify of the fluctuating part $e'(t/T)$, the root mean square (rms) value of the signal is evaluated. The turbulent intensity at a particular time is defined as:

$$T_i(t/T) = \frac{[e(t/T)]_{\text{rms}}}{\bar{E} + e_p(t/T)} \quad (2.4),$$

where $e(t/T)_{rms}$ is the standard deviation in the phase t/T calculated as:

$$[e(t/T)]_{rms}^2 = \frac{1}{N} \sum_{n=1}^N \left[E(t+nT) - \left[\bar{E} + e_p(t/T) \right] \right]^2 \quad (2.5),$$

where N is the number of the periods of the acquired signal.

Figures 2.9a, b, and c show schematically the principle of phase averaging. With help from the TTL, the acquired signal is divided into N individual periods (Figure 2.9b). The periodic part is calculated from these periods (Figure 2.9c).

In the case of SJ experiments in this work, the measured SJ period was divided into 12 parts of 5.5ms. Each double image gives the instantaneous figure (resultant image), i.e. information about particle displacement represents each of these 12 parts. In time averaging, the images are put together at the same time (the same part of the measured periods) during SJ actuating cycles. Figure 2.11 demonstrates an example of phase averaging in PIV experiments. It shows a single SJ without channel flow interaction at the instant of maximum extrusion velocity ($t/T = 0.25$), with the resulting vector maps averaged over 100 PIV records (i.e. recorded in the same part of 100 periods).

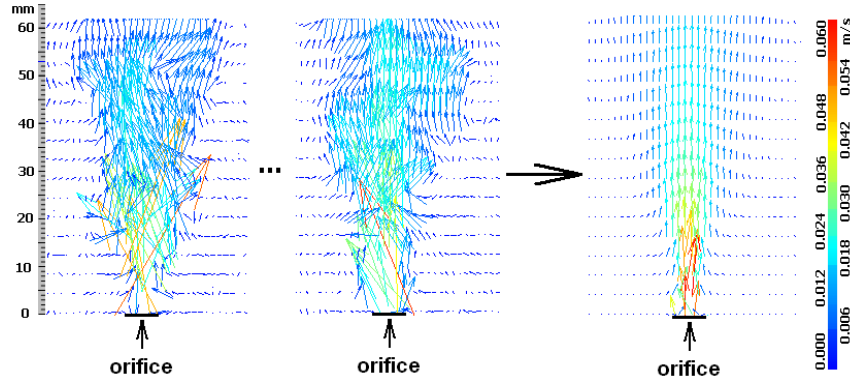


Fig.2.11 SJ phase average of 100 periods in $t/T = 0.25$ (vectors of velocity magnitude)

2.2.4 TIME AVERAGING

Time averaging can be expressed as:

$$u(t) = U + U_p(t) + u'(t) \quad (2.6),$$

$$U = \lim_{T_1 \rightarrow \infty} \frac{1}{T_1} \int_0^{T_1} u(t) dt \quad (2.7),$$

$$[u(t)]_{rms}^2 = \frac{1}{N} \sum_{n=1}^N [u(t) - U]^2 \quad (2.8),$$

where $u(t)$ is the instantaneous velocity, U , U_p , and $u'(t)$ are the time-mean, periodic, and fluctuation components, respectively, $u(t)_{rms}$ is the standard deviation, t indicates time, and N is the number of SJ cycles (e.g. recorded double images during PIV measurement).

2.3 EXPERIMENTAL METHODS

2.3.1 HOT-WIRE ANEMOMETRY

2.3.1.1. PRINCIPLE

Hot wire anemometry (HWA) is one of the classical methods for measuring fluid velocities, including a fluctuating velocity component. It was used in this study to quantify SJ velocities in general and to evaluate the resonant frequency of SJ actuators in particular.

The method is based on convective heat transfer from a heated body (hot wire or hot film probe) into a moving environment. The basic element of the measuring circuit is the probe, which is a wire fixed to the prongs of the carrier. The wire (typically tungsten) is heated by an electric current. The heat flux generated by the electric current in the wire element of length dx can be formulated according to Joule's law in the form:

$$d\dot{Q}_J = \frac{I^2 \chi_{\text{wire}}}{S_{\text{wire}}} dx \quad (2.9),$$

where I is the electric current, χ_{wire} is the specific resistance of wire material at the wire temperature T_{wire} , and S_{wire} is the wire cross section area; for more details, see Bruun [55].

The heat flux $d\dot{Q}_J$ generated in the wire element dx (see Figure 2.12) must be equal to the sum of the heat transferred into the surroundings, i.e. the convective transferred heat $d\dot{Q}_{\text{conv}}$, the heat transferred into carriers $d\dot{Q}_{\text{cond}}$, the heat radiated into the surroundings $d\dot{Q}_{\text{rad}}$, and the accumulated heat $d\dot{Q}_{\text{ac}}$:

$$d\dot{Q}_J = d\dot{Q}_{\text{conv}} + d\dot{Q}_{\text{cond}} + d\dot{Q}_{\text{rad}} + d\dot{Q}_{\text{ac}} \quad (2.10).$$

The heat dissipated by radiation is in most cases negligible, and the heat dissipated from the wire into the carrier can be considered as independent of the parameters of the flowing medium [55]. The convective heat flux $d\dot{Q}_{\text{conv}}$ transferred into the flowing medium can be formulated as:

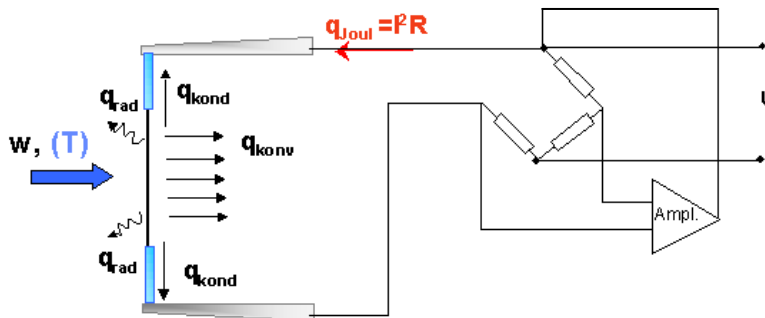


Fig.2.12 Schematic view of HWA (CT) measurement

$$\begin{aligned} d\dot{Q}_{\text{conv}} &= \pi d_{\text{wire}} \alpha (T_{\text{wire}} - T_{\infty}) dx \\ \dot{Q}_{\text{conv}} &= \pi d_{\text{wire}} l_{\text{wire}} \alpha (T_{\text{wire}} - T_{\infty}) \end{aligned} \quad (2.11a, b),$$

where d_{wire} is the wire diameter, α is the (overall) heat transfer coefficient, T_{wire} the wire surface temperature, and T_{∞} is the fluid temperature [55]. Based on this knowledge, HWA can be used for both velocity and temperature measurement.

If a constant temperature mode is assumed, the thermal balance for an infinitely long wire, where the heat transfer into the holder is ignored, is given by:

$$I^2 R_{\text{wire}} = \pi d_{\text{wire}} l_{\text{wire}} \alpha (T_{\text{wire}} - T_{\infty}) \quad (2.12),$$

where R_{wire} is the wire resistance on a heated wire with the temperature T_{wire}

$$R_{\text{wire}} = \int_l \frac{\mathcal{X}_{\text{wire}}}{S_{\text{wire}}} dx \quad (2.13).$$

After a substitution of resistance $R_{\text{wire}} = R_0 [1 + \alpha_0 (T_{\text{wire}} - T_0)]$ and Ohm's law $E_{\text{wire}} = IR_{\text{wire}}$, the equation (2.12) becomes:

$$\frac{E_{\text{wire}}^2}{R_{\text{wire}}} = (A + BU^n) (T_{\text{wire}} - T_{\infty}) \quad (2.14),$$

where A , B and n are the functions of wire diameter and the material properties of the wire, and of the surrounding fluid, whose magnitude are determined through calibration, [55].

As mentioned above, HWA probes are sensitive to both the velocity of the surrounding fluid and its temperature. The velocity sensitivity $S_{u,CT}$ of a probe connected in constant temperature (CTA) regime can be calculated as:

$$S_{u,CT} = \frac{\partial E_{\text{wire}}}{\partial U} = \frac{nBU^{n-1}}{2} \left[\frac{R_{\text{wire}} (T_{\text{wire}} - T_{\infty})}{A + BU^n} \right]^{\frac{1}{2}} \quad (2.15).$$

Temperature sensitivity $S_{\theta,CT}$ can be calculated as:

$$S_{\theta,CT} = \frac{\partial E_{\text{wire}}}{\partial \theta} = -\frac{1}{2} \left[\frac{R_{\text{wire}} (A + BU^n)}{(T_{\text{wire}} - T_{\infty})} \right]^{\frac{1}{2}} \quad (2.16),$$

where θ are small fluctuations in the surrounding temperature T_{∞} [55].

HWA can be used in two regimes – constant temperature (CT) and constant current (CC) anemometry. All our experiments were carried out in the constant temperature regime. Figure 2.13 shows the wiring of the HWA in the CT regime.

In the constant temperature (CT) regime of HWA, the temperature of the wire is maintained constant. The voltage change $E_2 - E_1$, which is proportional to the resistance change

of the wire, results from the fluid velocity change. The signal $E_2 - E_1$ is led into the amplifier, where the supply current I is modified to keep the wire temperature constant, [55].

2.3.1.2 OVERHEAT RATIO

An important parameter of probes working in a CT regime is the so-called “overheat ratio” a_h :

$$a_h = \frac{R_{\text{wire}}}{R_{\infty}} \quad (2.17)$$

and it is a guide for adjusting the wire temperature, [55]. From Equations (2.15) and (2.16), it follows that the velocity and temperature sensitivity of the probe is directly dependent on the selection of the overheat ratio. Therefore, for velocity measurement, it is recommended select an overheat ratio as high as possible (maximum values are limited by the material properties of the wire, especially by a tendency toward faster corrosion at higher temperatures). For experiments in water, the overheat ratio is limited by the boiling temperature of water and by the influence of buoyancy measurements.

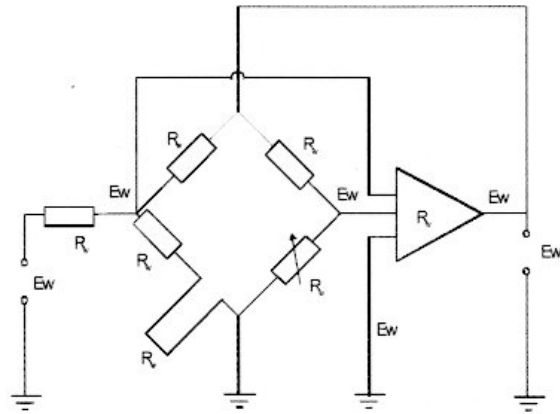


Fig.2.13 Wheatstone bridge for anemometer operating in CT mode

2.3.1.3. VELOCITY CALIBRATION

Precise calibration of the probe has to be done to obtain good quality results. Calibration is used to determine the constants in established calibration relations for velocity measurement $E = f(U)$ and for temperature measurement $E = f(T)$.

The most common relations for HWA calibration are [55]:

1. The power law (King's law) [58]: $E^2 = A + BU^n$ (2.18),

2. The extended King's law $E^2 = A + BU^{0.5} + CU$ (2.19),

3. Polynomial curve fit [63] $U = A + BE^2 + C(E^2)^2 + D(E^2)^3$ (2.20),

King's law – King proposed $n = 0.5$, but results from Collins and Williams have shown that a better curve fit is $n = 0.45$ for $0.02 < Re < 44$. Based on later experiments, the value n is considered as various parameters. The optimal value for a typical $5\mu\text{m}$ wolfram probe is $n = (0.4-0.45)$.

Extended King's law – Van der Hegge Zijnen [59] proposed to use a non-dimensional heat transfer equation for a large range of Reynolds number $0.01 < Re < 500,000$:

$$Nu = 0.35 + 0.5Re^{0.5} + 0.001Re \quad (2.21).$$

A similar relation was later proposed by Richardson [60] and Fand and Keswani [61]. Davies and Patrick [62] applied this relation in the form $E^2 = A + BU^{0.5} + CU$ for a heated wire probe, where U can be obtained by a simple inversion process.

Polynomial curve fit – George *et al* [64] established a polynomial equation in the form:

$$U = A + BE + CE^2 + DE^3 + \dots \quad (2.22).$$

The expression of the velocity U in polynomial form from E has the advantage that the requested velocity U can be expressed directly from equation (2.22).

During our experiments, a towing tank at TUL (see Appendix 7) was used as the calibration equipment. In a long enough towing tank (5.5m for the present case), the probe can be moved in quiescent water with a constant velocity (in a range from 0.001 m/s to 0.25 m/s). The velocity is known, the probe voltage is measured, and the calibration constants for the chosen equation (2.18-2.20) can be easily evaluated. In the present study, the calibration form of equation (2.22), namely, a third-degree polynomial, was used.

2.3.1.4 USING HWA IN WATER

The HWA method can be used for measurements in water and in other fluids, [55]. Hot film probes should be used for these measurements. A few issues must be considered to obtain reliable results:

Bubble formation on the probe: It has been observed that this problem is caused by bubbles in water. It is recommended to allow the water to rest (long enough) before use. The effect can be also eliminated by restricting the temperature difference between the film and water to approximately 20°C. The corresponding overheat ratio $a_h = R_{\text{wire}} / R_{\infty} = 1.05 - 1.1$ and its value depend on the material used (platinum or nickel), [55].

Cavitation: Cavitation can be caused by high velocities and is connected with bubble formation on the wire. For a 25 μm or 50 μm diameter probe, it is about 9 ms^{-1} or (4.5-6) ms^{-1} , [55].

2.3.1.5 HWA SETUP USED

For experiments, the DANTEC system was used: hot-film probe 55P36, anemometer 90C10, bus bar NI_CA1000, and A/D converter NI-PCI-MIO-16E-1. The measured data was analyzed in StreamWare 3.01 and Microsoft Excel.

2.3.2 LASER DOPPLER VIBROMETRY

2.3.2.1 PRINCIPLE

Measurement of the oscillating PCT membrane is based on the Laser Doppler Vibrometry (LDV) principle. LDV is a non-contact vibration measurement technique utilizing the Doppler Effect. LDV permits the measurement of hot, miniature, or soft surfaces, even under

water, without mass-loading. A laser Doppler vibrometer is based on a detection of the Doppler shift of coherent laser light that is scattered from a small area of a test object. The object scatters or reflects light from the laser beam, and the Doppler frequency shift is used to measure the component of velocity, which lies along the axis of the laser beam, [65, and 66].

The Ometron VH-1000-D (B&K 8338) Portable Digital vibrometer is used to measure the velocity of the oscillating membrane. This kind of vibrometer measures a vibrational velocity according to the heterodyne interferometer principle, which generates a high-frequency carrier signal at the photo detector with the aid of a Bragg cell. The beam of helium neon laser is pointed at the vibrating object and scattered back from it. The velocity and amplitude of a vibrating object generate a frequency or phase modulation due to the Doppler effect. The object beam is thereby subjected to a small frequency shift, which is described as the Doppler frequency f_D . The Doppler frequency is a function of the velocity component v in the direction of the object beam according to:

$$f_D = 2 \frac{v}{\lambda} \quad (2.23),$$

where λ is the laser wavelength, [66]. The Bragg cell also generates an optical frequency shift f_B in the reference beam. After superimposing the measurement and the reference beam, an electrical signal is generated at the photo detector with instantaneous frequency:

$$f_C(t) = f_B + f_D(t) = f_B + 2 \frac{v(t)}{\lambda} \quad (2.24).$$

This is a carrier frequency signal with a center frequency f_B , which is the frequency modulated with the Doppler frequency $f_D(t)$. Through frequency demodulation, the velocity signal can be decoded. In the VH-1000-D, demodulation of the Doppler signal is based purely on a digital process, [66]. For signal processing, an analog signal output with 24-bit amplitude resolution is available.

2.3.2.2 VIBROMETER PARAMETERS

The main parameters of the vibrometer VH-1000-D are the following, [65, 66]:

- Frequency range: 0.5Hz - 22kHz
- Measurement ranges (full scale (peak-peak)): 20 mm/s, 100 mm/s, 500 mm/s
- Spurious free dynamic range (SFDR): > 90 dB
- Best resolution: $0.02 \mu\text{m/s/Hz}^{0.5}$

The response of a PCT to a harmonic driving signal at frequency $f = 15\text{Hz}$ was measured. The LabView software was used to acquire and analyze the signal obtained from the Ometron vibrometer. Microsoft Excel was used for additional calculations and analysis.

2.3.3 TIN ION VISUALIZATION

Tin ion visualization (or electrolytic precipitation method) is used for SJ and SJ array primary structures visualization. It helps to evaluate the basic character of the flow. This method is based on the tin ion transfer from an anode to a cathode in an electrolytic solution, described by Honji and Taneda [67]. For our experiments, a tin wire with a diameter $d = 0.5 \text{ mm}$ was

used as the anode. A copper stick with a diameter 6 mm and length 140 mm was used as the cathode. A SJ nozzle was submerged into an electrolytic solution (mix of water and salt). The tin wire was attached close to the SJ orifice. Tin ions from the anode were released after DC voltage was applied. The particles were visible as a “white streak lines” with a very low sedimentation velocity. This method is very useful for velocities up to 5 cm/s, while the particle production is not sufficient at higher velocities, [68].

Experiments are performed at a frequency of $f=15\text{Hz}$. For electrolysis, a voltage of $E=30\text{V}$ and a current of $I=0.1\text{A}$ were used. For lighting, a continuous laser ND:YV04 with a power output of 300 mW and a laser for PIV system New Wave Geminy with output energy of 120 mJ in each pulse were used. By means of a cylinder optic, a thin light sheet was made, wherein the movement of tin ions was visible.

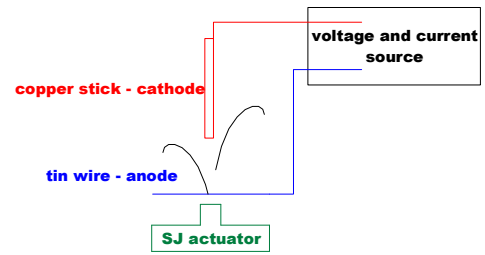


Fig.2.14 Schematic drawing of visualization

2.3.4 PARTICLE IMAGE VELOCIMETRY

2.3.4.1 PRINCIPLE

Particle Image Velocimetry (PIV) is used for channel flow and SJ/SJ array measurement. It is a non-intrusive laser optical measurement technique for research and diagnostics of flow, turbulence, microfluidics, spray atomization and combustion processes [37]. In PIV, the velocity vectors are derived from sub-sections of the target area of the particle-seeded flow by measuring the movement of particles between two light pulses:

$$v = \frac{\Delta l}{\Delta t} \quad (2.25),$$

where v is the flow velocity component, Δl is the particle displacement and Δt is the time of the particle displacement, see e.g. [56].

Figure 2.15 shows the principle of a PIV system. The measurement fluid has to be transparent enough. The small particles are put into this flow environment. The particles are illuminated in the target area with a laser light sheet. A camera lens images the target area onto the sensor array of a digital camera. The camera is able to capture each light pulse in

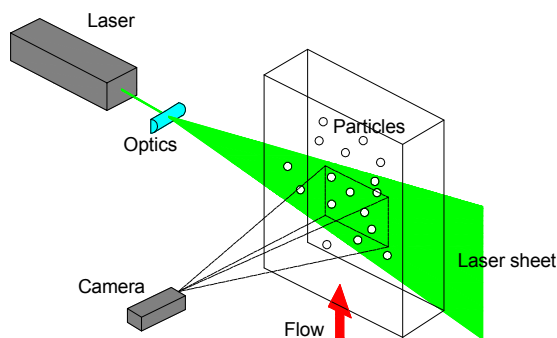


Fig.2.15 Principle of PIV measurement

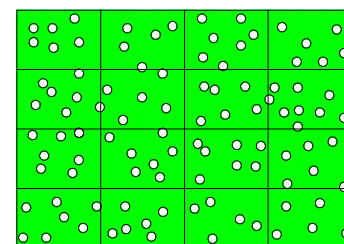


Fig.2.16 Interrogation areas

separate image frames. Once a sequence of two light pulses is recorded, the images are divided into small subsections called interrogation areas (IA) – see Figure 2.16. The interrogation areas from each image frame, I_1 and I_2 , are cross-correlated. The correlation produces a signal peak, identifying the displacement, Δl . An accurate measurement of the displacement – and thus the velocity – is achieved with sub-pixel interpolation of the cross-correlation signal. A velocity vector map over the whole target area is obtained by repeating the cross-correlation for each interrogation area (with one vector for each interrogation area) over the two image frames captured by the camera [56].

2.3.4.2 IMAGES ANALYSIS

For image, recording two cases are used:

- Double exposure – the start and end positions of the particles are recorded onto the same image.
- For a single exposure, two images are used. The first image is for the start position of the particles and the second is for their end position.

According to the image scanning case, the correlation function for the displacement mean value in a given area is used [69]. For a double exposure, the autocorrelation is used for data analysis. According to the data in the form of the brightness value in specific camera pixels, the calculation of discrete autocorrelation is:

$$\Phi_{ff}(m, n) = \sum_{k=-\infty}^{k=\infty} \sum_{l=-\infty}^{l=\infty} f(k, l) \cdot f(k + m, l + n) \quad (2.26).$$

Functional value $f(k, l)$ is light intensity recorded with the detector on pixel position (k, l) . The result is a correlation map. For autocorrelation, there are three peaks (see Figure 2.17). The main peak is in the middle of the autocorrelation level, and it is the comparison of itself (zero displacement). The next two peaks are smaller and symmetrically distributed around the central peak. By comparing each vector with all others, two times the same displacement with opposite orientation can be calculated. It is not clear which point is initial and which is the end. The directional ambiguity ensues from that. This problem can be solved by using a

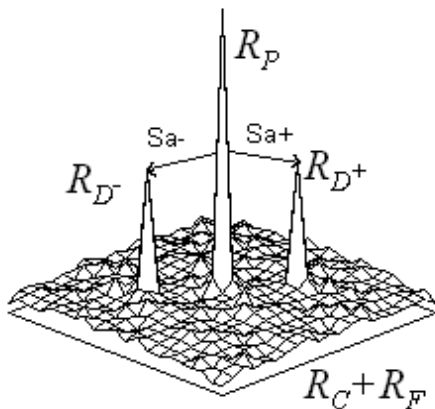


Fig.2.17 Graphical presentation of autocorrelation: R_P is the central vector of the autocorrelation. Sa is the resulting vector of the average displacement in this interrogation area between central peak R_P and peaks R_{D^-} , R_{D^+} . $R_C + R_F$ is the value of the correlation noise.

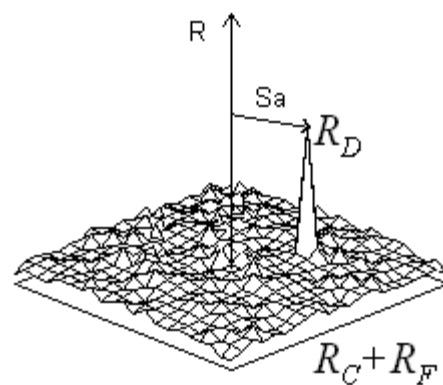


Fig.2.18 Graphical presentation of cross-correlation

suitable offset, [69].

More often, a cross-correlation is used. It investigates two separately exposed images. The equation of the cross-correlation discrete calculation is:

$$\Phi_{fg}(m, n) = \sum_{k=-\infty}^{\infty} \sum_{l=-\infty}^{\infty} f(k, l) \cdot g(k + m, l + n) \quad (2.27).$$

Figure 2.18 shows the cross-correlation result. In this case, there is no question about the start and final positions of the particle. Therefore, the correlation plane delivers an unambiguous result. There is only one peak and its joining with a correlation plane center determines the resulting shift vector [69].

For this result, a vectoring map can be created. The vectoring map shows velocity vectors from the entire measured plane between two moments. Figure 2.11 (Chapter 2.2.4) shows the vectoring map after incorrect values filtering.

For correlation calculations, the fast Fourier transformation (FFT) is used. The time-consuming computation of a correlation is replaced with a conjugate multiplication of corresponding coefficient pairs of Fourier images of light intensity functions. The correlation function is obtained back with reverse Fourier transformation of the result. Figure 2.19 shows the calculation using FFT, [69].

Window function

The main failure of PIV is the creation of “lost pairs”. The “lost pairs” are generated when the particle leaves the area in the period between two expositions (more about “lost pairs” is described in paragraph 2.3.5.3 below). Lost pairs increase the noise value in the correlation plane. The next correlation noise enhancement features FFT calculation. Both of these problems occur at most around the borders of the investigated area. A special window function assigns a low importance to the particle image near the borders thereby decreasing its influence on the correlation calculation. In practice, the Gauss function and the so-called “Top-Hat” function are used. The “Top-Hat” function assigns zero importance to points near the borders and more importance to those points in the middle of the interrogation area. With application of window functions, the information concerning large quantity particles movement is lost. The interrogation area overlap solves this problem, [69].

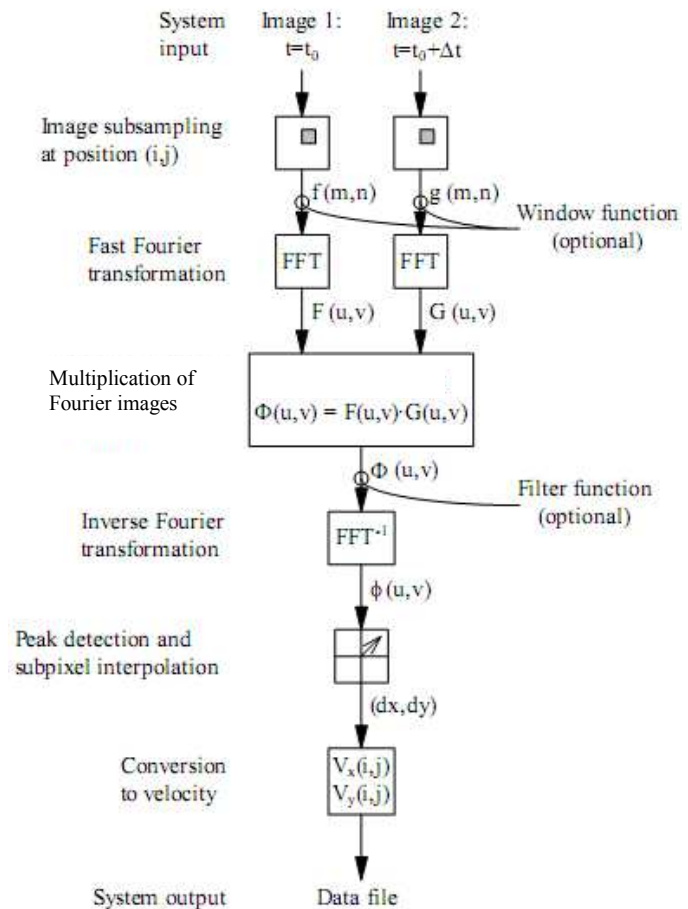


Fig.2.19 Computation of vector map with use of FFT, [69]

Overlap of the interrogation area

The overlap is the next possibility to improve the vector map calculation. Figure 2.20 shows the principle of the overlap. When using a window function, the information about particles at the borders of the interrogation areas is not effectively utilized. When using the overlap, information about the hidden border particles in the first area can be obtained by processing in the adjacent area; thereby reducing data loss when using the windows, [69].

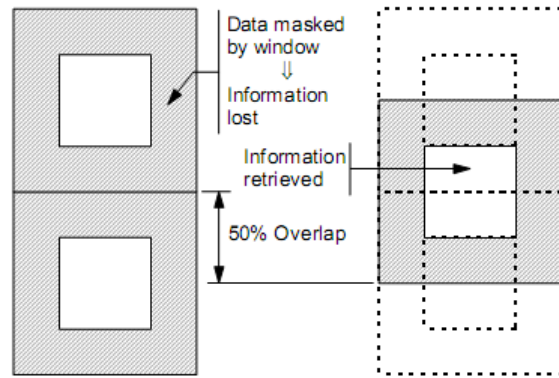


Fig.2.20 Principle of interrogation areas overlap, [69]

Sub-pixel interpolation

Sub-pixel interpolation is able to more exactly determine information about peak location in the correlation plane – height, width, and place. Without interpolation application, the maximum achievable accuracy is limited by the resolution of the camera used. Therefore, it is not possible to detect the peak parameters beyond an accuracy of one pixel. For higher accuracy, it would be advantageous, when possible, to place the correlation peak between the defined pixels. This can be achieved by an interpolation with the Gaussian curve, for example. For its interlay, it needs three points. These points represent an image of the particular particle, [69]. If the particle does not interfere directly in at least three pixels of a sensor array, it is advantageous to blur the camera and thereby extend the image.

Another possibility is to extend the correlation peak with special filters at the detriment of its height. Its width must fall within a certain interval. If the top is too thin, it is not possible to correctly interline the points for sub-pixel interpolation because the interpolation can also be affected by small high-frequency noise due to the large width. This operation cannot change the position of the peak in a plane and does not influence the determination of the resulting displacement, [69].

Offset of second correlation area

By default, the interrogation areas are located at the same position within the first and the second camera image maps. The resulting measurable particle displacement is $\pm 1/4$ of the length of the side of the interrogation area. However, it is possible to shift the velocity range by offsetting the second interrogation area relative to the first, so that the range of measurable displacements are no longer symmetric around zero, [69].

After correlating the particle image in interrogation area 1 with the particle image in interrogation area 2, the resulting measurable displacement now equals the offset $\pm 1/4$ of the size of the interrogation area.

Ideally, the offset should correspond to the average particle displacement, so that every seeding particle in interrogation area number 1 corresponds to a seeding particle in interrogation area number 2, and so that both particles in such a pair are located at the same position within their respective interrogation areas. In this way, the “lost pairs” can be minimized since in-plane motion is eliminated, and out-of-plane motion is the only remaining source of the problem.

The same offset value is applied to the entire investigated field, and should thus be chosen on the basis of the known or expected average particle displacement for the entire field, [69].

2.3.4.3 LASER AND SYSTEM SYNCHRONIZATION

For our experiments, a unit “Timer box” and DynamicStudio v.2.30 (DANTEC) software were used. All the control boards of the lasers, cameras, and timers of the input and output signals were placed directly into the main computer. DynamicStudio is a control and processing program for the unit Timer box. The system allows the computer

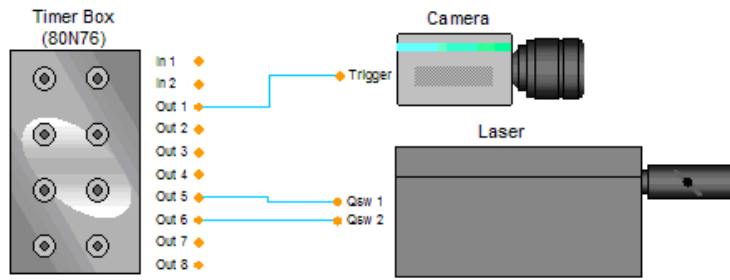


Fig.2.21 A unit *Timer box* with signals for laser and camera

to take on the role of a measuring center. Data communication between the PC, laser, and cameras runs through the internal protocols of the DynamicStudio control software and are impossible to modify. Starting signals are taken out by means of a National Instruments PCI-6601 counting measuring card into the unit Timer box with eight BNC connector outputs and two inputs (see Figure 2.21).

Signals for the start of every flash lamp and Q-switching of the laser are led through one cable, whose position it is necessary to define – to Timer box to connect the starting trigger signal into two inputs.

Figure 2.22 shows the principle of basic synchronization. From the SJ signal generator, the TTL signal goes into the PC (Timer box). The laser and camera start with the leading edge of the TTL. The starting point of measurement is changed during the SJ period and, therefore, the whole period is measured.

The delay inside the electronic synchronization devices does not exceed $3\mu\text{s}$.

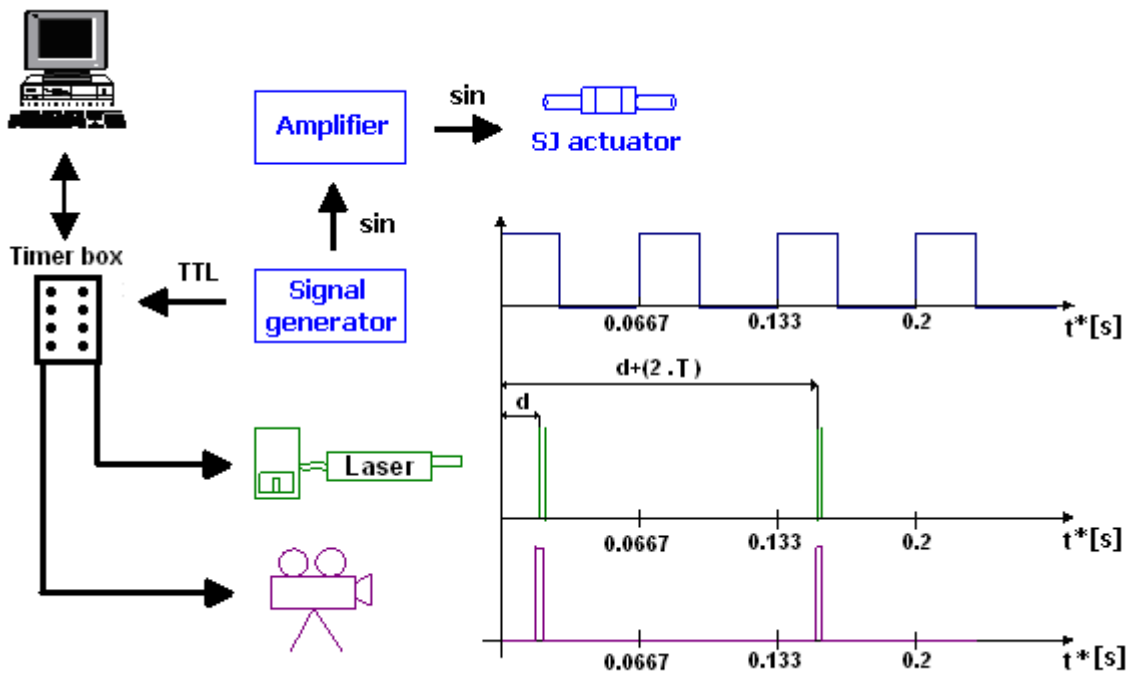


Fig.2.22 Schematic of basic synchronization for PIV measurements (T means the period), modified by [70]

2.3.4.4 SETUP PARAMETERS

In the present study, two PIV systems were used:

- Parameters for the PIV system at the Eindhoven University of Technology (TU/e)

Experiments at TU/e were performed with a channel flow without a SJ and with a channel flow interacting with a single SJ. Seeding particles were polyamide balls¹ with diameters of 20 μm (DANTEC), which have a density comparable to water. The particles were illuminated by a double pulse laser with a maximum 200 mJ per 5ns pulse, at a repetition rate of 2 x 15Hz. A typical delay time of 30 ms was used. The laser beam was expanded by a cylindrical lens into a light sheet of about 1mm in thickness. The image pairs were acquired using a 10-Bit CCD Kodak ES 1.0 camera with a spatial resolution of 1008 x 1018 pixels and a maximum rate of 30 frames/s. The resulting vector maps were averaged over 54 double pulses in sequence. Velocity vectors were determined by adaptive correlation using interrogation windows of 32 x 32 pixels at a 50% overlap and by cross-correlation using interrogation windows of 64 x 32 pixels at a 50% overlap, respectively. Adaptive correlation was used on the images, which shows the SJ flow in the direct vicinity of the actuator; cross correlation was used on the images father from the SJ actuator. Data processing was done using FlowManager 4.71 (DANTEC) software.

- Parameters for the PIV system at the Technical University of Liberec (TUL)

Experiments were focused on a single SJ and on a SJ array – both either with or without a channel flow. Two kinds of seeding particles were used: polyamide balls with diameters of 20 μm (DANTEC) and fluorescent rhodamin coated particles² with diameters of 10.2 μm (Microparticles GmbH). The particles were illuminated by a double pulse laser with a maximum 125 mJ per 10 ns pulse at a repetition rate of 2 x 15Hz. The typical delay time between two pulses was 5 ms.

The laser beam was expanded into a light sheet of approx. 1 mm thick. The image pairs were acquired using the HiSense MKI camera (DANTEC) with a spatial resolution of 1280 x 1024 pixels.

The resulting vector maps were averaged over 100 PIV records. Velocity vectors were determined by adaptive correlation using interrogation windows of 32 x 32 pixels at a 25% overlap. Data processing was done using DynamicStudio 2.21 commercial software (DANTEC).

2.3.5 UNCERTAINTY ANALYSIS

2.3.5.1 UNCERTAINTY OF CTA MEASUREMENTS

The uncertainty model combines uncertainty contributions $U(y_i)$ from each individual input variable x_i into a total uncertainty at a given confidence level, [57]. The output variable is defined as:

¹ The advantage of polyamide balls is that they have the same as water, which guarantees accurate measurement of the flow. The disadvantage is tendency for the particles to become attached to channel walls and their consequential high reflection.

² The advantage of rhodamine coated particles is the negation of the influence of bubbles in water, foreign matter drift with flow, and reflection from walls. During measurement, the camera's narrow-band filter is used.

$$y_i = f(x_i) \quad (2.28).$$

The relative standard uncertainty $u(y_i)$ is a function of the standard deviation of the input variance:

$$u(y_i) = \frac{1}{y_i} S \left(\frac{\Delta x_i}{k_i} \right) \quad (2.29),$$

where $S = \frac{\partial y_i}{\partial x_i}$ is the sensitivity factor and k_i is the coverage factor related to the distribution of the input variance.

The uncertainty of the results obtained with a CTA anemometer is a combination of the uncertainties of the individually acquired voltages converted into velocity and the uncertainty of the statistical analysis of the velocity series.

Anemometer

Commercially available anemometers have low drift, low noise, and good repeatability, so that these factors do not add significantly to the uncertainty in comparison with other error sources. In certain applications, e.g. dissipation measurement, the high frequency noise of the anemometer may be significant, [57].

The frequency characteristic of the anemometer will not add to the uncertainty when the frequencies in the flow are below approximately 50% of the cut-off frequency (from the square wave test), as the characteristic is normally flat up to this point, [57].

Calibration equipment

The calibration performed with a dedicated calibrator constitutes a major source of uncertainty, [57]. The error is stochastic with a normal distribution, and the relative standard uncertainty can be expressed as:

$$U(U_{\text{cal}}) = \frac{1}{100} \text{STDV}(U_{\text{cal}}(\%)) \quad (2.30).$$

The calibrator uncertainty is often given as a relative standard uncertainty, a_{cal} , in percent plus a constant contribution b_{cal} in m/s:

$$\text{STDV}(U_{\text{calibrator}}) = \pm a_{\text{cal}}(\%) + b_{\text{cal}}(m/s) \quad (2.31).$$

For a good dedicated calibrator, the values are: $a_{\text{cal}} = \pm 1\%$ and $b_{\text{cal}} = \pm 0.02 m/s$. The constant contribution b_{cal} can usually be neglected at velocities above 5m/s, [57].

Linearization (Conversion)

The linearization uncertainty is related to curve fitting errors. It is stochastic with a normal distribution, and its relative standard uncertainty can be calculated from:

$$U(U_{\text{lin}}) = \frac{1}{100} \text{STDV}(\Delta U_{\text{lin}}(\%)) \quad (2.32),$$

where $STDV(\Delta U_{lin})$ is the standard deviation of the curve fitting errors in the calibration points in %, [57].

A/D board resolution

The resolution uncertainty is stochastic with square distribution, and its relative standard uncertainty can be expected as:

$$U(U_{res}) = \frac{1}{\sqrt{3}} \frac{1}{U} \frac{E_{AD}}{2^n} \frac{\partial U}{\partial E} \quad (2.33),$$

where E_{AD} is the A/D board input range, n is its resolution in bits, U the velocity, and $\frac{\partial U}{\partial E}$ is the slope (sensitivity factor) of the inverse calibration curve, $U = f(E)$, [57].

Probe positioning

The positioning uncertainty is related to the alignment of the probe in the experimental set-up after calibration. The uncertainty is stochastic with square distribution, and its relative standard uncertainty can be expected as:

$$U(U_{pos}) = \frac{1}{\sqrt{3}} (1 - \cos \theta) \quad (2.34).$$

Normally a probe can be positioned with an uncertainty of $\Delta\theta = 1^\circ$, [57].

Temperature variations

Temperature variations from calibration to experiment or during an experiment introduce systematic errors. If not corrected, a change in temperature changes the sensor over-temperature and contributes to a stochastic uncertainty with rectangular distribution. The relative standard uncertainty is:

$$U(U_{temp}) = \frac{1}{\sqrt{3}} \frac{1}{U} \frac{1}{T_w - T_0} \left(\frac{A}{B} U^{-0.5} + 1 \right)^{0.5} \quad (2.35).$$

where T_w is the sensor temperature, T_0 the ambient reference temperature, and ΔT is the difference between the ambient reference temperature and the temperature during the measurement, [57].

Ambient pressure variations

Changes in ambient pressure also influence the density and hence the calculated velocity. It contributes to a stochastic uncertainty with rectangular distribution with a following relative standard uncertainty, [57]:

$$U(U_{\rho,P}) = \frac{1}{\sqrt{3}} \left(\frac{P_0}{P_0 + \Delta P} \right) \quad (2.36).$$

2.3.5.2 UNCERTAINTY OF LDV MEASUREMENTS

Measurement range

The VH-1000-D offers three velocity measurement ranges, with the corresponding full scale values shown in mm/s (20mm/s, 100mm/s, and 500mm/s). If the full scale values are divided by the four corresponding values of the output voltage swing of $\pm 4V$, it produces the respective scaling factors for the analog output signal as $\frac{\text{mm}}{\text{s}}/V$ ($5 \frac{\text{mm}}{\text{s}}/V$, $25 \frac{\text{mm}}{\text{s}}/V$, and $125 \frac{\text{mm}}{\text{s}}/V$).

Generally, the smallest possible measurement range, which is not exceeded under the given measurement conditions, should be used to optimize the signal-to-noise ratio. Coming close to the exceeded measurement range (94% of the full scale) is indicated by a circular symbol on the vibrometer display. A brief appearance of the over range indicator does not necessarily mean the measurement is causing over range, as noise peaks caused by brief disruptions of the optical signal level can trigger the display. However, when using the filters, it is also possible that an internal overload outside the frequency pass band has occurred. In this case, the over range indicator would appear without over range being apparent in the output signal. Despite this, the next highest measurement range would have to be selected to avoid waveform distortions, [66].

If the display over range indicator is lit up continuously, it means that the measurement range is being exceeded. In this case, the next highest measurement range has to be selected, [66].

Low pass filter

The VH-1000-D is equipped with switchable, digital low pass filter. Unlike typical analog filters, the three selectable limit frequencies of 1 kHz, 5 kHz, and 22 kHz mark the upper frequency limit for precise amplitude measurements (flatness $\pm 0.1\text{dB}$), but not the -3 dB point. The changeover to the stop band has a steep frequency roll-off of 120 dB/dec, resulting in an effective suppression of noise and higher frequencies, [66].

High pass filter

To suppress low-frequency background vibrations, the VH-1000-D is equipped with a switchable 3rd order Butterworth high pass filter with a cutoff frequency of 100 Hz (-3 dB).

The high pass filter is beneficial for signal acquisition if it is working with high-level background noise, e.g. caused by machine vibrations, while measuring a relatively small, desired signal at high frequencies.

Attention has to be paid to the following properties of the high pass filter:

- The changeover from the pass band to the stop band occurs with a more gradual frequency roll-off (-60 dB/dec) than with low pass filters.
- A significant amplitude error occurs near the cutoff frequency
- For frequencies >140 Hz, the amplitude error is <-0.5 dB (-5%).

2.3.5.3 UNCERTAINTY OF PIV MEASUREMENTS

The limitation of PIV consists of particle size, flow velocity, and saturation.

The main limiting condition is the interrogation area length and its maximal displacement. The maximal particle displacement should not be more than a quarter of the interrogation area length. The equation for maximal velocity is:

$$|v_{\max}| = \frac{d_1}{4M\Delta t} \quad (2.37),$$

where d_1 is size of interrogation area, M is an enlargement, and Δt is the time between two expositions.

One of the errors is linked with the “lost pairs”. Lost pairs are caused when the particle leaves or enters the interrogation area between two light pulses. This particle does not have a twin in a second image, thereby causing random correlations. With higher velocity particles, the probability of leaving the interrogation area is higher. Then the particles with smaller velocities have higher influence, and the resulting velocity looks lower than in reality. This phenomenon is called the error of velocity taking down to zero.

Saturation

Another important parameter is the particle saturation of the flow. Low saturation increases the probability that the particle leaves the interrogation area between two expositions. This causes the correlation level noise rate to increase and measurement accuracy to decrease. A recommended value of particle saturation is 5 particles in the area for cross correlation and 10 particles for autocorrelation.

Measurement accuracy

To correctly understand flow character, it is important to select a suitable size for the interrogation areas. To suppress the “lost pairs” error, it is necessary to choose large enough areas. Nevertheless, for better space resolution, a sufficient quantity of vectors is need. Finding a compromise between these two requests depends on the user’s skill. The application of offset, overlap, window function, filters, etc. eliminates incurred errors. However, none of these operations inserts any new information into the process. Conversely, these applications can entirely misrepresent the results. In any case, they do not provide any information about what happens in the flow in the time between two expositions. When a more detailed view of the flow is required, it is necessary to adapt this time period. The main limits are the actual possibilities of pick-up technique, lasers, and the analyzing equipment used, [56, 69].

2.3.5.4 UNCERTAINTY OF USED MEASURING DEVICES

The experimental setup consisted of the following measuring devices: a Tektronix AFG 3102 signal generator, an Omnitronic MPZ-180 amplifier, a UNI-T UT70B voltmeter, a PU 510 ampere meter, and a Tektronix TDS 1012 oscilloscope.

Tektronix AFG 3102 signal generator

The frequency range, in our case a sinus waveform, was 1 μ Hz to 100 MHz. The resolution of selected frequency was 1 μ Hz of 12 digits. Accuracy was ± 1 ppm.

The range of signal amplitude was 20 mV_{peak-peak} to 10 V_{peak-peak}. The amplitude accuracy was $\pm (1\% \text{ of setting} + 1\text{mV})$ at 1 kHz sine waveform, amplitude $> 10 \text{ mV}_{\text{peak-peak}}$. 0 V offset.

Omnitronic MPZ-180 amplifier

During measurements at a frequency of 1 kHz, there can be a distortion of 0.5%.

UNI-T UT70B digital voltmeter

For our measuring range of up to 40V effective and AC voltage, the resolution was 10mV, and accuracy was $\pm (1\% \text{ of reading} + 5 \text{ digits})$.

PU 510 digital ampere meter

For AC, the accuracy of the ampere meter was $\pm (1\% \text{ of reading} + 0.5\% \text{ of full scale})$.

Tektronix TDS 1012 oscilloscope

An oscilloscope was used to measure the peak-to-peak value of the amplified signal from the signal generator. DC vertical accuracy was $\pm 3\%$.

CHAPTER 3

EXPERIMENTAL RESULTS

Five types of measurements were performed:

- Channel flow without interaction of a single SJ or SJ array,
- Single SJ in quiescent fluid,
- SJ array in quiescent fluid,
- Single SJ interacting with a channel flow,
- SJ array interacting with a channel flow.

As mentioned in Chapter 2, PIV experiments were performed with two different PIV systems and with two different circulation water channels. First, the experiments at TU/e in Eindhoven were conducted. Therefore, the measurement conditions (as well as the Plexiglas channel dimensions and the setting of the channel flow velocity) were adapted to this system's possibilities. Subsequent experiments at TUL in Liberec and at IT CAS in Prague were adjusted to these conditions.

In this thesis, three definitions of time origin are used: t^* is the time related to the leading edge of the TTL signal (used for LDV experiments and phase averaging of HWA results), t^{**} is related to the zero position of the membrane center at the maximum extruded velocity, and t is related to the beginning of fluid extrusion from the SJ actuator (i.e. at zero velocity of the fluid and maximum membrane displacement). These definitions will be demonstrated in Figure 3.8, with an explanation in paragraph 3.2.3 below.

3.1. CHANNEL FLOW

3.1.1 CHANNEL FLOW USING CHANNEL AT TU/E (EINDHOVEN)

The first phase of the experiments was to visualize and measure the channel flow without the interaction of a SJ or SJ array. The reason for this experiment was to detect and set the laminar channel flow. For the first view of the flow, simple ink visualization was used – see Figure 3.1. The ink was inserted about 1m upstream from the test section. The laminar parabolic profile of the channel flow corresponds quite well with the theoretical laminar parabolic profile.

For a more precise measurement, the PIV method and polyamide particles were used. The typical time-mean velocity profile for the (main) channel flow without SJ interaction can be seen in Figure 3.2. It is easy to see that the measured profile compares very well with the parabolic Poiseuille profile (denoted by U):

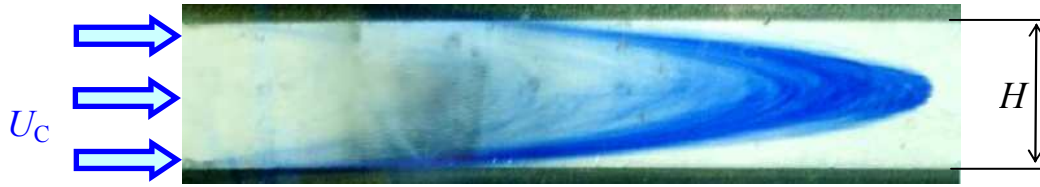


Fig.3.1 Visualization of the laminar channel flow at Reynolds number $Re_C = U_C 2H/\nu = 480$; results from the experiments conducted at TUE (NL) – presented in [A16]

$$U = 6 \cdot U_C \left[y/H - (y/H)^2 \right] \quad (3.1),$$

where the origin of the crosswise coordinate y is chosen on the bottom wall of the channel – see Fig. 2.4.

Figure 3.2 indicates that the velocity on the channel wall is not zero (see the position $y = 40$ mm). Obviously, this cannot be true. This error is typical for near-wall PIV measurements, and it is caused by Plexiglas reflection. The reflections from the wall and from the polyamide particles look like “white fog”, which prevents proper post-processing near the wall. Reflections from the wall at distance $y = 0$ mm are rather well suppressed since this wall was painted black.

The velocity profile was measured approximately in one-half of the channel length at location $x = 0$ (see Fig. 2.4). Note that the channel flow field at this point can be considered to be fully developed, as was discussed in Chapter 1.1.1, [80].

For evaluation of the Reynolds number, the time-mean velocity through the channel cross section was considered as $U_C = (2/3) \cdot U_{max}$ (for the two-dimensional case), and it is approximately $U_C = 0.006$ m/s. The Reynolds number of the channel flow was evaluated as $Re_C = 480$.

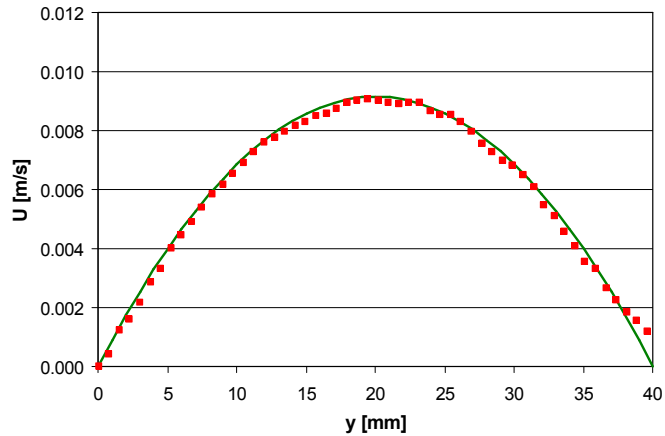


Fig.3.2 Velocity profile of a channel flow without SJ; results obtained at TU/e (Eindhoven). red points– PIV measured profile, green line - parabolic Poiseuille profile, Eq. (3.1)

3.1.2 CHANNEL FLOW USING CHANNEL AT IT CAS (PRAGUE)

Figure 3.3 shows the PIV results of a channel flow using a circulation channel at IT CAS (see Figure 2.8). Figure 3.3a compares the velocity laminar profile with the parabolic Poiseuille profile (using Eq. (3.1)). This profile was measured at an approximate distance of 520mm from the beginning of the Plexiglas wall in a plane of SJ array orifices axis $x = 0$ (see Fig. 2.8b and Appendix 4). Figure 3.3b presents the

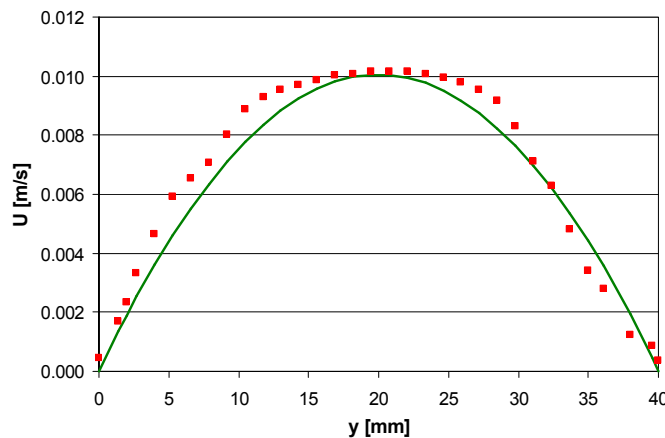


Fig.3.3a Velocity profile of a channel flow without SJ; results obtained at IT CAS (Prague). red points – PIV measured profile, green line - parabolic Poiseuille profile, Eq. (3.1)

results in the form of velocity magnitude vectors.

Similar to above, the time-mean velocity through the channel cross section was evaluated as $U_C = (2/3) \cdot U_{max} = 0.0067$ m/s, and the relevant Reynolds number was $Re_C = 536$.

Figure 3.4 compares both velocity profiles in a dimensionless form. The profiles shapes look quite similar. Each profile is relative to the corresponding U_C .

To demonstrate the three-dimensionality of the real channel flow, Figure 3.5a shows the velocity profile $U(z)$. The transformation into a dimensionless form is shown in Fig. 3.5b. It is clear that the velocity profile is not fully developed (compared with Figure 3.3). This confirms that the channel flow can be assumed to be 2D, i.e. flow between two parallel walls.

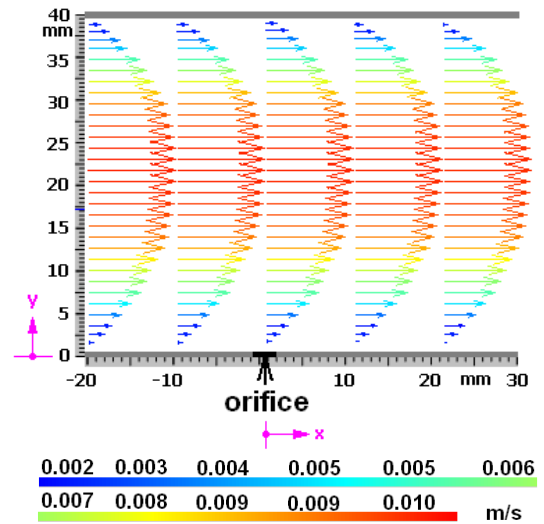


Fig.3.3b PIV results of velocity laminar profile in the form of velocity magnitude vectors; results from IT CAS

3.2. SINGLE SYNTHETIC JET

This part describes the behavior of a single SJ. Good understanding of a principle of a single SJ leads to right proposal of SJ array. During experiments dealing with frequency characteristics (chapter 3.2.1), the actuator was fed with a sinusoidal AC signal of a true rms AC voltage of (18.6-19.3) V. The true rms AC current was (38.5-45.0) mA, and the apparent electric power (the product of the true rms AC voltage and current) was 0.8W.

During additional experiments (chapters 3.2.2-3.2.6), the actuator was fed with a sinusoidal AC signal at the

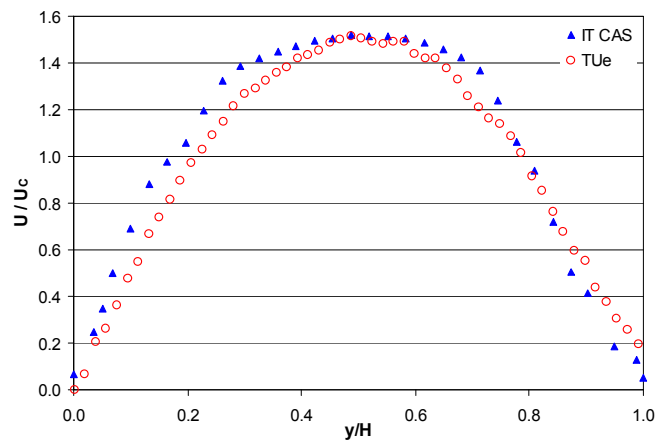


Fig.3.4 Comparison of channel velocity profiles from TU/e and IT CAS

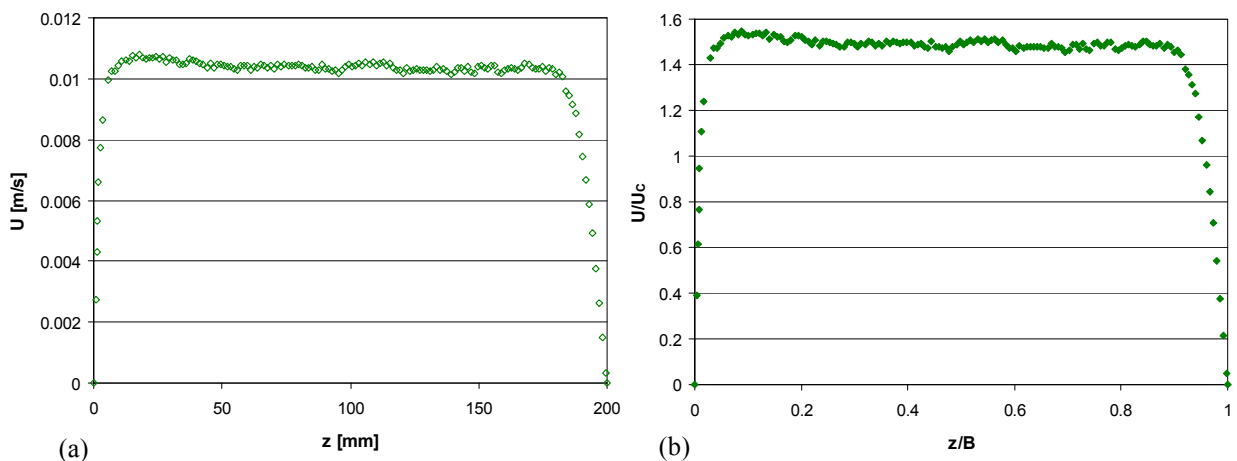


Fig.3.5 Velocity profile of a channel flow without a SJ: (a) $U(z)$, (b) $U/U_C(z/B)$; results obtained at IT CAS (Prague)

constant apparent electric power of 0.8W (at the true rms AC voltage and a current of 19.5 V and 40 mA, respectively).

For a single SJ/SJ array comparison, it is important to maintain PCT(s) at the same voltage.

3.2.1 FREQUENCY CHARACTERISTIC (using HWA)

Finding a suitable SJ actuator nominal frequency was the first step in the experiments. The maximal time-mean velocity of the flow was achieved via the nominal frequency. For this reason, HWA was used. Figure 3.6 shows the frequency characteristic in the form of the relationship between the HWA time-mean voltage and the frequency. The frequency was selected from a range between 10Hz – 60Hz, and the HWA probe was positioned at the actuator orifice axis at a distance of $y/D = 4$ from the orifice. Figure 3.6a represents the full range of measured frequencies. From a frequency of 10Hz, the HWA voltage increased. The highest value of HWA voltage was achieved at $f = 15\text{Hz}$. From this value, the HWA voltage decreased, and from $f = 20\text{Hz}$ it exhibited a very low, nearly constant value. Obviously, the discovered maximum frequency of $f = 15\text{Hz}$ was relevant to the first resonance of the actuator. Through theoretical calculation, (see Chapter 1.4, Eq. (1.30)) the first resonance was estimated at $f = 19.7\text{Hz}$, which was in reasonable agreement with the experiment. The main reason for the difference was caused by difficulties in evaluating PCT membrane stiffness – see the experimental setup and measurement in Appendix 8.

In the end, the frequency $f = 15\text{Hz}$ was chosen as the nominal frequency of the SJ actuator.

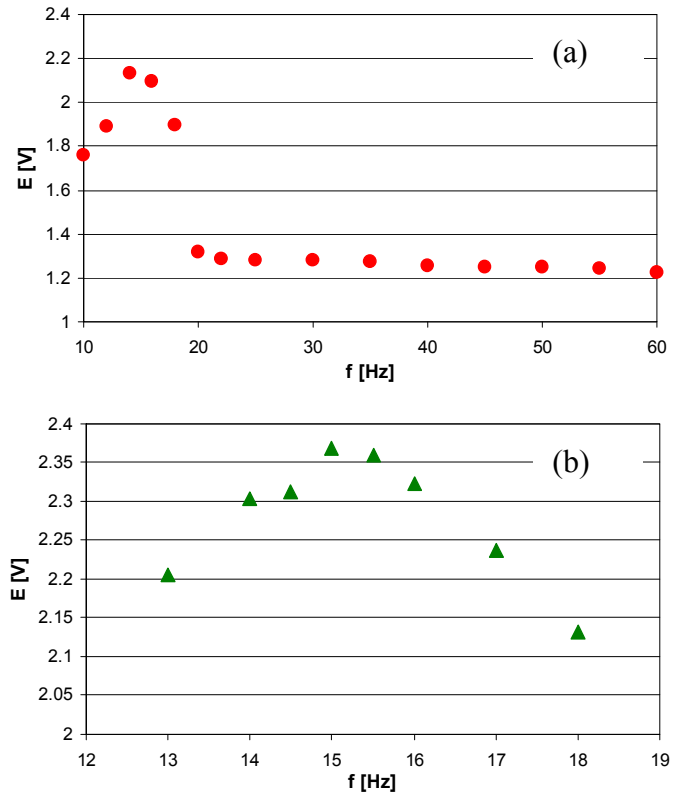


Fig.3.6 (a) Frequency characteristic of a SJ actuator, (b) detailed view (results of CTA experiments)

3.2.2 FLOW VISUALIZATION USING THE TIN ION METHOD

Tin ion visualization was used for a SJ without channel flow to observe the behavior of a single SJ. The selected frequency $f = 15\text{Hz}$ was convenient for these experiments and the SJ was clearly visible. The “white streak-lines” were recorded with a Canon EOS 40D digital camera. For lighting, a continuous ND:YV04 laser with a power output of 300 mW was used. The tin wire was fixed across the flow approx. 2mm from the orifice.

Figure 3.7 shows the vortex structures. The exposure time was 1/20 sec for Figure 3.7a and 1/60 sec for Figure 3.7b, c.

3.2.3 PCT BEHAVIOR USING LASER DOPPLER VIBROMETRY

An experiment was performed for a SJ actuator without a channel flow. The sampling rate for LDV measurement was 3000 Hz. The period starts with the leading edge of the TTL signal, which had the same frequency as the actuator driving signal. Figure 3.8 shows the results of LDV measurement of the velocity of the PCT membrane center. Figure 3.8 plots measured phase-averaged velocity magnitude U_p and membrane center displacement Δy , which was evaluated from the time behavior of the velocity, taking into consideration the sinusoidal waveform and using the least squares fitting, which yielded $\Delta y(t) = \Delta y_{\max} \sin(2\pi f t^{**})$, where t^{**} was the time from the moment when membrane displacement starts. Moreover, Figure 3.8 shows the reference TTL signal (acquired from the signal generator) and actuator sinusoidal input (the amplifier output). The TTL and sinusoidal input are not represented at scale. The positive values of the phase-averaged velocity magnitude (U_p) mean an extrusion from the orifice while negative values

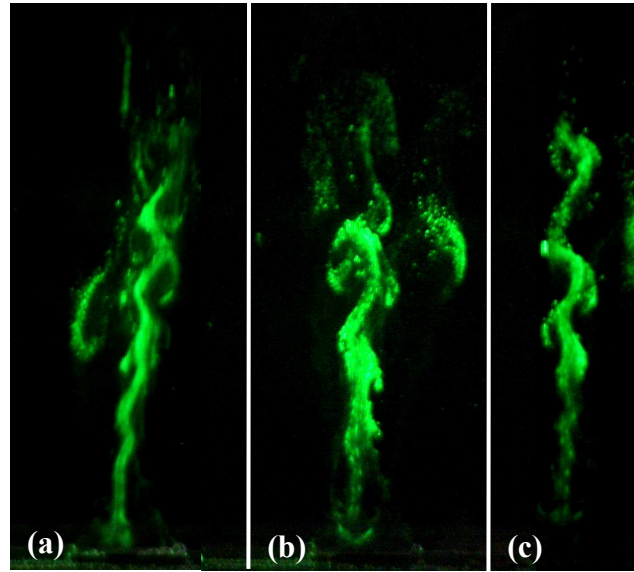


Fig.3.7 Tin ion visualization of a single SJ

Moreover, Figure 3.8 shows the reference TTL signal (acquired from the signal generator) and actuator sinusoidal input (the amplifier output). The TTL and sinusoidal input are not represented at scale. The positive values of the phase-averaged velocity magnitude (U_p) mean an extrusion from the orifice while negative values

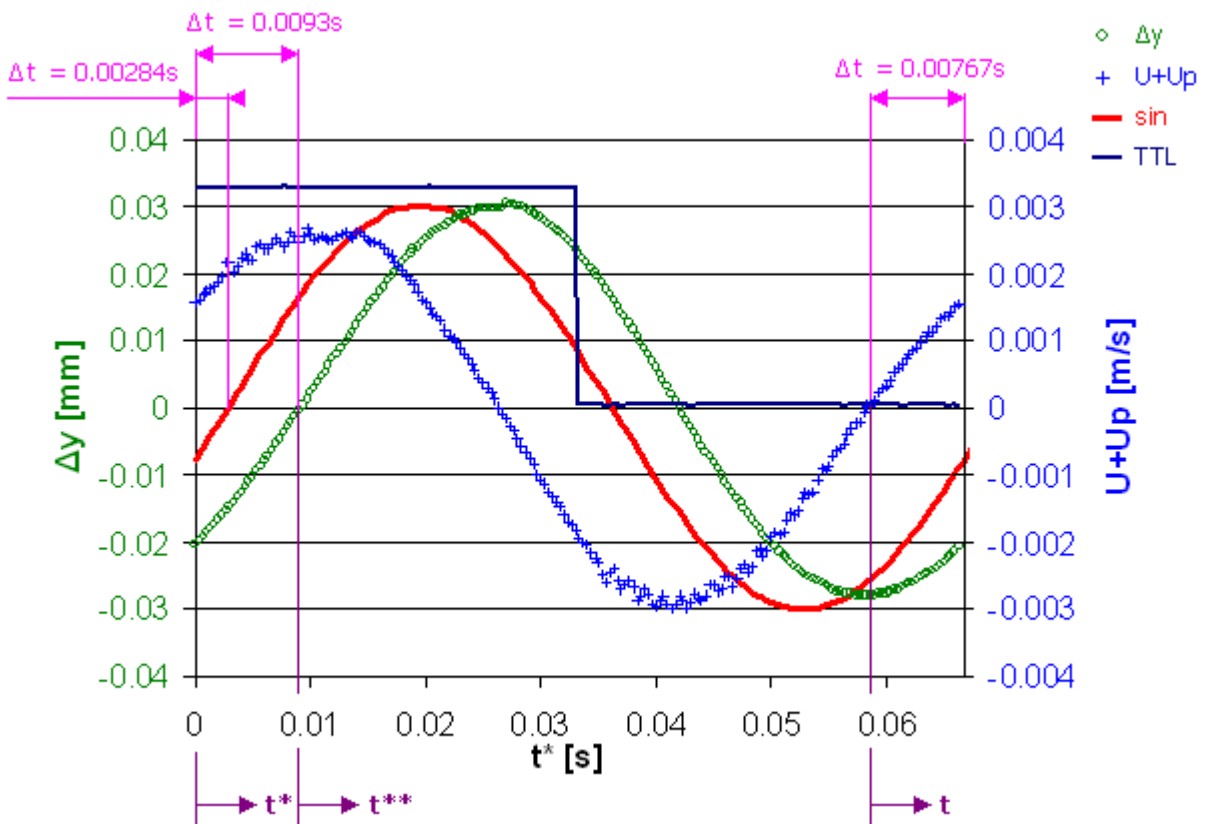


Fig.3.8 Results of LDV measurement of the oscillating membrane center. Phase shift between LDV membrane center velocity measurement and its position calculation, TTL, and driving sinusoidal signal

mean suction into the actuator orifice. The highest velocity of extrusion was at zero displacement of the membrane. The delay between the TTL and the actuator sinusoidal input was caused by the amplifier and electrical circuit loading; it was 2.84ms.

Figures 3.9a, b show the measured membrane center velocity and evaluated membrane center displacement in time in comparison with the theoretical harmonic velocity and displacement in time, respectively.

Theoretical harmonic membrane center velocity and displacement (pink curves) was described as $v(t) = v_{\max} \cos(2\pi f t^{**})$ and $\Delta y(t) = \Delta y_{\max} \sin(2\pi f t^{**})$. The least squares fitting gave $\Delta y_{\max} = 0.0274\text{mm}$ – see Figure 3.9b. The relevant maximum membrane velocity was $v_{\max} = 2\pi f \Delta y_{\max} = 0.00258\text{m/s}$. Taking continuity into consideration, the plug flow model of an extruded fluid column and the parabolic shape of the membrane deflection, the maximum velocity in the actuator orifice can be evaluated as $U_{\max} = 0.5(D_D/D)^2 v_{\max} = 0.186\text{m/s}$. Finally, the sinusoidal character gave $U_0 = U_{\max}/\pi = 0.059\text{m/s}$ and $Re_{SJ} = 177$.

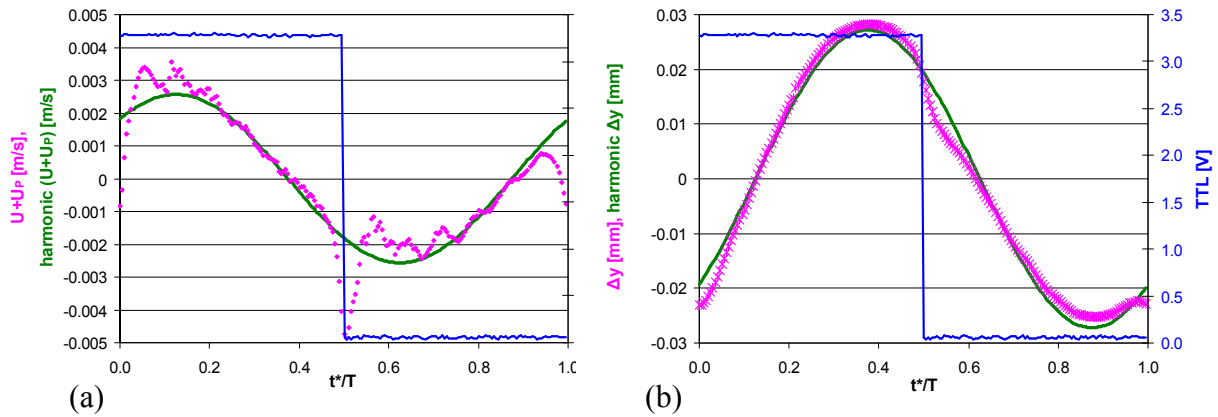


Fig.3.9 Oscillating membrane center: (a) LDV measured velocity, (b) calculated displacement

3.2.4 HWA VELOCITY MEASUREMENT

HWA experiments can evaluate flow velocity at a specific distance from an actuator orifice. The results helped to set up a velocity range in the post-processing of PIV measurements (range validation in DynamicStudio v.2.30, DANTEC). A 55P36 hot-film probe was used. Note that the film probe in the configuration used does not enable the absolute value of suction flow velocity to be measured. Measured velocity values of suction flow (in y direction) were influenced by probe construction and the massive holder. However, this effect was significant only at the vicinity of the actuator orifice). Further downstream from the orifice, the liquid was already flowing in the direction of $+y$, therefore the inaccuracy of the velocity measurement at the time of suction is not shown.

Figure 3.10a demonstrates the dependence of the phase-averaged velocity U_p in a different instant of the period and the time-mean velocity U on the distance from the actuator orifice. There was a visible decrease in velocity as the distance increased along y direction. At a distance of $y/D = 3.7$, the flow oscillation practically disappeared, and the flow can be considered as a steady jet flow. Further downstream from the orifice, the vortex structure disappeared owing to dissipative processes, thereby decreasing the velocity. The dependence of the time-mean velocity on the y in the logarithmic scale (in dimensionless form in Figure 3.10b) shows the slope of the line relating to two regions of the SJ. The exponents of velocity decay $U \sim y^n$ were $n = -0.445$ and $n = -1.04$, respectively.

Similar behavior was found also in [45 and 86], where $n = -0.43$ and $n = -1.04$. In [85], the authors established $n = -1.04$. In [42], three jets were compared: a SJ, a continual (steady) jet, and a mixed pulsed jet with an additional blowing component. Only the exponents for the continual jet ($n = -0.95$) and the mixed jet ($n = -1.20$) were shown. The exponent for the SJ is not mentioned, but from the experimental results, it can be approximated as $n = -1.04$.

In all these cases, the exponents are the same or very similar. This indicates that they are not an influence of SJ actuator design or the working fluid. Exponent $n = -1.04$ confirms that a SJ in the distant field has the character of a continual fluid jet. It is a well known fact that the stream-wise velocity decay of conventional (steady) axisymmetric fully-developed turbulent jets is $U/U_0 \sim y/D^{-1.0}$ – see Schlichting and Gersten, [89].

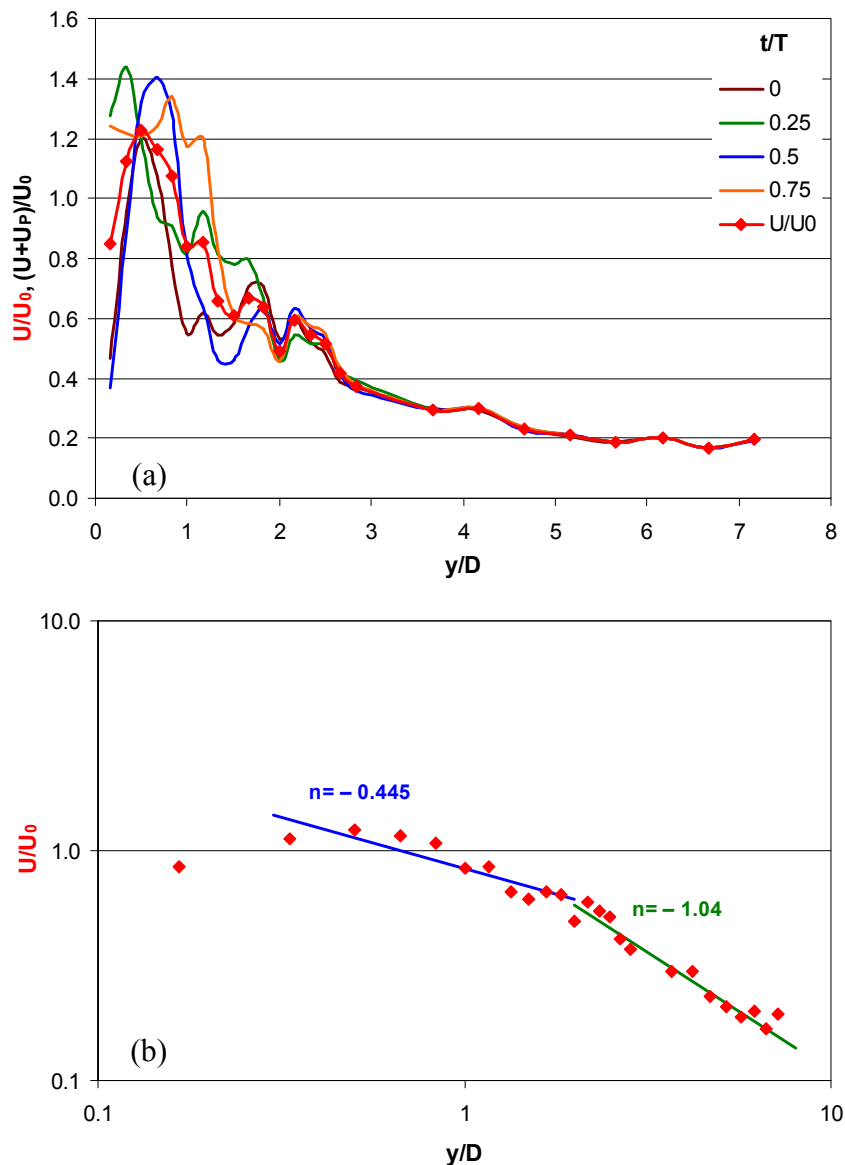


Fig.3.10 Results of CTA experiments:

- (a) Dependence of the phase-averaged velocity magnitude at different instances in the period and of the time-mean velocity on the distance from the actuator orifice,
- (b) Dependence of the time-mean velocity on the distance from the orifice on a logarithmic scale

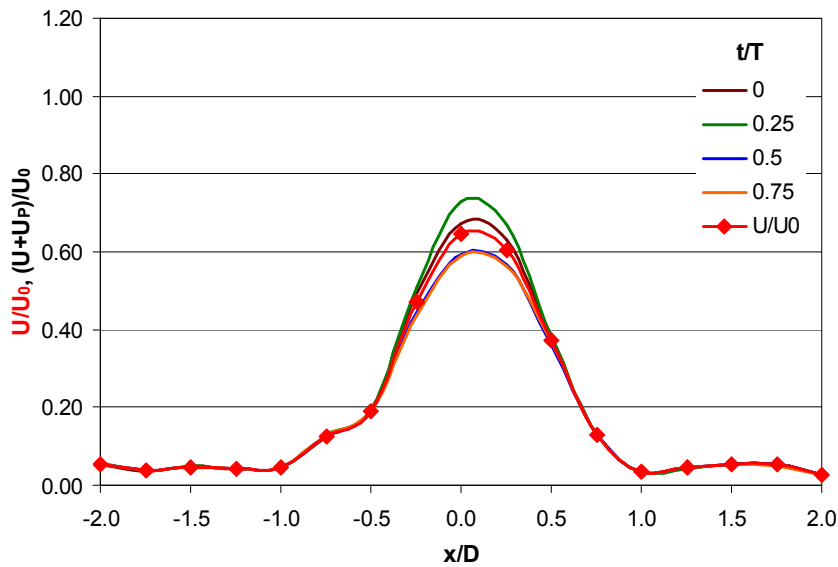


Fig.3.11 Phase-averaged velocity magnitude profiles and time-mean velocity magnitude profile at distance $y/D = 1.5$ (results of CTA experiments)

Figure 3.11 shows the phase-averaged velocity magnitude profiles, which were measured at $y/D = 1.5$. The oscillating character of the velocity is easily distinguishable there.

3.2.5 PIV EXPERIMENTS OF A SINGLE SJ IN QUIESCENT FLUID

The experiments were performed using the PIV system of TUL. The delay time between two laser pulses (two images) was $t = 5\text{ms}$. For a comparison with HWA results, the dimensionless coordinates in Figures 3.13 are outspread to the orifice diameter D .

Figure 3.12a shows the results of a single SJ at different instant of the period in the form of vectors of the phase-averaged velocity (actuator, see Figure 2.1). For comparison, Figure 3.12b shows the contours of the phase-averaged velocity magnitude. Figures 3.12a, b plotted at $t/T = 0, 0.25, 0.5,$ and 0.75 show a SJ at the beginning of the extrusion from the actuator, maximum extrusion velocity, beginning of suction, and maximum suction velocity, respectively. Figure 3.12b clearly shows the formation of vortices and their propagation downstream in y direction.

Figure 3.13a shows the phase-averaged velocity magnitude profiles during the actuation cycle for the distance of $y/D = 1.5$ without channel flow influence. There was evidence that the highest velocity was in phase with the maximum extrusion velocity from the orifice at the instant $t/T = 0.25$. At a distance of $y/D = 11.5$ (Figure 3.13b), the periodical “jet synthesis” process seemed to be practically completed, and the jet appeared nearly non-periodic.

3.2.6 PIV EXPERIMENTS OF A SINGLE SJ IN A CHANNEL FLOW

These experiments were performed at TU/e (Netherlands). The delay time between the two laser pulses was $t = 5\text{ms}$. The interaction of the channel flow with the SJ at the instant of maximum extrusion velocity ($t/T = 0.25$) is shown in Figure 3.14 in the form of phase-averaged velocity magnitude contours and phase-averaged velocity magnitude contours in a discrete drawing style. This experiment clearly demonstrated SJ bending and its propagation downstream of the main channel flow. The SJ deflection can be evaluated approximately as

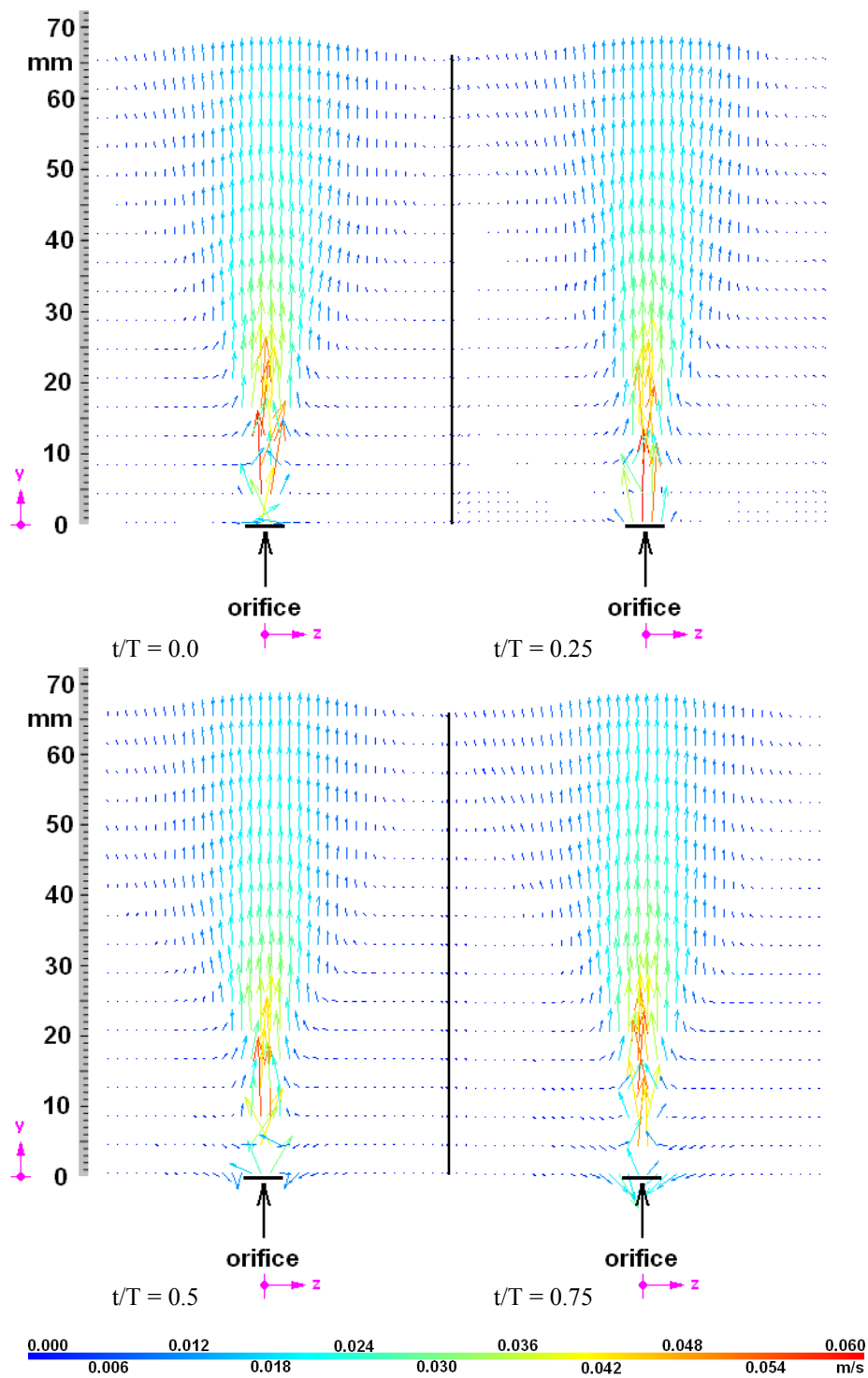


Fig.3.12a Single SJ – vectors of the phase-averaged velocity magnitude (results of PIV experiments)

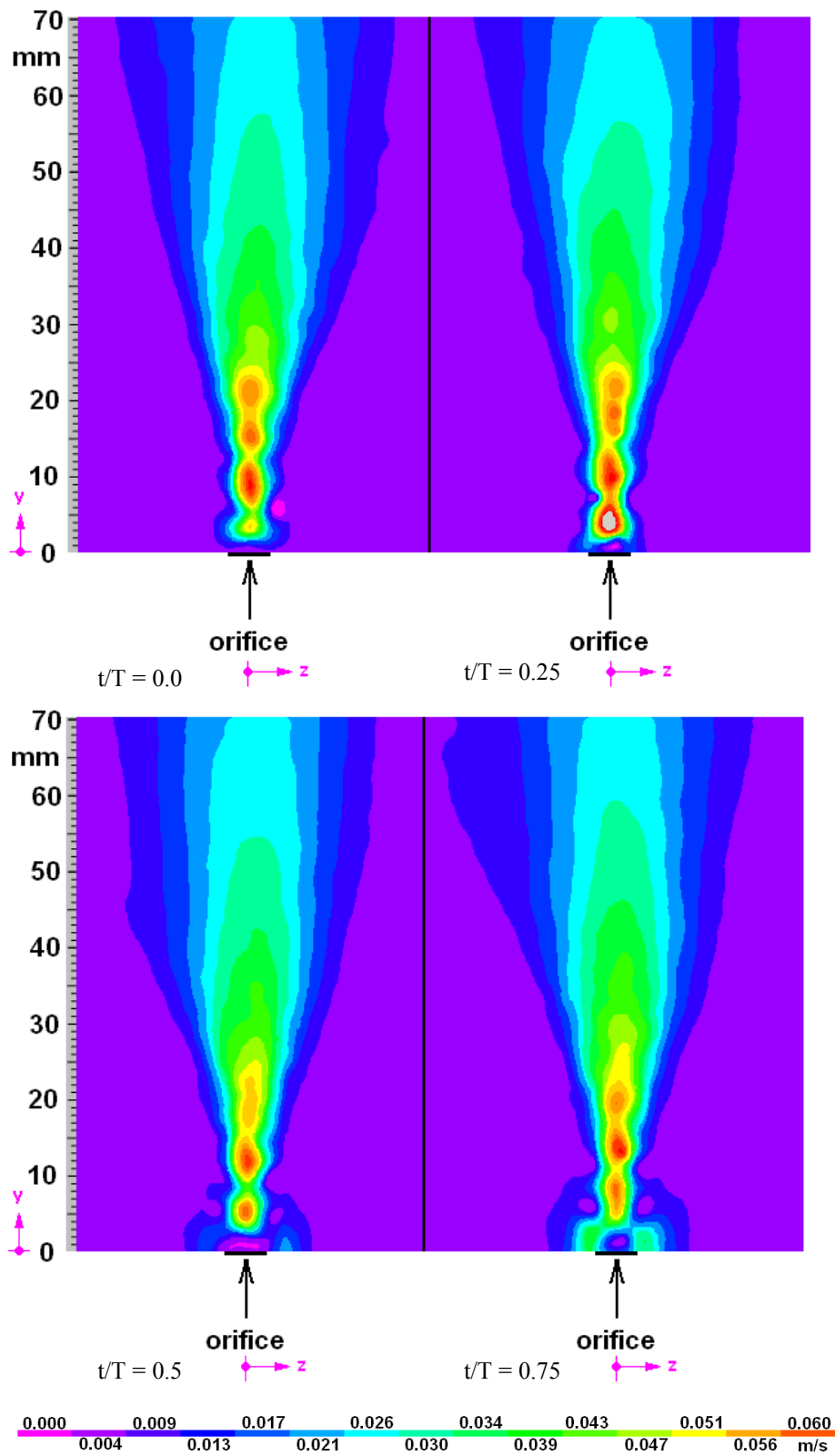


Fig.3.12b Single SJ – contours of the phase-averaged velocity magnitude (results of PIV experiments)

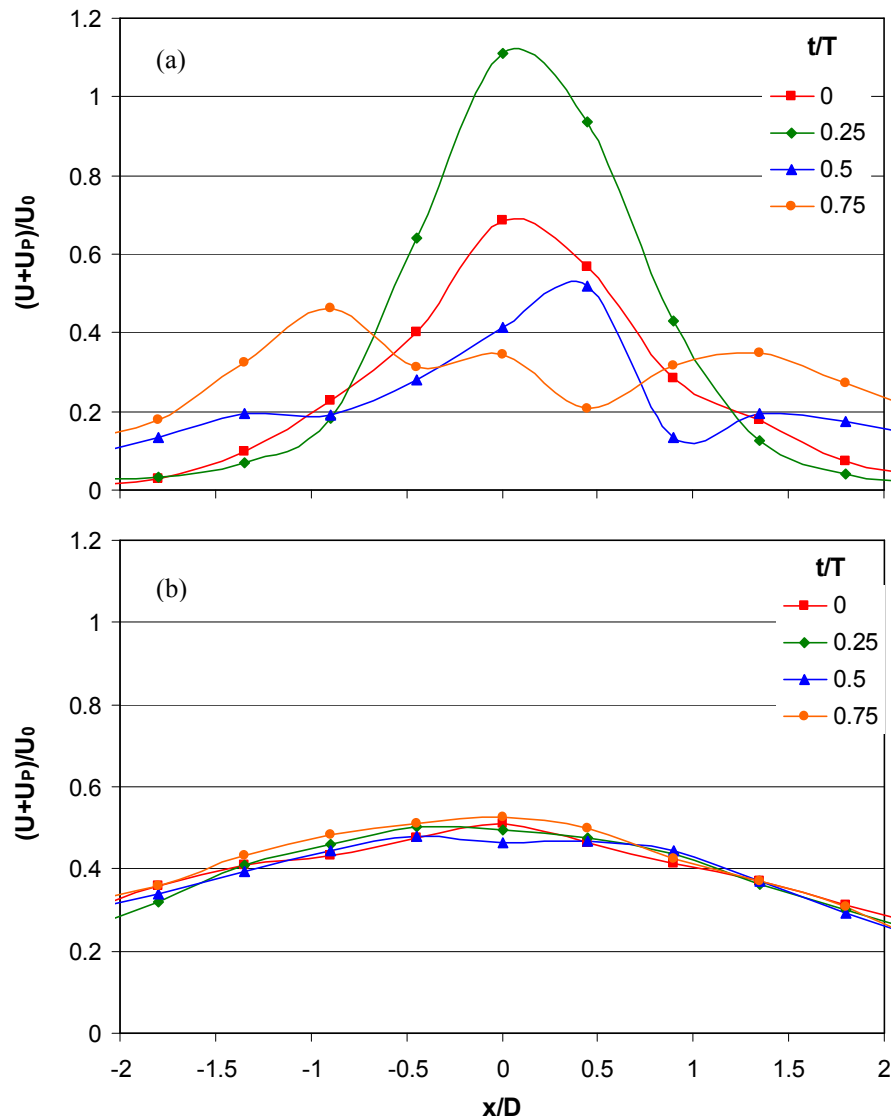


Fig.3.13 Phase-averaged velocity magnitude profiles of a single SJ during the actuation cycle at: (a) $y/D = 1.5$, (b) $y/D = 11.5$ (results of PIV experiments)

$\phi = 22^\circ$ in the middle of the channel, as is shown in Fig. 3.14. Further downstream, at $y = 24$ mm, the deflection angle reaches a value of 55° . Moreover, the SJ reached the opposite wall ($y = 40$ mm), where an oblique jet impingement was identified (at $x = 30 - 40$ mm, see the ellipse mark in Figure 3.14). Obviously, heat/mass transfer enhancement can be expected in the impingement area – this effect is desirable in various applications. Nevertheless, even more important than this local effect could be the overall modification on the channel flow further downstream from the impingement area. Note that the experimental results are plotted in Figure 3.14a, while Figure 3.14b shows a post processing smoothing of the results.

Figures 3.15a, b, and c show the phase-averaged velocity magnitude profiles at different distances x from the orifice of the SJ actuator in dimensionless form.

Figure 3.15a shows that the velocity profiles were significantly influenced at the top of the channel – i.e. near the wall opposite the SJ actuator, where the SJ impingement effect occurs and where the velocity $U+U_p$ reached nearly 0.02m/s, i.e. $(U+U_p)/U_C$ was nearly 3.34. Obviously, this was caused by the relatively high velocity of the SJ – the velocity U_0 was one order higher than U_C , as evaluated below.

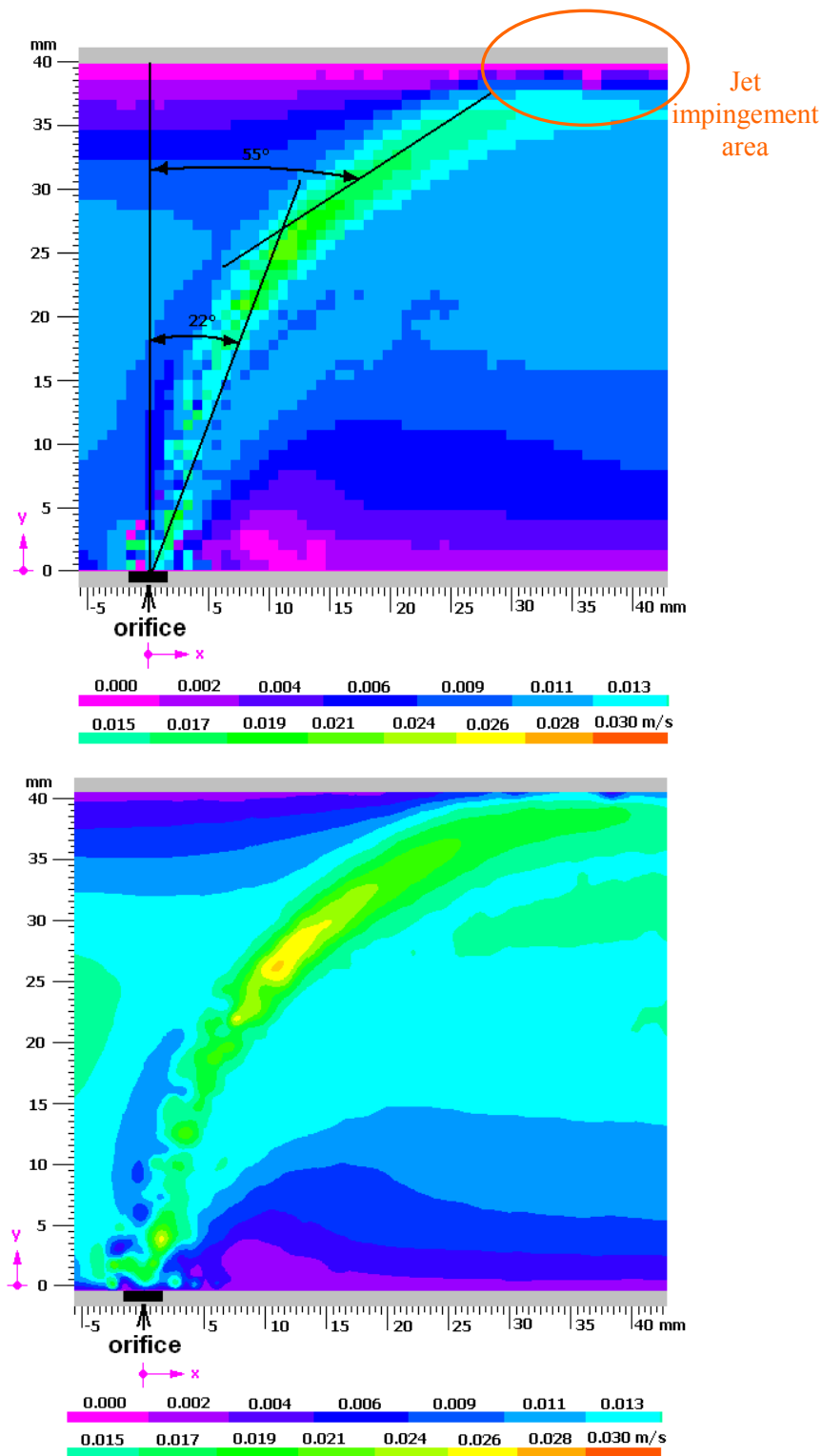


Fig 3.14 Velocity magnitude contours of the channel flow interacting with a single SJ. Phase-averaged for $t/T = 0.25$, PIV experiments: (a) discrete drawing style, (b) post processing smoothing

Further downstream, the flow development was propagated downwards to the bottom channel wall (see Figures 3.15b, c). The flow profile again redistributed towards a parabolic profile, however at $x = 115$ mm this profile had not yet been achieved.

The time-mean velocity through the channel and the synthetic jet time-mean orifice velocity were evaluated as approximately $U_C = 0.006$ m/s and $U_0 = 0.059$ m/s. The associated maximum Reynolds numbers were $Re_C = 480$ and $Re_{SJ} = 177$, respectively.

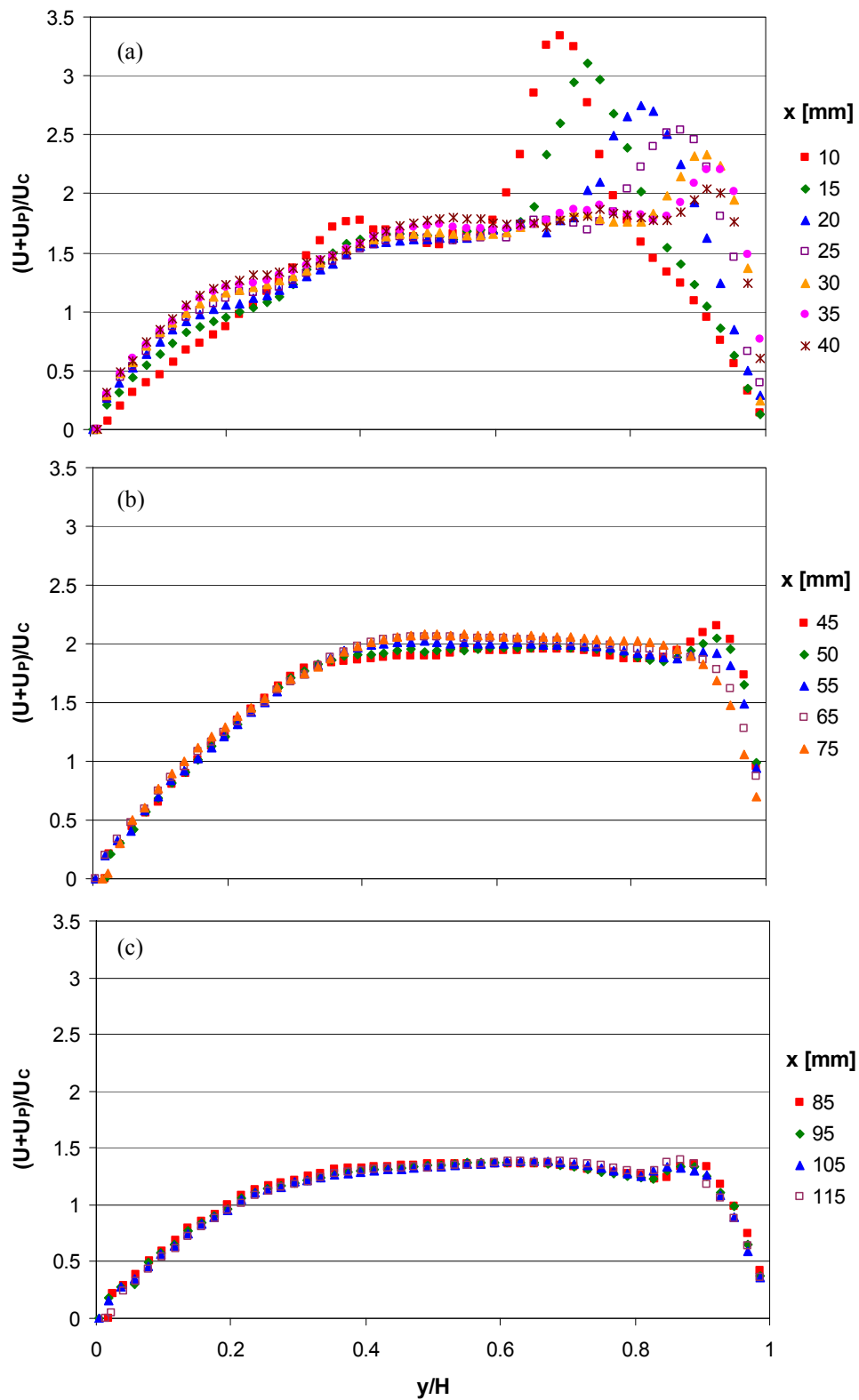


Fig.3.15 Phase-averaged velocity magnitude profiles of channel flow interaction with a single SJ, $t/T = 0.25$
 (a) $x = (10-40)$ mm, (b) $x = (45-75)$ mm, (c) $x = (85-115)$ mm
 (results of PIV experiments)

Experimental results

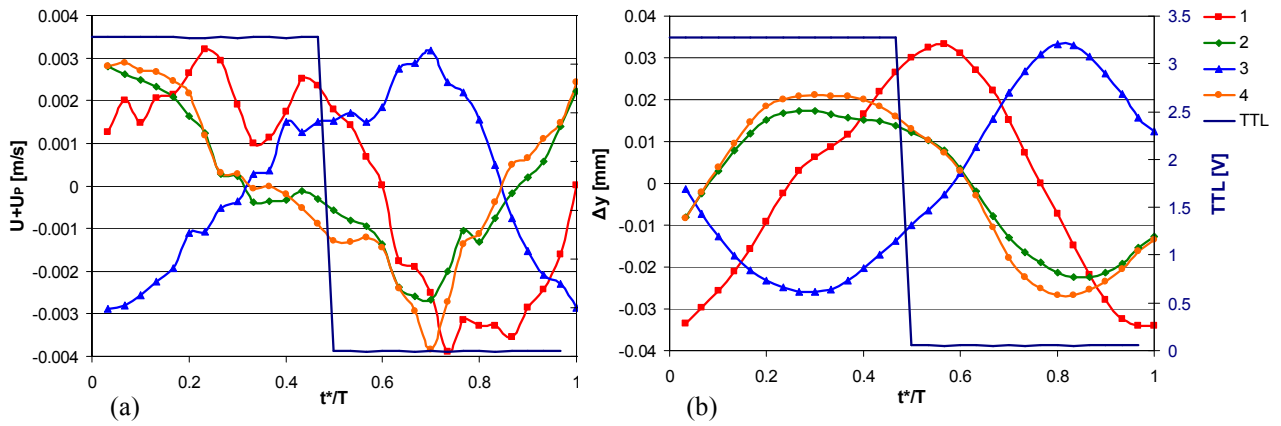


Fig.3.16 Unselected PCT - oscillating membrane center in time (a) measured velocity, (b) calculated displacement (results of LDV experiments)

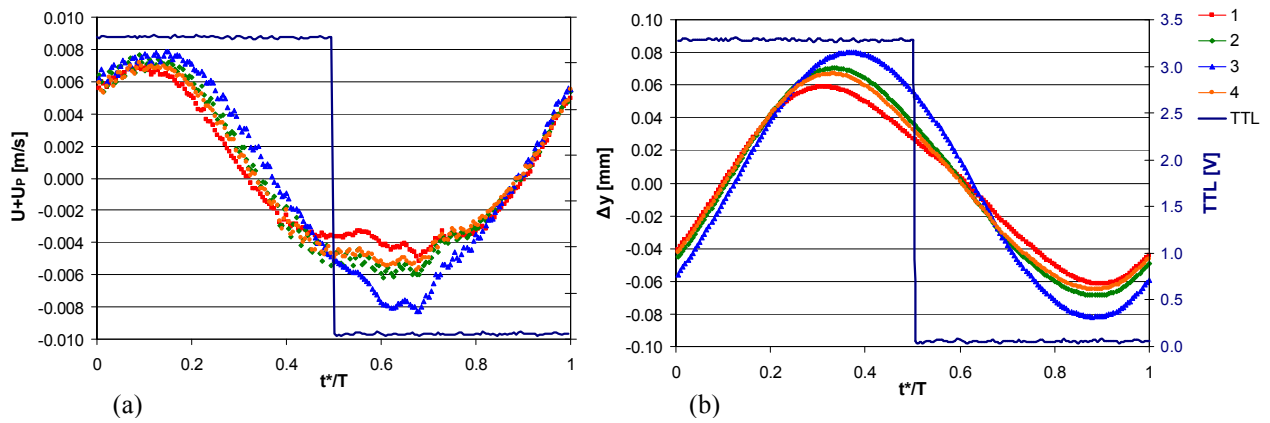


Fig.3.17 Selected PCT, different power - oscillating membrane center in time (a) measured velocity, (b) calculated displacement (results of LDV experiments)

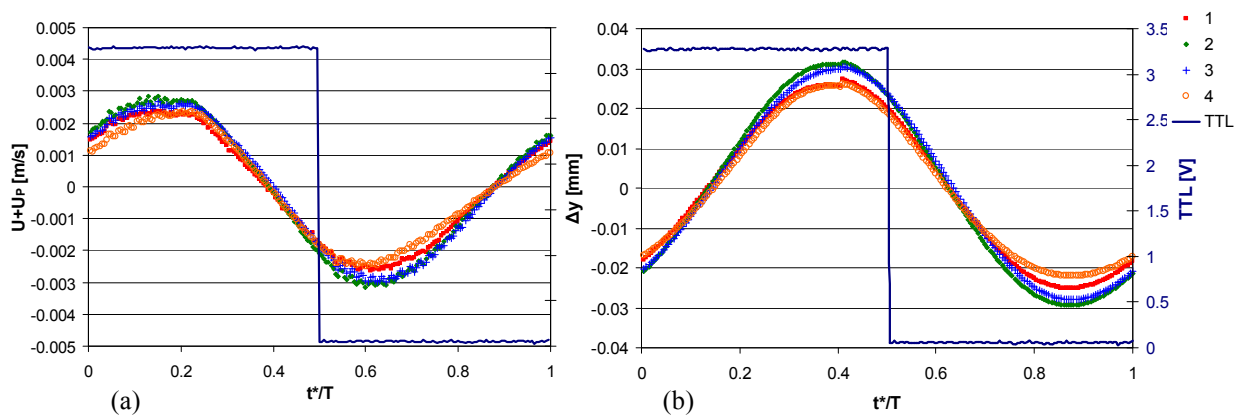


Fig.3.18 Selected PCT, similar power - oscillating membrane center in time (a) measured velocity, (b) calculated displacement (results of LDV experiments)

Note that the different order of magnitude of the velocities U_0 and U_C and the limits of the dynamic resolution of the PIV method resulted in the basic impossibility to measure a higher velocity at the SJ actuator orifice and slow velocity of a channel flow *simultaneously*. In other words, it was impossible to set up a time delay, which would be appropriate for both orders of the velocity magnitude – thus many ‘lost-pairs’ (non-correlated interrogation areas) occurred in the higher velocity area of the SJ. Therefore, the above-mentioned measurement of the velocity profiles started from $x = 10$ mm, as shown in Fig. 3.15a.

3.3 SYNTHETIC JET ARRAY

The SJ array consisted of four SJ actuators located side by side across a channel. They were electrically connected in parallel. The actuating membranes were made out of PCT. It was very important to use PCTs with identical or very similar characteristics. In spite of PCT producer guarantees of identical electrical properties, it is very important to take care during the phase shift of the particular PCTs used.

For a proper comparison of a SJ array with single SJ, the PCTs have to be fed with a sinusoidal AC signal with the same voltage as for a single SJ. In the case where PCTs are connected in parallel, the electrical current automatically set. The set values for the experiments were the following: a true rms AC voltage of 19.5 V, a true rms AC current of approx. 0.164 A, and an apparent electric power of 0.8W for each actuator (3.2W for the entire SJ array). The actuators working frequency was 15Hz.

3.3.1 SYNCHRONIZATION OF THE PIEZOCERAMIC SYSTEM (using LDV)

3.3.1.1 UNSELECTED PIEZOCERAMIC TRANSDUCERS

The first group of randomly chosen PCTs only had the same impedance. In spite of their identical electrical properties, later experiments proved the phase shift between these PCTs.

Figures 3.16a, b show results from the LDV measurement. The sampling rate for this measurement was 450Hz. The period starts with leading edge of the TTL signal. Curves 1, 2, 3, and 4 are the velocity (Figure 3.16a) or displacement (Figure 3.16b) of the actuator membrane center in time. The blue curve is the TTL signal. There is visible phase shift between PTCs. These phase shifts, especially PCTs number 1 and 3, when compared with PCTs number 2 and 4, are unsuitable for the proper actuation of a SJ array. Therefore, new PTCs without phase shift had to be found. See experiments in Appendix 9.

3.3.1.2 SELECTED PIEZOCERAMIC TRANSDUCERS – DIFFERENT POWER OF SJ ACTUATORS

After discovering that the previous PCTs were not in phase, a second group of PCTs was tested. The sampling rate for LDV measurement was 3000Hz. Figures 3.17a, b show nearly the same phase shift among PCTs. Moreover, curves numbers 1, 2, and 4 have very close values of membrane center maximum velocity and, consequently, membrane center maximum displacement. PCT number 3 has the highest values – approx. 20% higher than the other three. The experiments described in Appendix 10 show a higher power in SJ actuator

number 3, which influenced its surroundings more than the other three actuators. Therefore, this actuator was replaced by one with the same power characteristics as all SJ actuators.

3.3.1.3 SELECTED PIEZOCERAMIC TRANSDUCERS – SIMILAR POWER OF SJ ACTUATORS

Subsequently, the above described selection process had to be repeated. Figures 3.18a, b show LDV measurement of the final four PCTs (sampling rate of 3000Hz). They demonstrated the same phase shift and a very similar velocity and displacement of the membrane center. The results confirmed that these PCTs were the proper ones for conducting the next experiments.

From the membrane center velocity, and considering continuity, the plug flow model of an extruded fluid column, the parabolic shape of the membrane deflection, the sinusoidal waveforms, the time-mean orifice velocity, and the Reynolds number of a particular SJ actuator were evaluated (as described in paragraph 3.2.3 above). The results were: $U_{0_1} = 0.057\text{m/s}$, $U_{0_2} = 0.066\text{m/s}$, $U_{0_3} = 0.063\text{m/s}$, $U_{0_4} = 0.053\text{m/s}$ and $Re_{SJ_1} = 170$, $Re_{SJ_2} = 199$, $Re_{SJ_3} = 190$, $Re_{SJ_4} = 158$.

3.3.2 FLOW VISUALIZATION OF A SJ ARRAY USING THE TIN ION METHOD

For technical reasons, the visualization of a SJ array using the tin ion method was made in quiescent fluid, without the channel flow and even without the upper wall of the channel. The upper wall represents a water free surface at $H = 40\text{mm}$. Figure 3.19 shows the influence of the individual jets and the vortex structures. The first three vortex rings behind the SJ actuator orifice are visible, as is indicated by arrows (demonstrated by SJ 2): The first one is near the actuator orifice, the second one drifts away from the orifice, and the third one is still clearly visible – obviously, the cascade process dissipates a bit further downstream. This experiment quite easily confirmed the evaluation of the SJ “stroke length” from the above-described U_0 velocity evaluation (based on the LDV measurements) and Eq. (1.14); L_0 is marked at SJ 1 in Figure 3.19. Evaluation from the visualization gives approx. $L_{0_1} = 3.64\text{ mm}$, $L_{0_2} = 4.36\text{ mm}$, $L_{0_3} = 4.07\text{ mm}$, and $L_{0_4} = 3.06\text{ mm}$. It is worth noting that very similar values resulted from Eq. (1.14), i.e. from the LDV measurements: $L_{0_1} = 3.8\text{ mm}$, $L_{0_2} = 4.4\text{ mm}$, $L_{0_3} = 4.2\text{ mm}$, and $L_{0_4} = 3.54\text{ mm}$.

Instantaneous pictures were recorded using a NIKON D300 camera, with an exposure time of 1.3 sec. For lighting, the laser for the PIV system New Wave Gemini, with output energy of 120 mJ per pulse, was used. The frequency of the SJ actuators and the laser system was set at 15Hz and 3Hz, respectively. The tin wire was fixed 10mm to the side of the

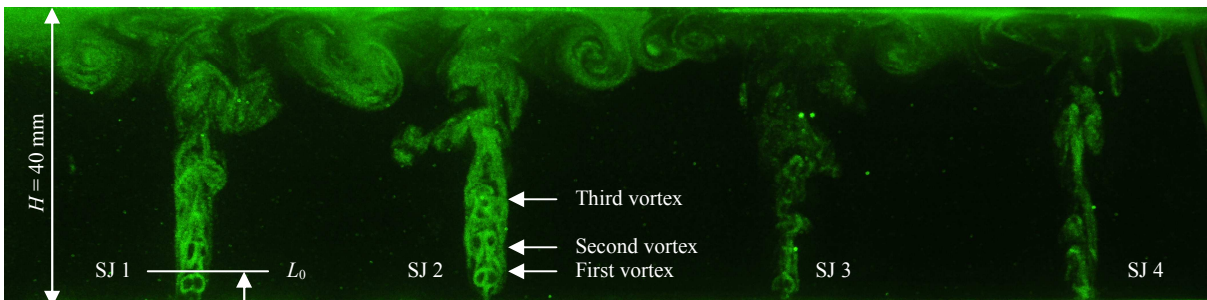


Fig.3.19 Tin ion visualization of a SJ array in quiescent water on plane III (see drawing in Appendix 2), without channel flow

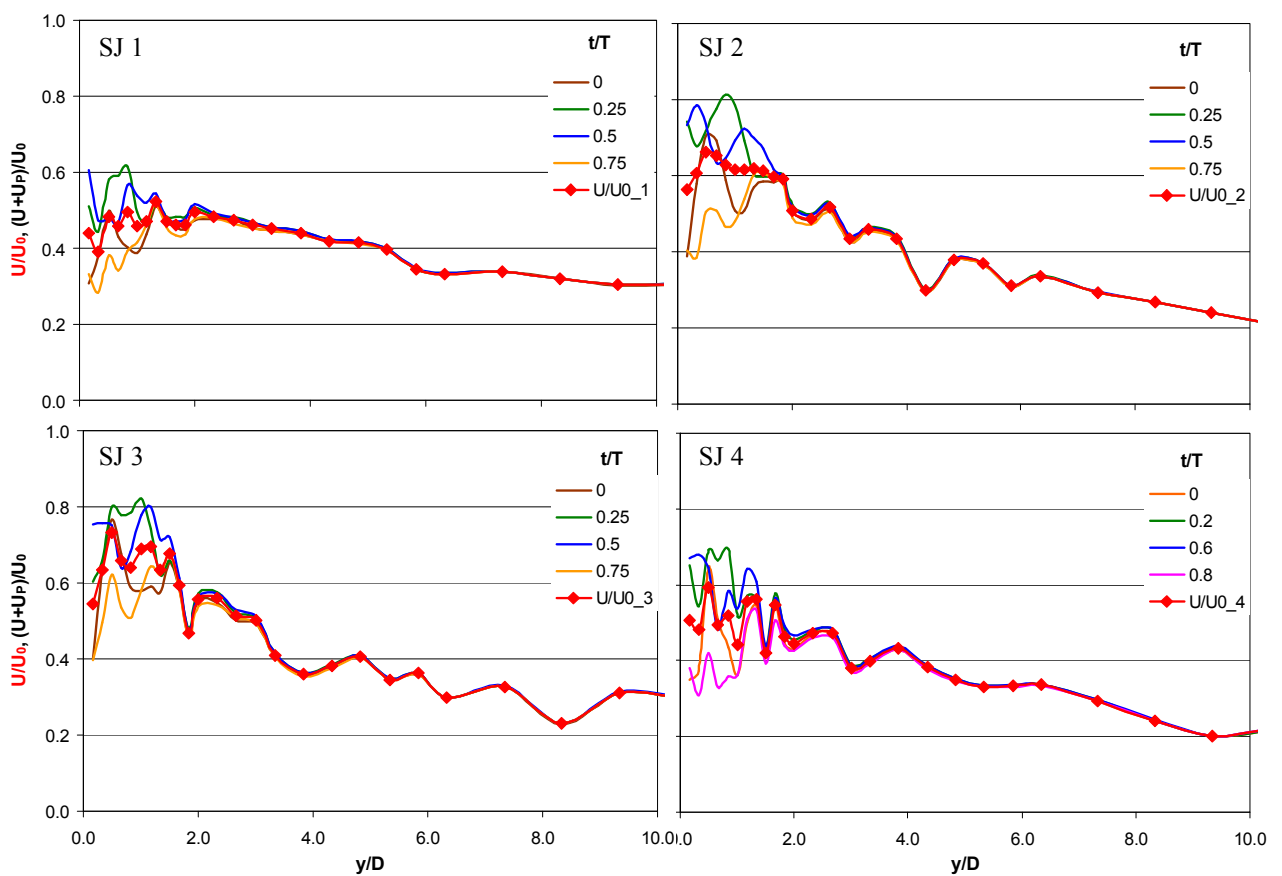


Fig.3.20 Dependence of the phase-averaged velocity magnitude at different instances in the period and of the time-mean velocity magnitude on the distance from the SJ array actuator orifices (results of CTA experiments)

orifices' axes. Electrolysis was running for only few seconds to make a tin ion “fog” but not long enough darken the water.

3.3.3 SJ ARRAY VELOCITY MEASUREMENT USING HWA

As in the previous case of a single SJ, a 55P36 hot-film probe was used. Velocity profiles at two distances from the orifice and the dependence of average velocity on distance from the orifice were measured. The results are presented in Fig. 3.20 in non-dimensional coordinates, and velocities are related to the corresponding U_0 .

Figure 3.20 demonstrates the dependence of average velocity at different times and time-mean velocities along the distance from the orifice of each actuator. As distance increases, velocity (in principle) decreases. From the time-mean velocities, it was visible that the oscillations of the flow decrease from distance $y/D = 6.3$.

Figure 3.21 shows the dependence of time-mean velocity on the orifice direction on a logarithmic scale, and it shows the slope of the line of each SJ. Note, that the bottom and top channel walls are located outside of the plotted area, namely at $y/D = 0$ and 13.33, respectively. It is a known fact that a non-influenced single SJ in a distant field has a line slope of $n = -1.04$, which corresponds with the continual fluid jet (see Figure 3.10b) – e.g. Schlichting and Gersten, [89]. In a SJ array, SJs are under the influence of mutual interactions, and the slope of the line has the exponent $n = (-0.37 - -0.57)$. A comparison with Fig. 3.10 clearly demonstrates that the SJs in the array could not reach a developed stage with an exponent of $n \sim -1$.

Experimental results

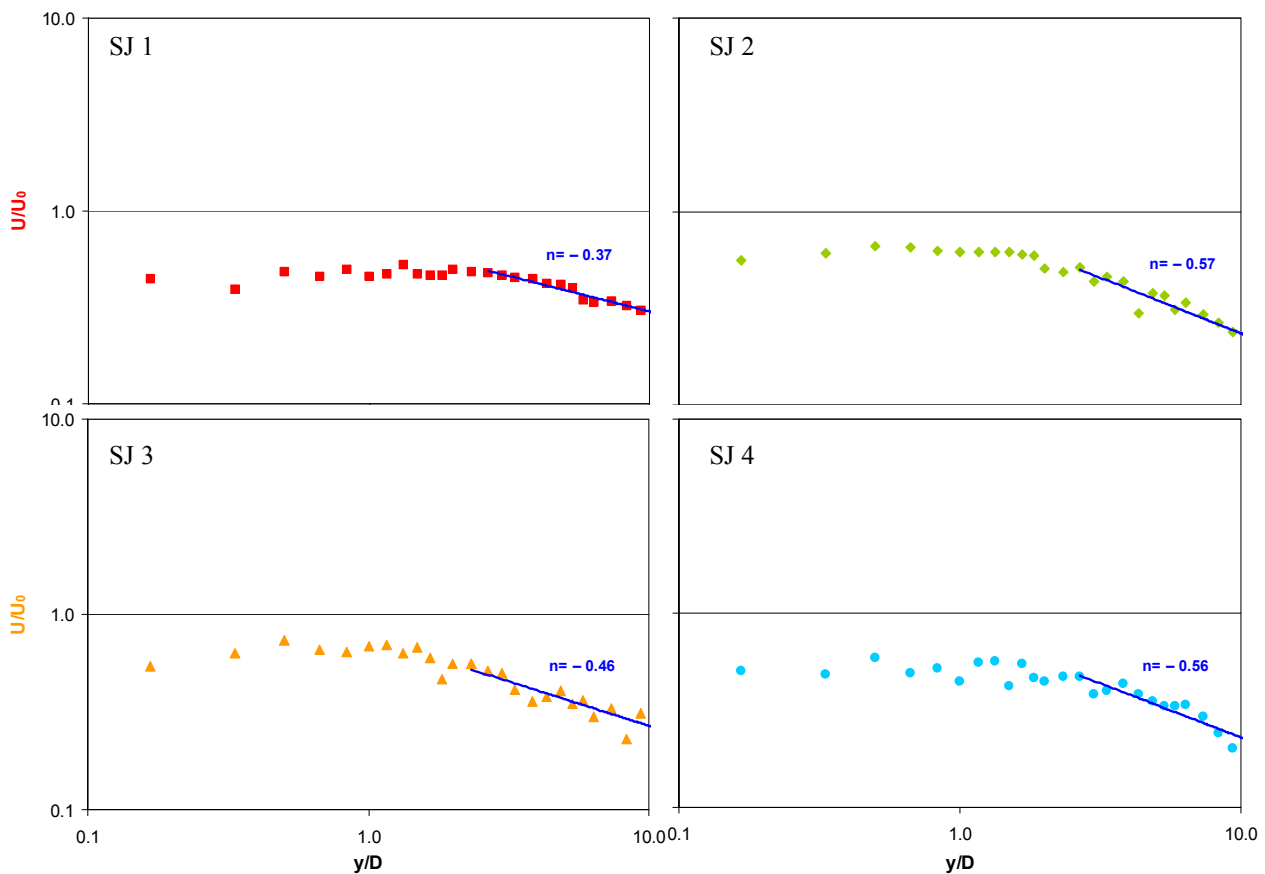


Fig.3.21 Dependence of the time-mean velocity magnitude on the distance from the SJ actuator orifices on a logarithmic scale (CTA experiments); the bottom and top channel walls are located outside of the plotted area, namely at $y/D = 0$ and 13.33, respectively

Figures 3.22 and 3.23 show phase-averaged velocity magnitude profiles at distances $y/D = 0.5$ and $y/D = 1.5$. The time-mean velocity magnitude profile is plotted as well. Despite some individual differences between SJs 1 – 4, Figs. 3.22 and 3.23 demonstrate that they operate sufficiently in phase.

3.3.4 PIV EXPERIMENTS OF A SJ ARRAY IN QUIESCENT FLUID

The experiments were performed with the TUL PIV system. The delay time between the two laser pulses was $t = 5\text{ms}$. Due to the large size of the SJ array equipment, the images were scanned on two cameras. Only one camera did not record all four actuators in high-quality resolution. During post processing, these two pictures were composed into one and consequently processed. The Matlab program was used for composing (see Appendix 11).

The SJ array experiments were performed with the upper wall of the device attached (Figure 2.6). Figures 3.24a, b demonstrate the results of the SJ array at different instances in the period in the form of phase-averaged velocity magnitude contours together with vectors, which show flow direction. The monitored plane was aligned to the collective centerline of all orifices. Figures 3.24 plotted at $t/T = 0, 0.25, 0.5,$ and 0.75 revealed the influence of individual SJs – a collision of the vortexes is seen in the upper third of figures.

Figure 3.25 represents the SJ array's phase-averaged velocity magnitude profiles during the actuation cycle $y/D = 1.5$. In comparison with the relevant results from CTA (Figure 3.23), it exhibited similar values and developments in velocities profiles.

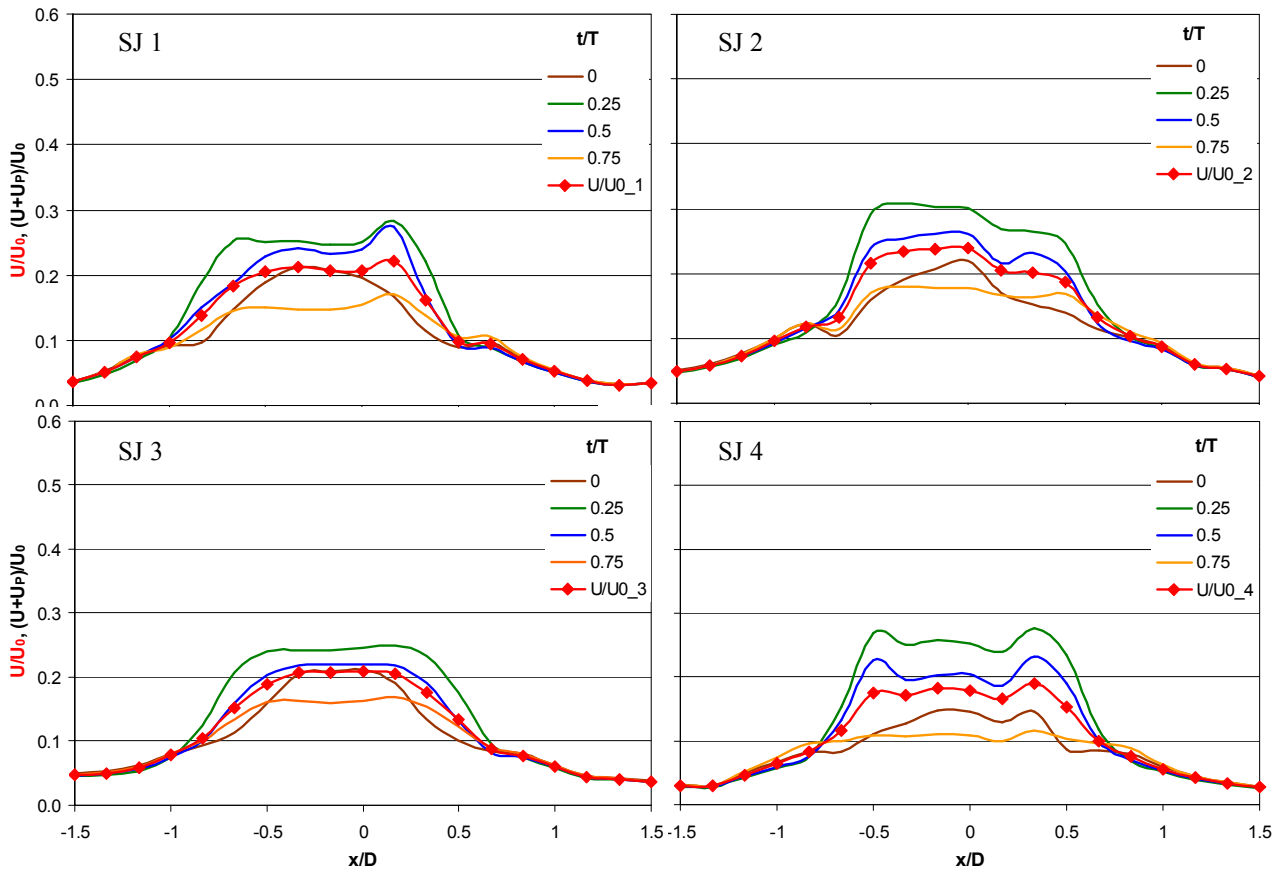


Fig.3.22 Phase-averaged velocity magnitude profiles and time-mean velocity magnitude profile at distance $y/D = 0.5$ (results of CTA experiments)

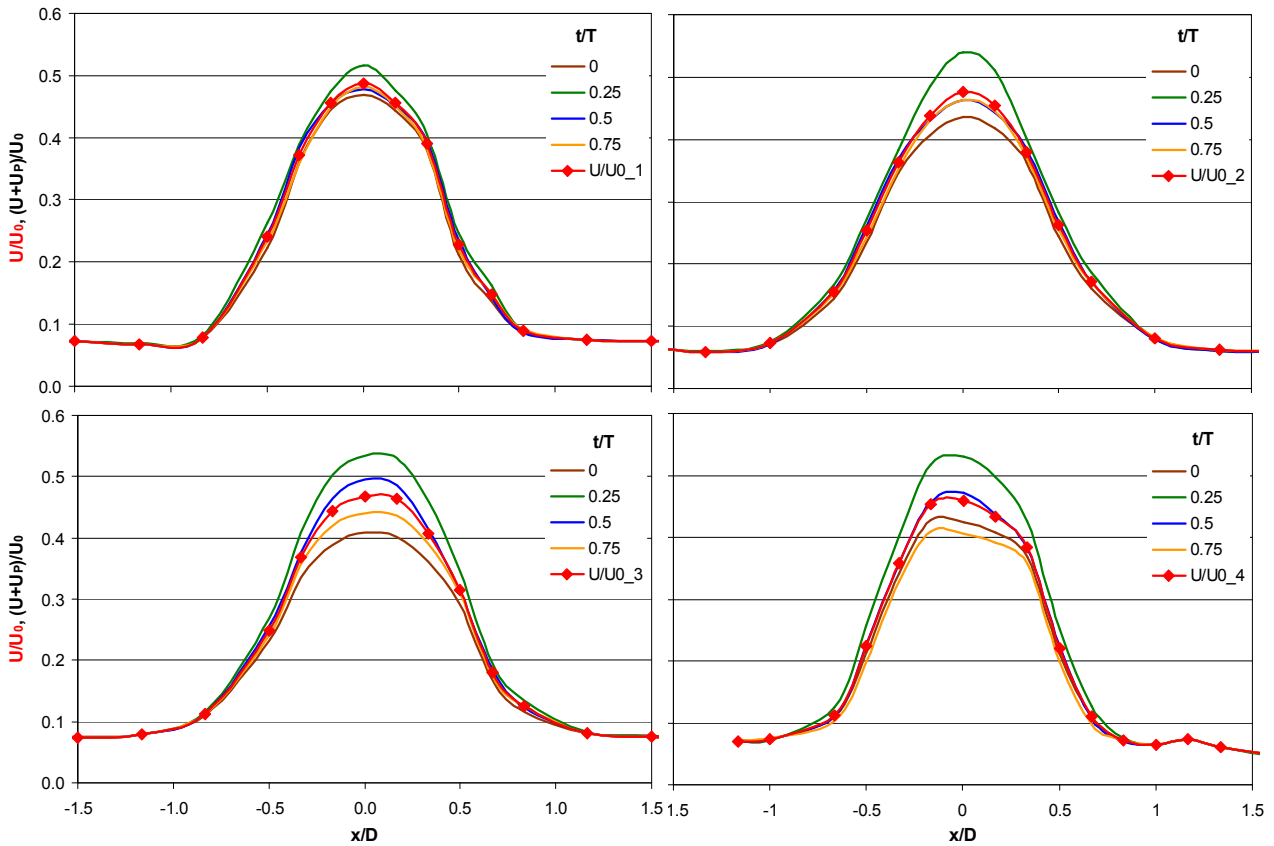


Fig.3.23 Phase-averaged velocity magnitude profiles and time-mean velocity magnitude profile at distance $y/D = 1.5$ (results of CTA experiments)

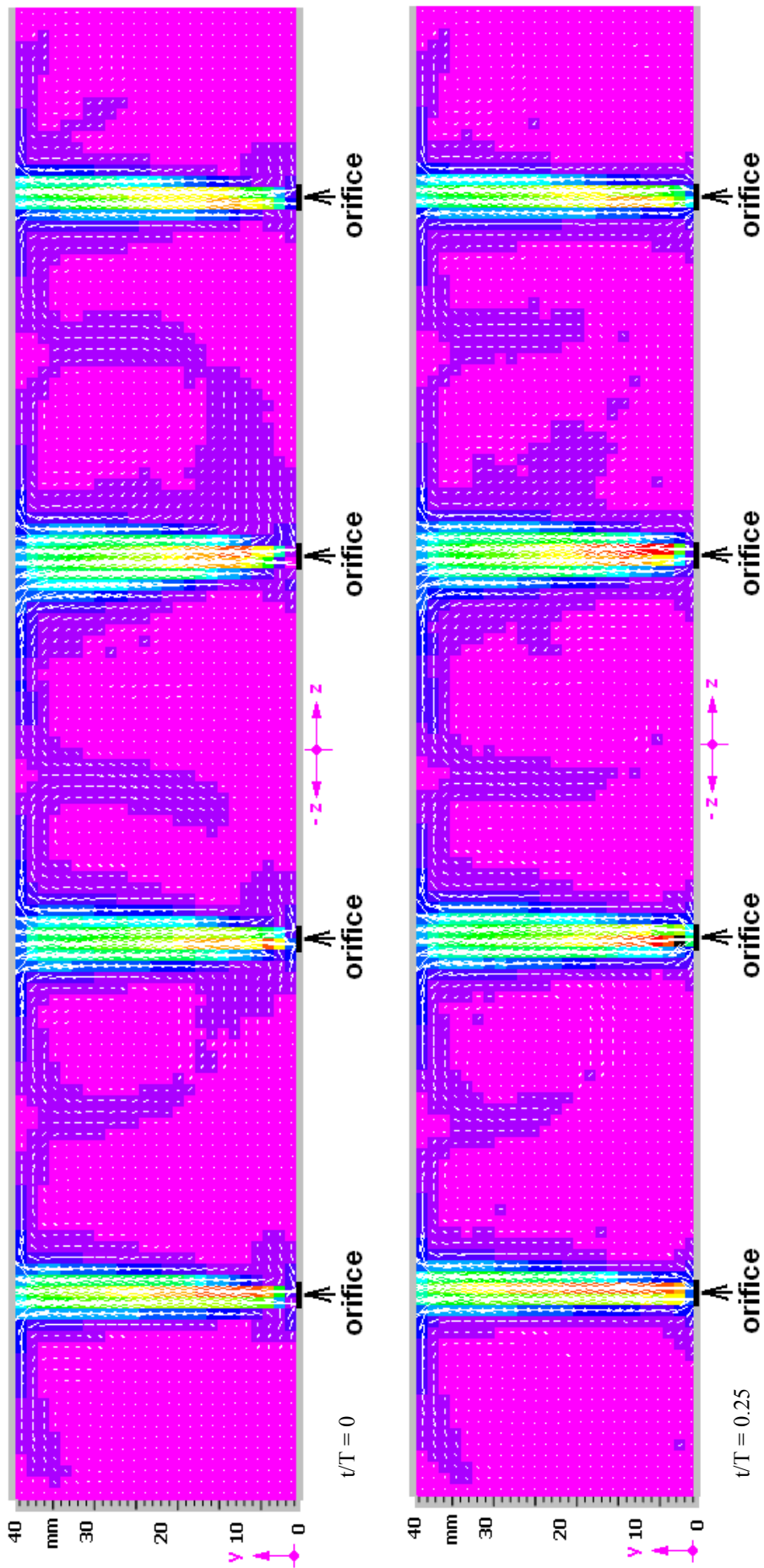


Fig.3.24a SJ array – contours in discrete drawing style and vectors of the phase-averaged velocity magnitude (results of PIV experiments)

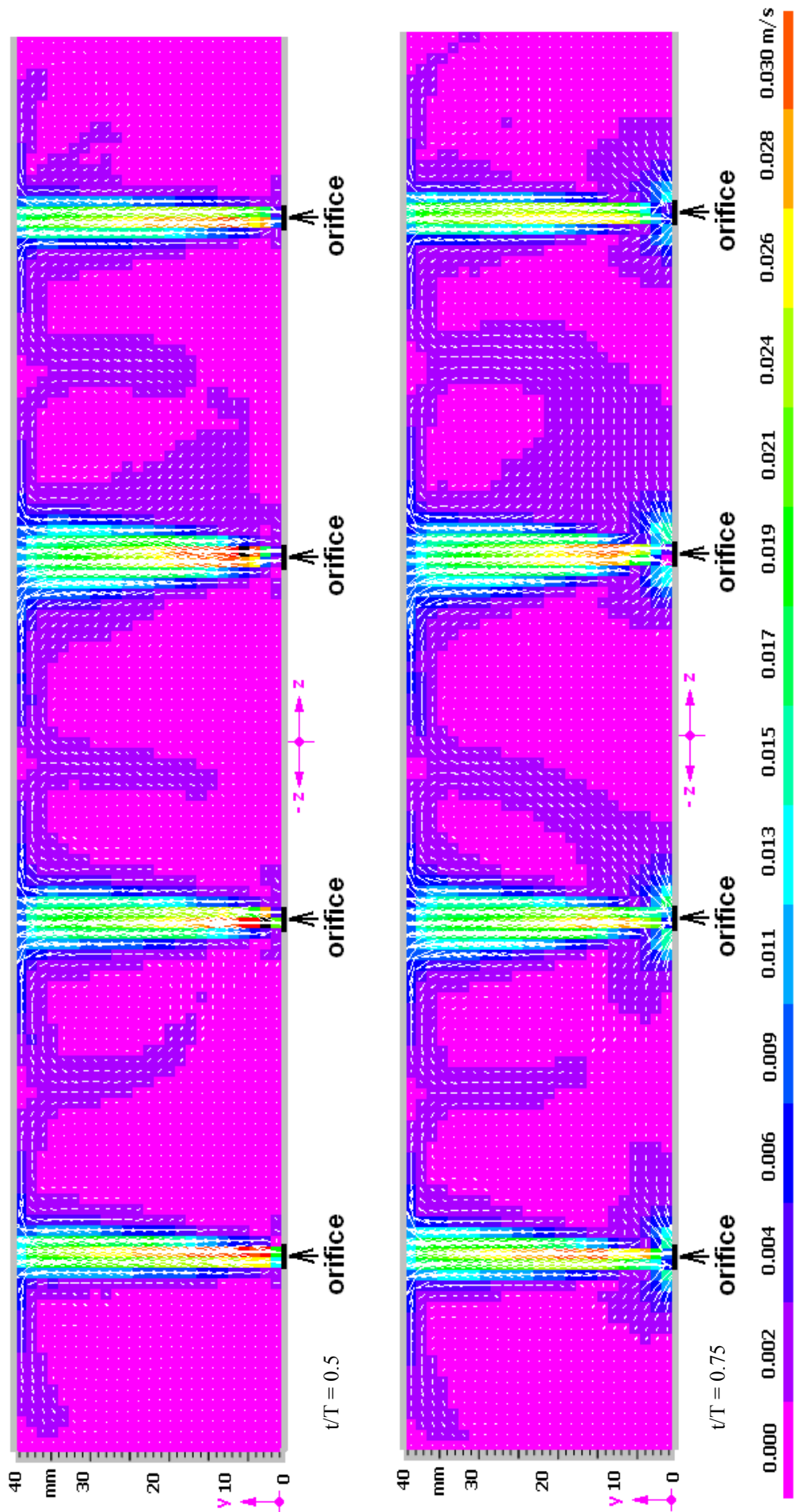


Fig.3.24b SJ array – contours in discrete drawing style and vectors of the phase-averaged velocity magnitude (results of PIV experiments)

Experimental results

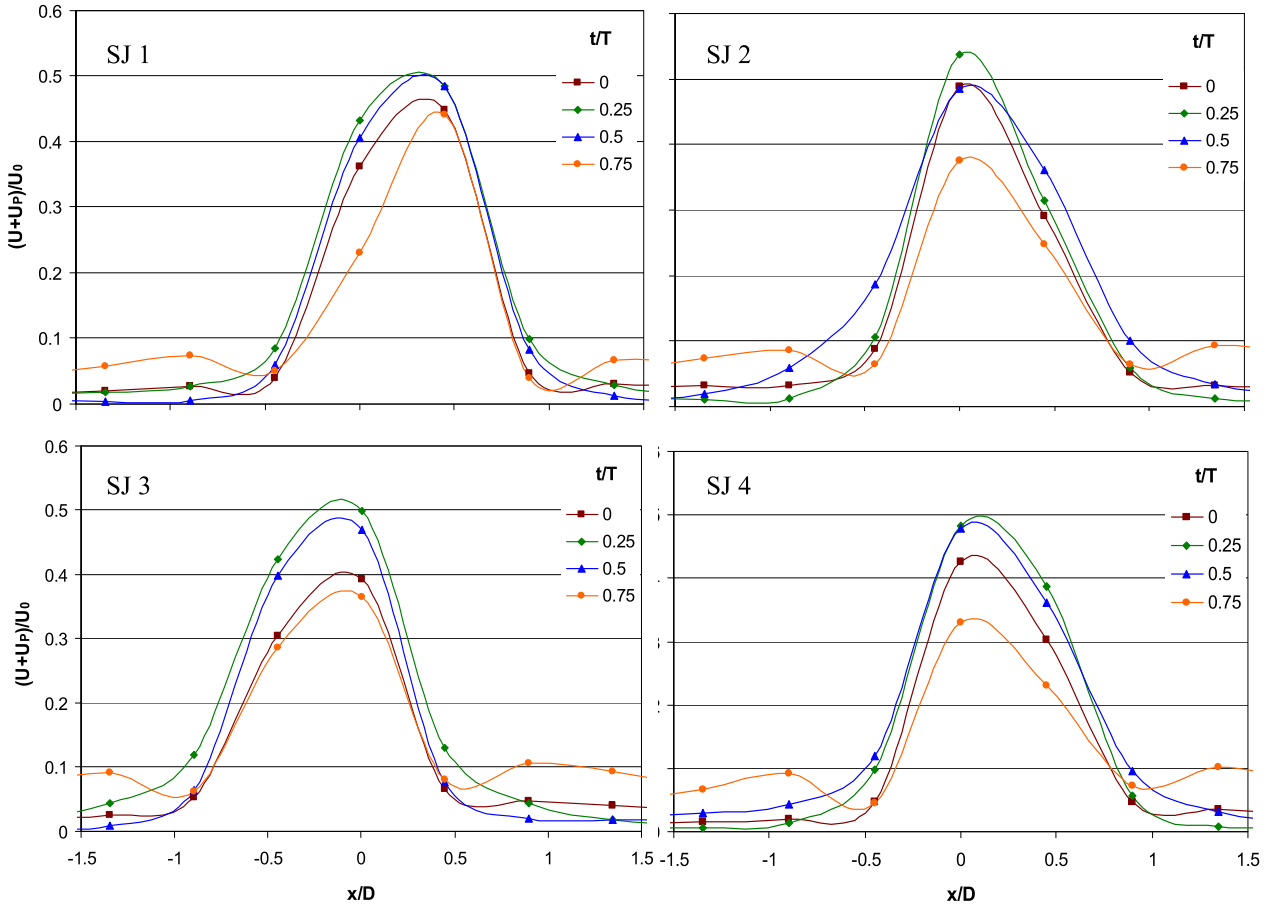


Fig.3.25 Phase-averaged velocity magnitude profiles of a SJ array during the actuation cycle at $y/D = 1.5$ (results of PIV experiments)

Figures 3.26 show the SJ array's phase-averaged velocity magnitude profiles at the instant of maximum extrusion velocity ($t/T = 0.25$) at different distances from the actuators' orifices. As the distance from the orifices increased, the velocity decreased, and velocity profiles widened.

3.3.5 PIV EXPERIMENTS OF A SJ ARRAY IN A CHANNEL FLOW

The experiments were performed at the IT CAS. The delay time between the two laser pulses was $t = 5\text{ms}$. The results plotted in Figure 3.27 are in the form of velocity magnitude contours in time $t/T = 0.25$ (maximum extrusion velocity), measured in the plane of SJs 1, 2, 3, and 4, i.e. $z = (-72, -24, 24, \text{ and } 72)$ mm, with all SJs (1 – 4) operating. SJs 1, 2, 3, and 4 exhibited visible bending, which was smaller than that exhibited by a single SJ. SJs 1, 2, 3, and 4 reached the opposite wall ($y = 40$ mm) at the location of $x = (6-16)$ mm.

Figures 3.28 – 3.31 present phase-averaged velocity magnitude profiles at different distances from the orifices of the SJ array (all SJs were working) in the planes of SJs 1, 2, 3, and 4, i.e. $z = (-72, -24, 24, \text{ and } 72)$ mm, respectively.

Figures 3.28a, 3.29a, 3.30a, and 3.31a show the velocity profile of the channel flow upstream of the SJ actuators. At a distance of $x = -5\text{mm}$, a small influence of the SJs was visible because $(U+U_p)/U_C$ reached a value of 0.4 at a distance of $y/H = 0.01$.

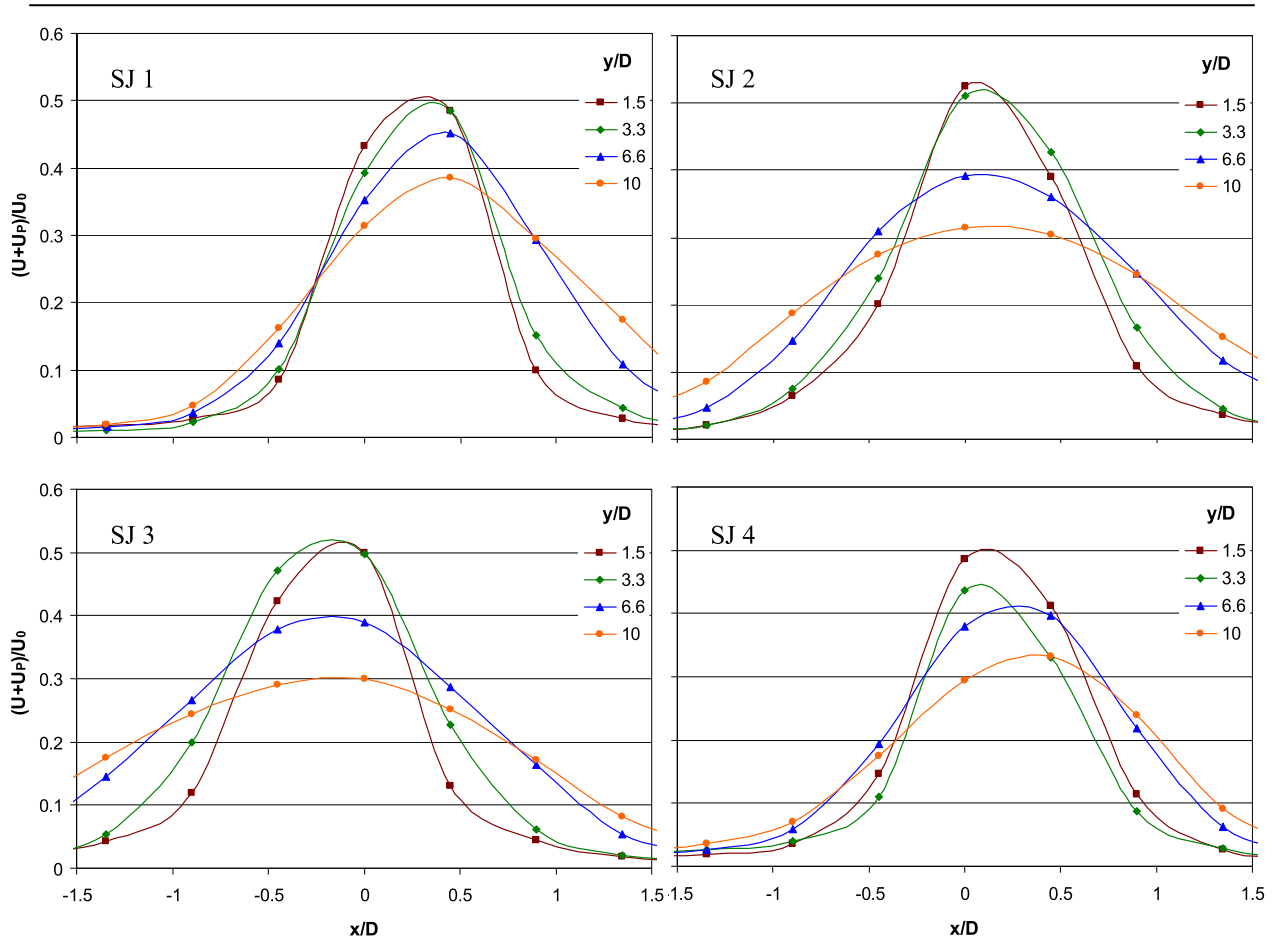


Fig.3.26 Phase-averaged velocity magnitude profiles of a SJ array at the instant of maximum extrusion velocity ($t/T = 0.25$) (results of PIV experiments)

Figures 3.28b, 3.29b, 3.30b, and 3.31b show the influence of the velocity profiles on the top part of the channel. The velocity ratio $(U+U_p)/U_C$ even achieved a value of (2.7-3) at a distance of $x = 10$ mm.

Further downstream, flow development was propagated downwards to the bottom channel wall, and the velocity profiles relaxed back towards parabolic profiles (Figures 3.28 – 3.31c, d). Obviously, the parabolic profiles of the developed channel flow cannot be achieved in the rather short test section, limited by $x = 350$ mm – as is shown in Figures 3.30e, f, and g.

Figure 3.32 shows the results at Plane I, i.e. between SJ 2 and SJ 3, at $z = 0$ mm (see Figure 2.5 and Appendix 2) in the form of phased-average velocity contours. The delay time between the two laser pulses was $t = 25$ ms. The influence of the laminar channel flow from SJ 2 and SJ 3 was visible. In front of the SJ array, the flow velocity decreased markedly due to the blockage effect of SJs on the channel flow (see ellipse mark in Figure 3.32). Behind the SJ array, the channel flow relaxed back to the laminar profile very slowly – cf. velocity profiles shown in Figures 3.28 – 3.31 discussed above.

The time-mean velocity through the channel and the synthetic jets' time-mean orifice velocities were evaluated at approximately $U_C = 0.0067$ m/s and $U_{0_1} = 0.057$ m/s, $U_{0_2} = 0.066$ m/s, $U_{0_3} = 0.063$ m/s, $U_{0_4} = 0.053$ m/s. The associated maximum Reynolds numbers were $Re_C = 536$ and $Re_{SJ_1} = 170$, $Re_{SJ_2} = 199$, $Re_{SJ_3} = 190$, $Re_{SJ_4} = 158$, respectively.

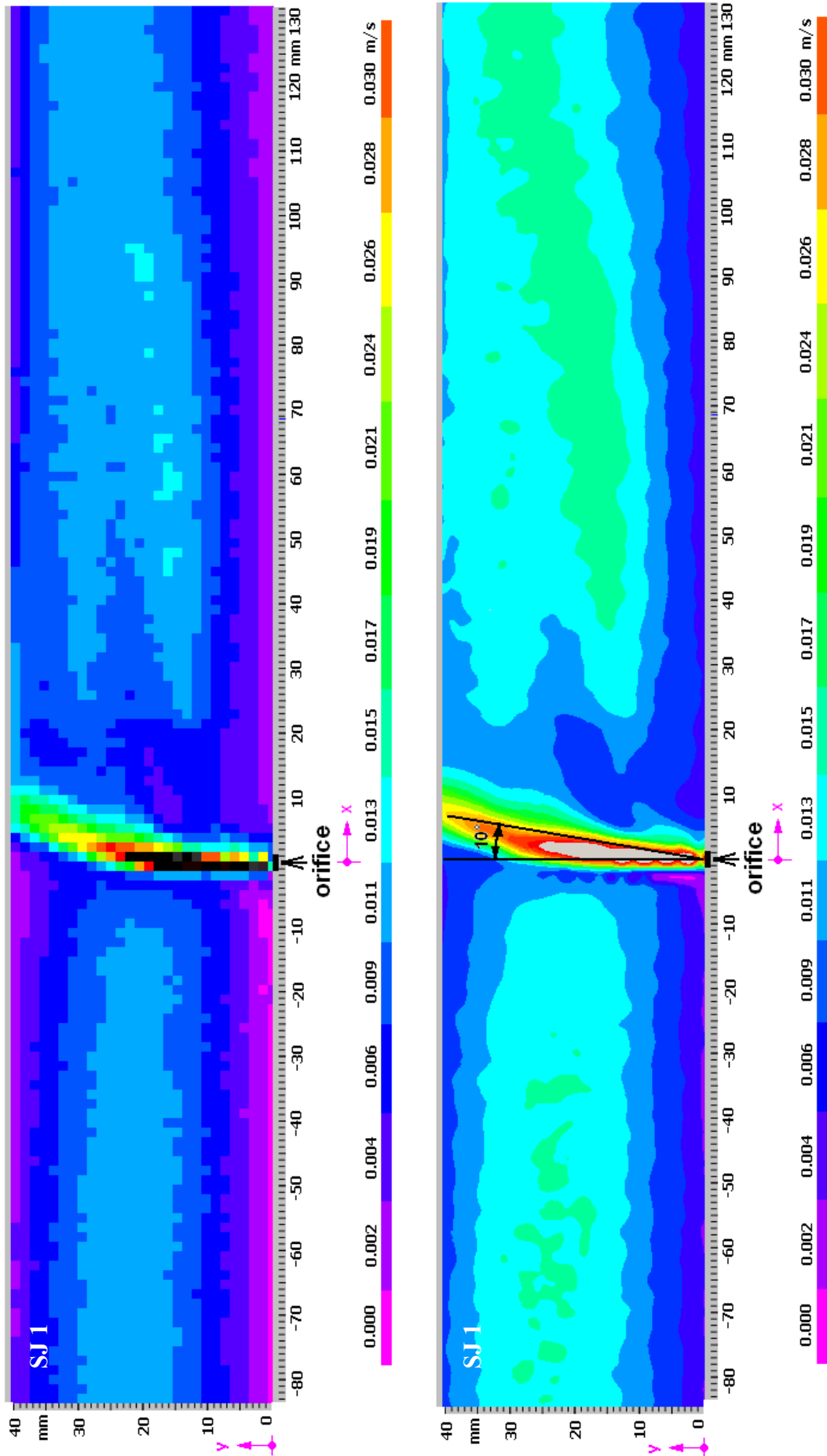


Fig.3.27a Velocity magnitude contours of the channel flow interacting with a SJ array, measured on the plane of SJ 1 (i.e. $z = -72$ mm); upper picture - discrete drawing style, bottom picture - post processing smoothing. Phase-averaged for $t/T = 0.25$ (results of PIV experiments)

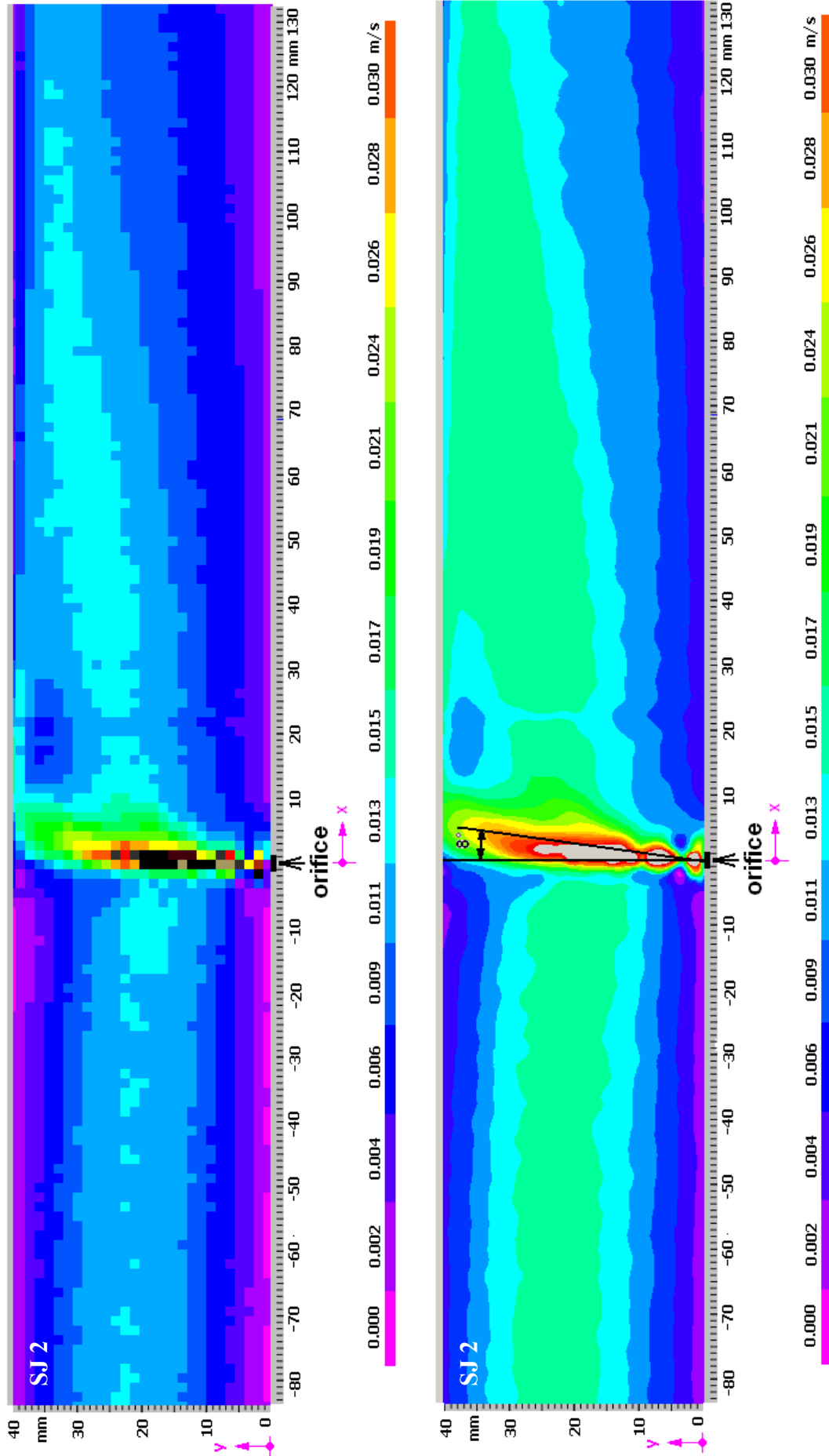


Fig.3.27b Velocity magnitude contours of the channel flow interacting with a SJ array, measured on the plane of SJ 2 (i.e. $z = -24$ mm); upper picture - discrete drawing style, bottom picture - post processing smoothing. Phase-averaged for $t/T = 0.25$ (results of PIV experiments)

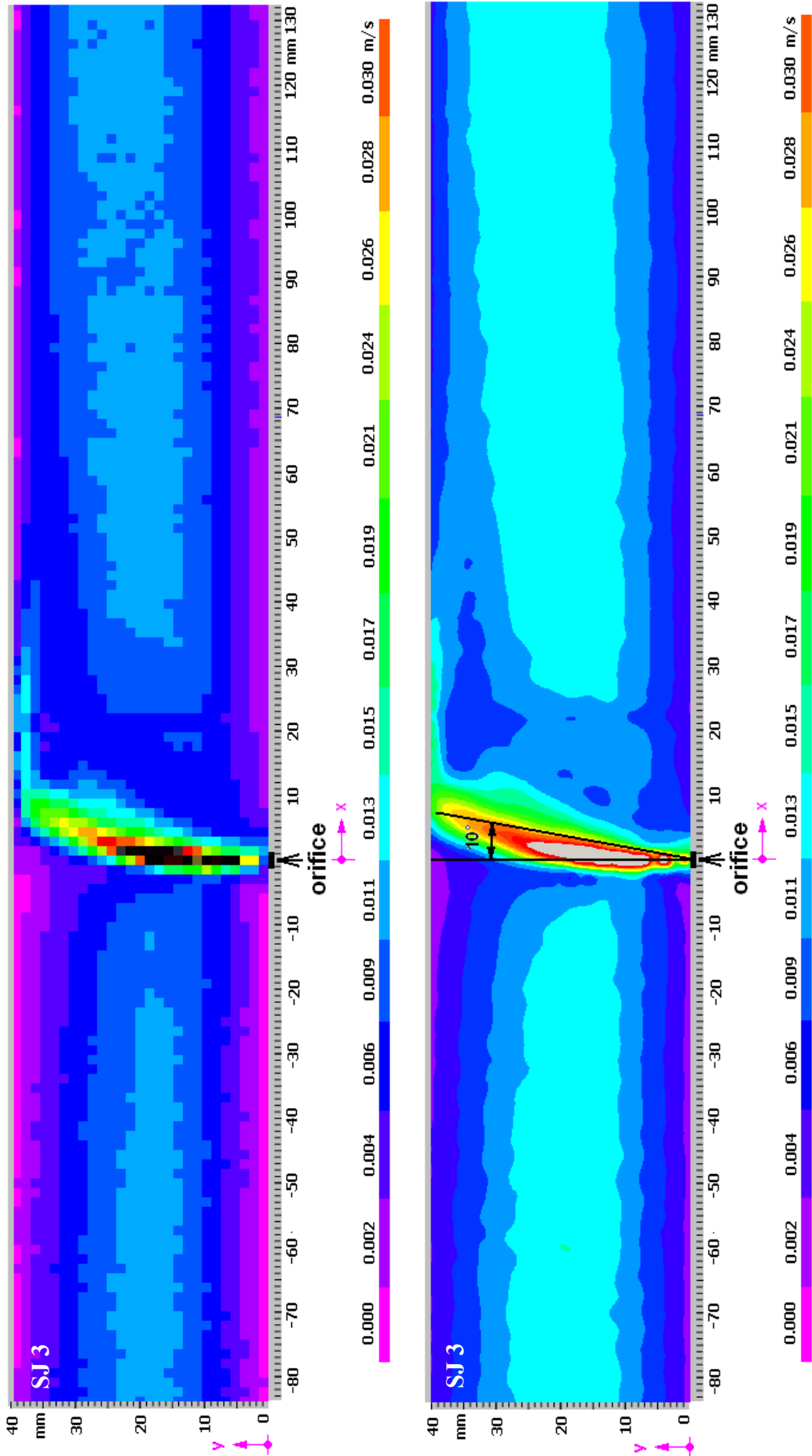


Fig.3.27c Velocity magnitude contours of the channel flow interacting with a SJ array, measured in the plane of SJ 3 (i.e. $z = 24$ mm); upper picture - discrete drawing style, bottom picture - post processing smoothing. Phase-averaged for $t/T = 0.25$ (results of PIV experiments)

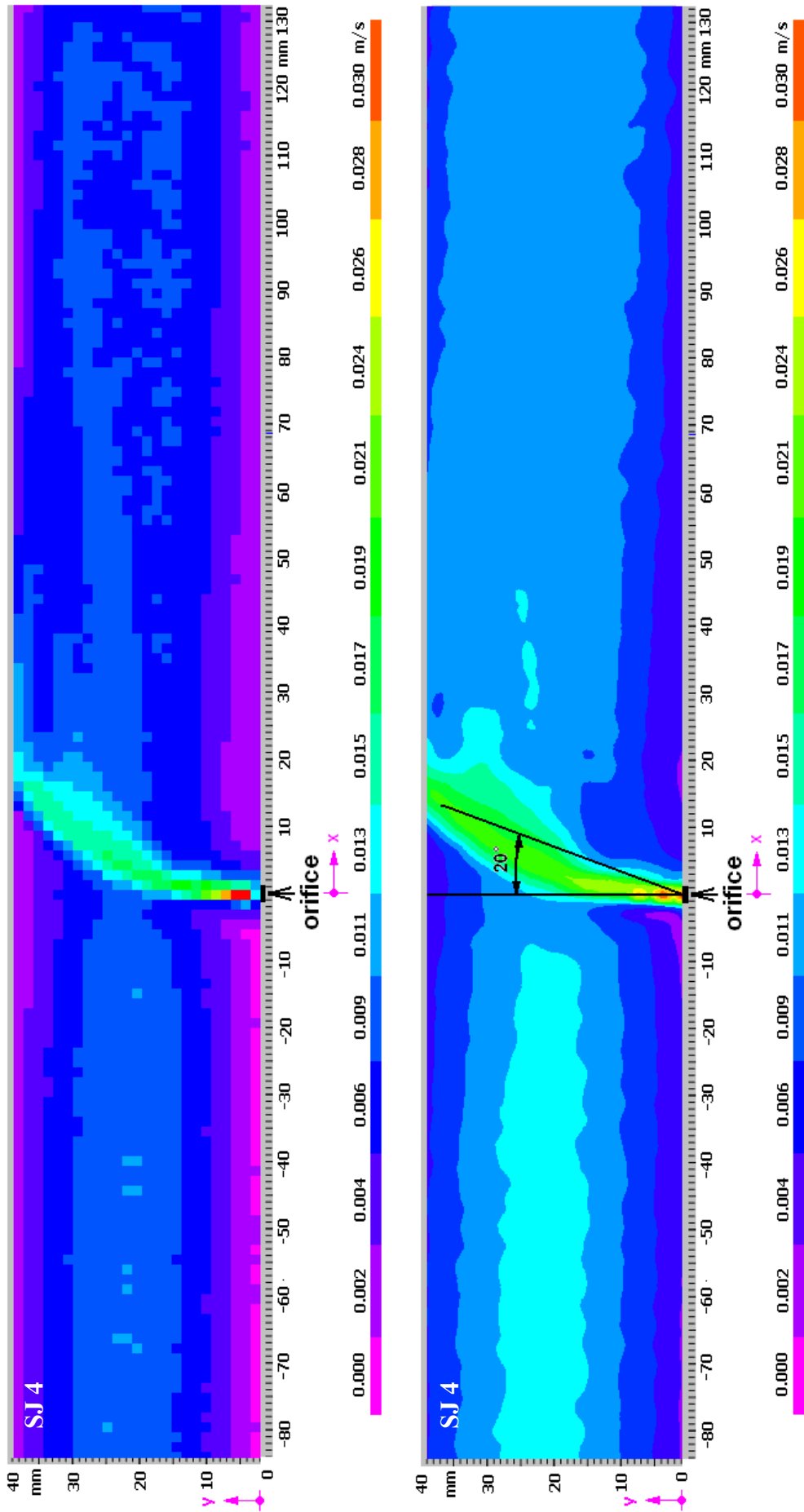


Fig.3.27d Velocity magnitude contours of the channel flow interacting with a SJ 4 array, measured in the plane of SJ 4 (i.e. $z = 72$ mm); upper picture - discrete drawing style, bottom picture - post processing smoothing. Phase-averaged for $t/T = 0.25$ (results of PIV experiments)

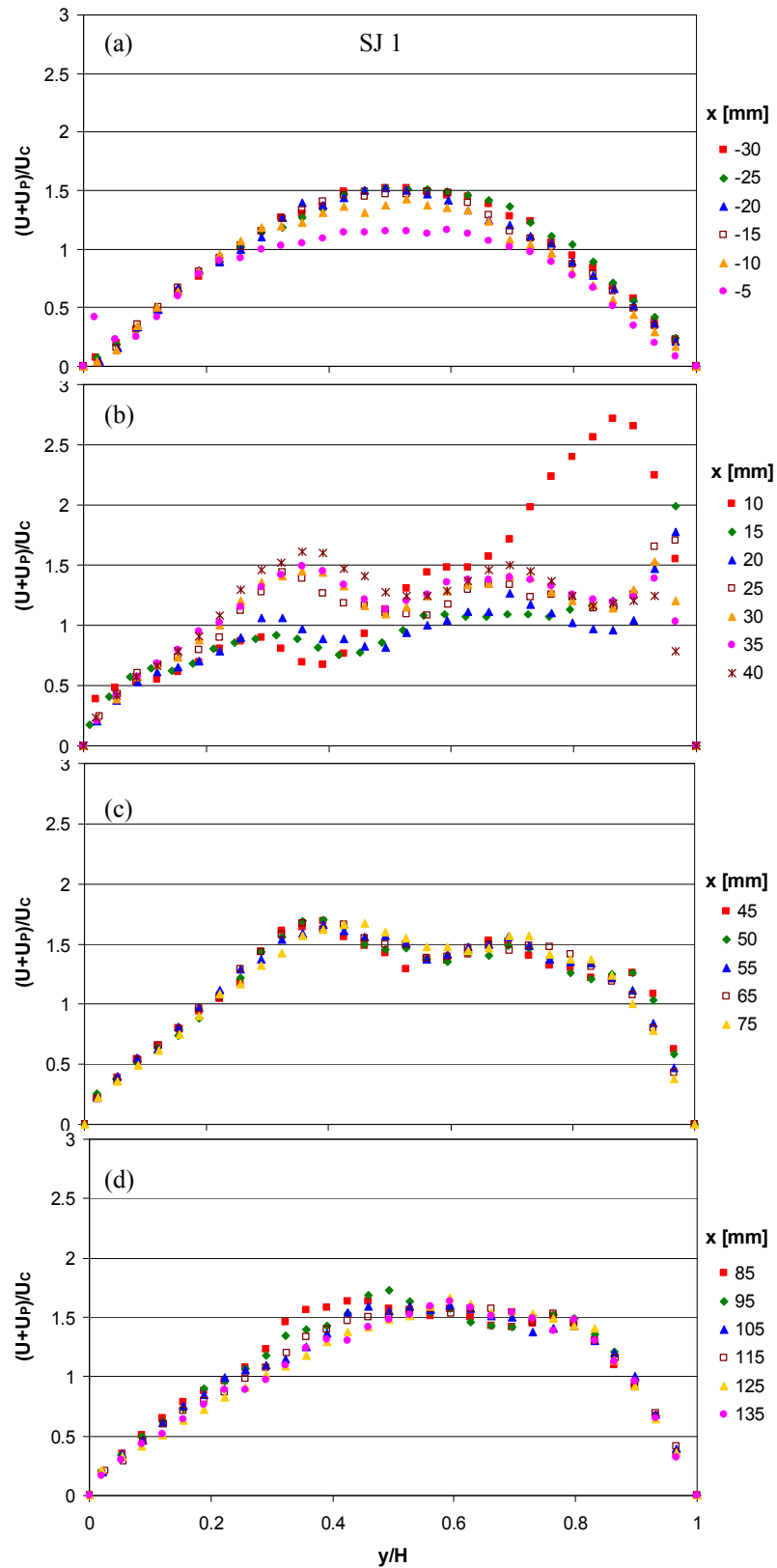


Fig.3.28 Phase-averaged velocity magnitude profiles of the channel flow measured in the plane of SJ 1 (i.e. $z = -72$ mm), $t/T = 0.25$
 (a) $x = (-30 \div -5)$ mm, (b) $x = (10 \div 40)$ mm, (c) $x = (45 \div 75)$ mm, (d) $x = (85 \div 135)$ mm
 (results of PIV experiments)

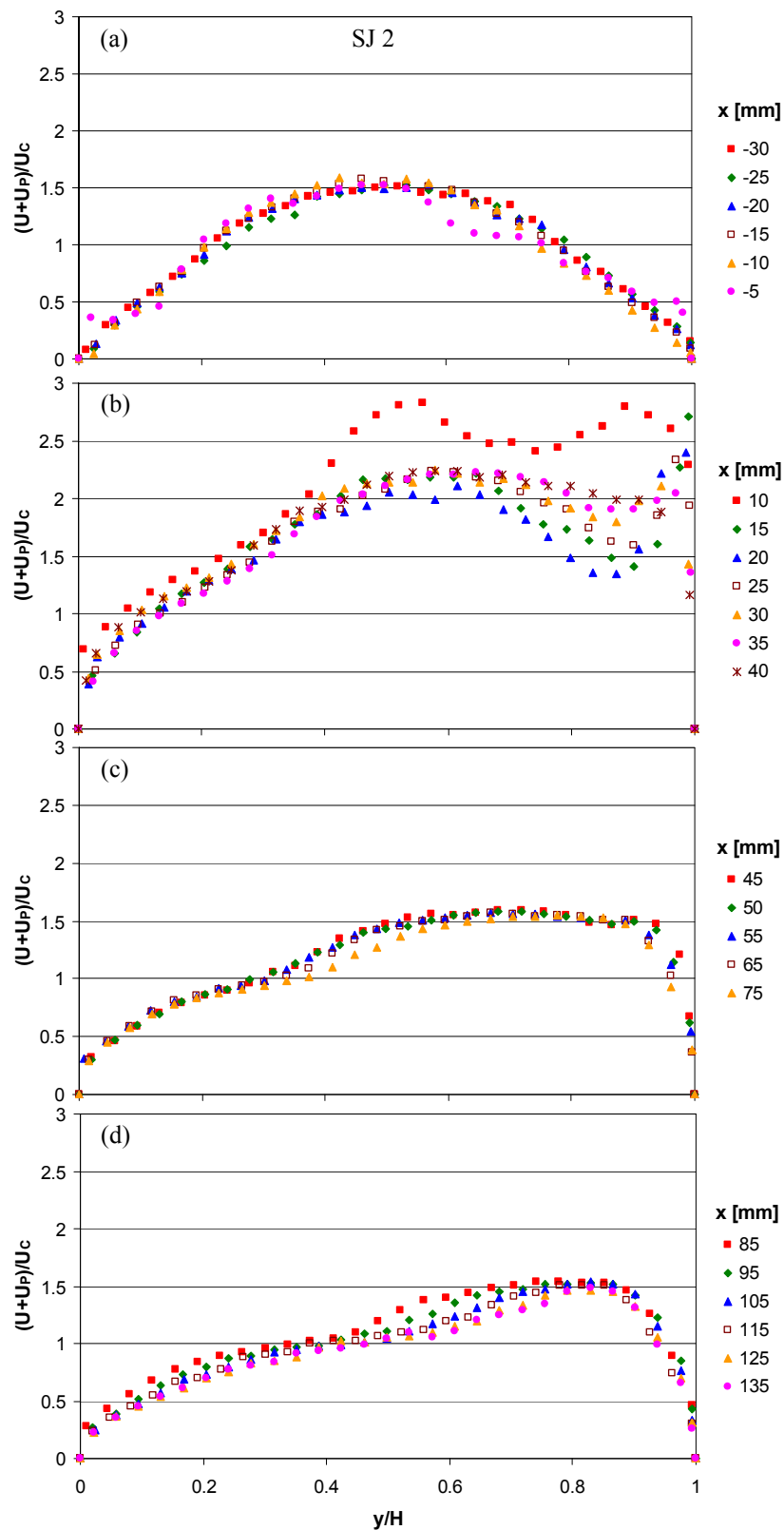


Fig.3.29 Phase-averaged velocity magnitude profiles of the channel flow measured in the plane of SJ 2 (i.e. $z = -24$ mm), $t/T = 0.25$
 (a) $x = (-30 \div -5)$ mm, (b) $x = (10 \div 40)$ mm, (c) $x = (45 \div 75)$ mm, (d) $x = (85 \div 135)$ mm
 (results of PIV experiments)

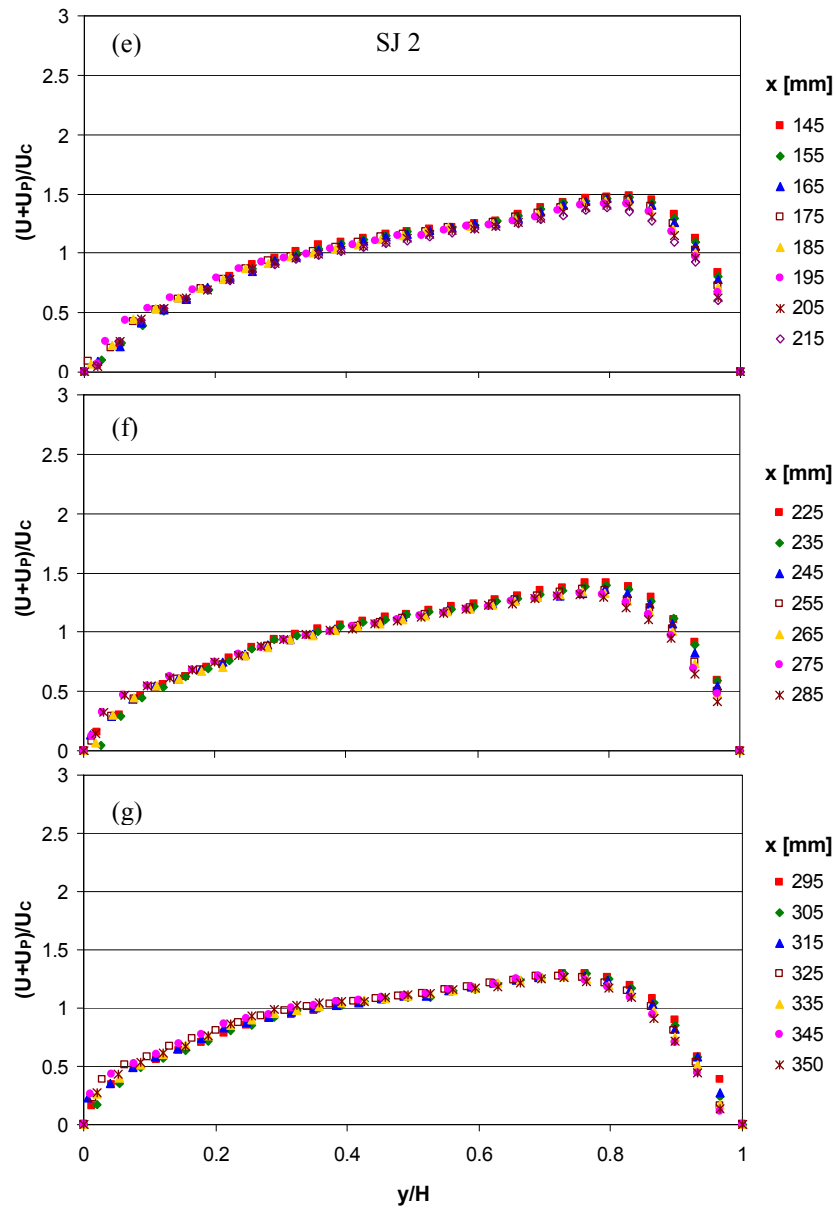


Fig.3.29 Phase-averaged velocity magnitude profiles of the channel flow measured in the plane of SJ 2 (i.e. $z = -24$ mm), $t/T = 0.25$
 (e) $x = (145 \div 215)$ mm, (f) $x = (225 \div 285)$ mm, (g) $x = (295 \div 350)$ mm
 (results of PIV experiments)

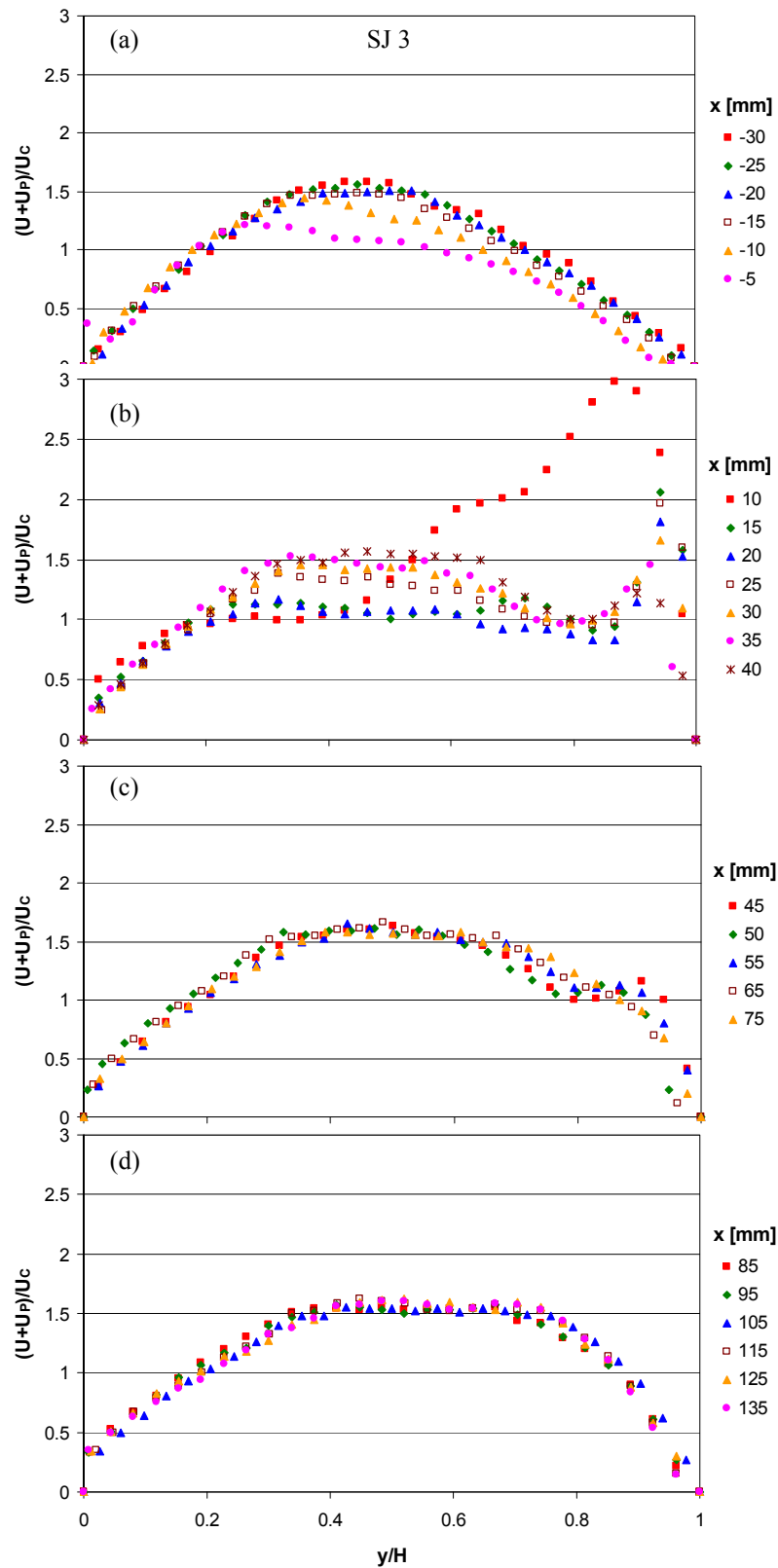


Fig.3.30 Phase-averaged velocity magnitude profiles of the channel flow measured in the plane of SJ 3 (i.e. $z = 24$ mm), $t/T = 0.25$
 (a) $x = (-30 \div -5)$ mm, (b) $x = (10 \div 40)$ mm, (c) $x = (45 \div 75)$ mm, (d) $x = (85 \div 135)$ mm
 (results of PIV experiments)

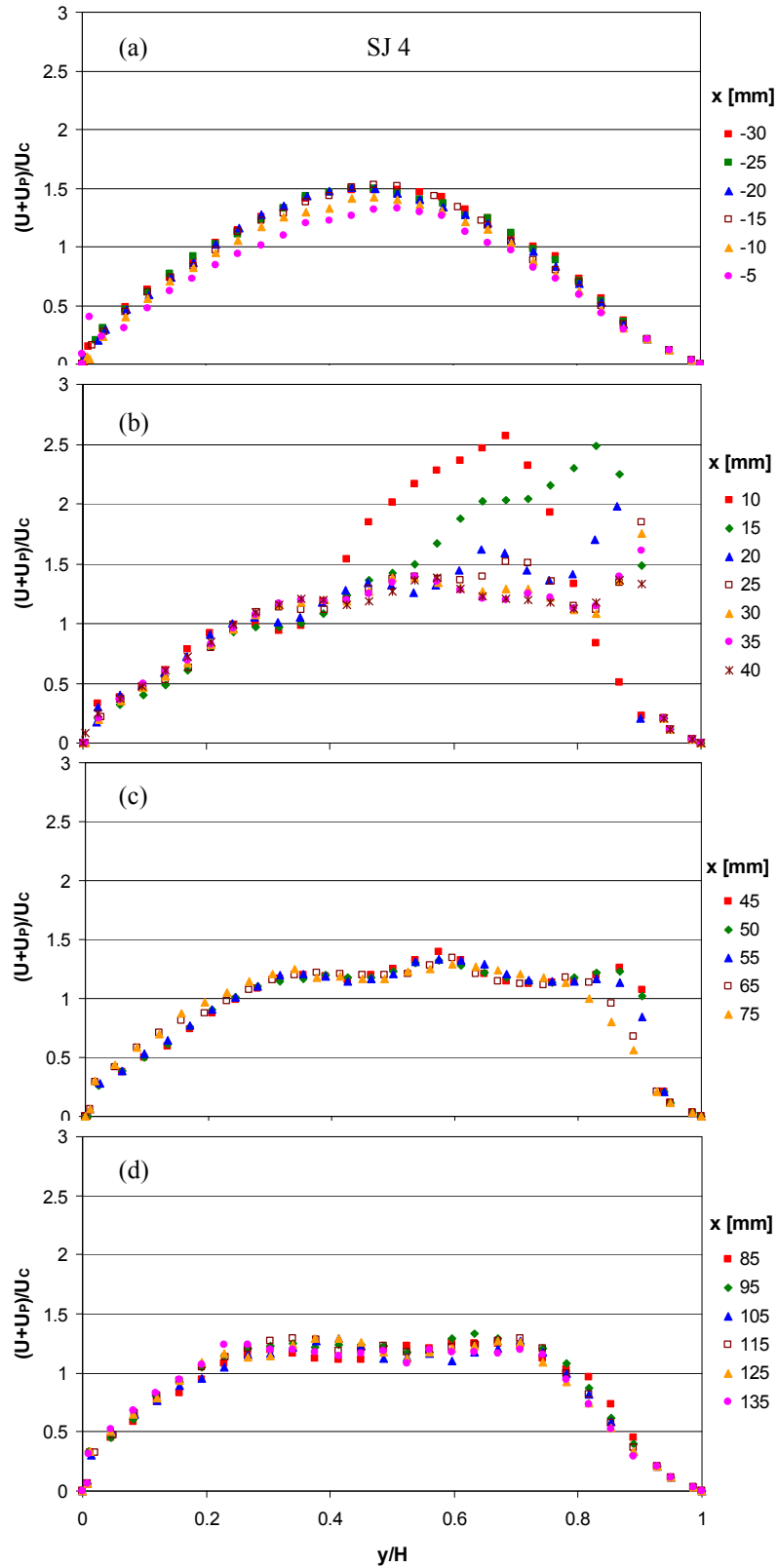


Fig.3.31 Phase-averaged velocity magnitude profiles of the channel flow measured in the plane of SJ 4 (i.e. $z = 72$ mm), $t/T = 0.25$
 (a) $x = (-30 \div -5)$ mm, (b) $x = (10 \div 40)$ mm, (c) $x = (45 \div 75)$ mm, (d) $x = (85 \div 135)$ mm
 (results of PIV experiments)

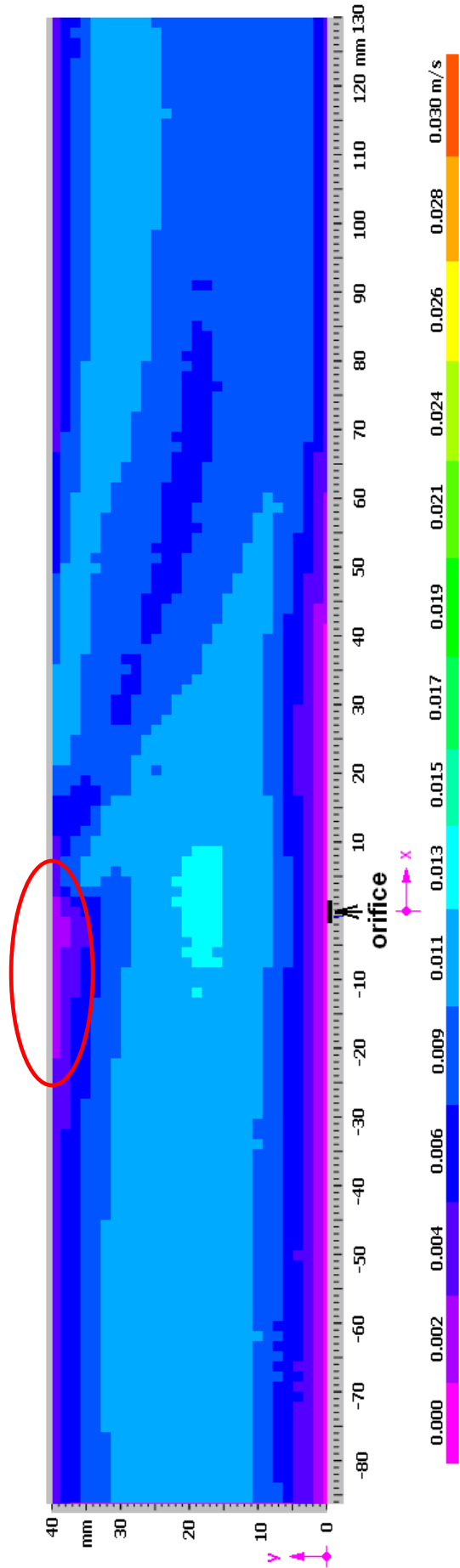


Fig.3.32 SJ array – contours in discrete drawing style of the phase-averaged velocity magnitude on plane I (i.e. between SJ 2 and SJ 3, at $z = 0$ mm, see Fig.2.5b and Appendix 2), (results of PIV experiments)

3.4 OVERVIEW OF THE MAIN RESULTS

The investigation described in this work was focused on a laminar channel flow influenced by a single SJ or SJ array. This configuration can be effective in many micro-scale applications, e.g. in the cooling of microelectronics.

All the experiments were performed using water as the working fluid. The measurements were done at TU Eindhoven (Netherlands), TU Liberec, and IT CAS.

Four SJ devices and two circulation water channels (both described in Chapter 2) were used:

- Synthetic jet actuator, equipped with a sealed cavity and an actuating piezoelectric membrane (KINGSTATE KPS-100); actuator dimensions: orifice diameter $D = 3.0\text{mm}$, cavity diameter $D_D = 36\text{mm}$.
- Tested channel for a single SJ actuator, dimensions: channel length, height, and width were $L_{UP} + L_{DOWN} = 1020\text{mm}$, $H = 40\text{mm}$, and $B = 200\text{mm}$, respectively.
- SJ array setup, dimensions: length, height, and width $L = 210\text{mm}$, $H = 40\text{mm}$, and $B = 200\text{mm}$, respectively. The upper wall was connected with four screws for easy removal.
- Plexiglas wall with SJ array, dimensions: *length (length with start) x width x thickness* = (860 (880) x 200 x 10) mm.
- Circulation water channel at TU Eindhoven with cross section 570mm x 450mm (horizontal x vertical dimensions, respectively); length approx. 2500mm. There were water tanks (approx. dimensions: diameter 1000mm, height 2200mm) at both channel sides. Three pumps on three sectional pipes controlled the water flow rate.
- Circulation water channel at IT Prague with Plexiglas wall equipped with pump to raise water to the top.

For measurement of the problem, the following methods were used:

- Ink visualization: This very simple visualization method was used to obtain the first view of the laminar channel flow. The method was used at TU/e. The ink was put approx. 1m in front of the test section. Due to the geometry of the circulation water channel, it was not possible to visualize the flow with the tin ion method; therefore ink was used because of its simplicity.
- The tin ion method was used for the visualization of a single SJ and a SJ array without channel flow influence. A tin ion transfer was completed between an anode and copper cathode in an electrolytic solution. The experiments were performed at a frequency of $f = 15\text{Hz}$. A voltage of $E = 30\text{V}$ and current of $I = 0.1\text{A}$ was used for electrolysis. For lighting, a continuous ND:YV04 laser with a power output of 300 mW and a New Wave Gemini laser for the PIV system with a power output of 120 mJ per pulse were used.
- Hot-wire anemometry in constant temperature mode was used for determining the SJ actuator's natural frequency and for measuring SJ velocity. For experiments, the DANTEC system was used: a hot-film 55P36 probe, a 90C10 anemometer, a NI_CA1000 bus bar, and a NI-PCI-MIO-16E-1 A/D converter. The measured data was analyzed using StreamWare 3.01 and Microsoft Excel.
- Laser Doppler vibrometry was used for PCT behavior investigation. Using LDV, the velocity of a membrane center was measured, from which membrane center displacement was calculated. After considering the continuity equation, the jet velocity was evaluated from the membrane center velocity during the period. LabView software was used to acquire and analyze the signal obtained from the Ometron vibrometer.

Microsoft Excel was used to make additional calculations and analysis. LDV was also used to find PCTs, which worked without phase shift, for the SJ array.

- Particle image velocimetry was used to investigate channel flow without the interaction of single SJ/SJ array, to investigate a single SJ/SJ array in quiescent fluid, and to investigate a single SJ/SJ array in a cross-flow. Two PIV systems (TU/e and TUL) were used. To properly complete the experiments, the SJ actuator (master) and the laser system (slave) had to be synchronized.

Five types of experiments were carried out:

- Channel flow without the interaction with the single SJ or SJ array,
- Single SJ in quiescent fluid,
- Single SJ interacting with the channel flow,
- SJ array in quiescent fluid,
- SJ array interacting with the channel flow.

All the experiments with the single SJ or SJ array were made at a constant true rms AC voltage of 19.5 V. For the single SJ, the true rms AC current was 40 mA, and the apparent electric power was 0.8W. For the SJ array, the true rms AC current was approx.0.164 A, and the apparent electric power was 0.8W for each actuator (3.2W for the whole SJ array).

The working (resonant) frequency was 15 Hz.

Table 1 compiles the main results of this work.

Table 1. Channel flow, single SJ, and SJ array parameters for the presented experiments in water

Channel flow				
U_C at TU/e (m/s)	0.006	U_C at IT CAS (m/s)	0.0067	
Re_C at TU/e	480	Re_C at IT CAS	536	
SJ actuator nominal frequency				
Resonant frequency acquired from the experiments (Hz)	15.0	Calculated resonant frequency (Hz)	19.7	
Single SJ				
U_0 (m/s)	0.059			
$L_0/D = U_0/(fD)$	1.31			
$Re_{SJ} = U_0D/\nu$	177			
$St = (1/\pi)D/L_0$	0.25			
SJ deflection φ (°) in the middle of the channel (Fig. 3.14)	22°, from $y = 24\text{mm}$, the deflection is 55° from vertical position			
$c_U = U_0/U_C$	9.84			
$c_Q = U_0A/(U_CBH)$	0.009			
$c_M = (5\pi^2/24)(A/A_C)(U_0/U_C)^2$	0.18			
SJ array				
	SJ 1	SJ 2	SJ 3	SJ 4
U_0 (m/s)	0.057	0.066	0.063	0.053
$L_0/D = U_0/(fD)$	1.27	1.46	1.4	1.2
$Re_{SJ} = U_0D/\nu$	170	199	190	158

Experimental results

SJ array				
	SJ 1	SJ 2	SJ 3	SJ 4
$St = (1/\pi)D/L_0$	0.25	0.22	0.23	0.27
SJ deflection flow φ (°) in the middle of the channel (Fig. 3.27)	10	8	10	20
$c_U = \frac{1}{n} \sum_{i=1}^n \left(\frac{U_{0i}}{U_C} \right)$				8.92
$c_Q = \frac{A}{A_C} \sum_{n=1}^n \left(\frac{U_{0i}}{U_C} \right)$				0.03
$c_M = \frac{5\pi^2}{24} \left(\frac{A}{A_C} \right) \sum_{i=1}^n \left(\frac{U_{0i}}{U_C} \right)^2$				2.31

Because a single SJ and each actuator in a SJ array use the same power (0.8 W), SJ array bending is smaller than the bending of a single SJ (see Figures 3.14 and 3.27).

CHAPTER 4

CONCLUSIONS

4.1 SUMMARY AND EVALUATION OF THE WORK

The aims of this thesis were formulated with five objectives in paragraph 1.3. All of these objectives were fulfilled, as summarized below point by point.

The thesis investigated the influence of a laminar channel flow with a single synthetic jet or a synthetic jet array; the working fluid was water. The investigation was focused on low Reynolds numbers (in order 10^2) because the arrangement can be useful in many micro-scale applications, such as the cooling of microelectronics or the detection of various (biological, biomedical, or chemical) species. The flow regime in micro-scale is usually laminar with very small Reynolds numbers.

The experiments were carried out at Eindhoven University of Technology (Netherlands), the Technical University of Liberec, and the Institute of Thermodynamics AS CR (both Czech Republic).

Two PIV systems (TU/e and TUL) were used. To properly complete the experiments, the SJ actuator (master) and the laser system (slave) had to be synchronized.

The aims of the work were carried out:

- Design of experimental setups:
 - SJ actuator: consisting of a sealed cavity and a KINGSTATE KPS-100 PCT, orifice diameter of $D = 3.0\text{mm}$, orifice height of 5 mm, cavity diameter of $D_D = 36\text{mm}$, and a cavity height of 5 mm.
 - Plexiglas test channel with a single SJ: inner dimensions of the channel – *width x height x length* = (200 x 40 x 1020) mm; SJ actuator was placed 520mm from the beginning.
 - Two experimental setups with a SJ array: consisting of four SJ actuators across the channel cross section:
 - a) SJ equipment with SJ array: *width x height x length* = (200 x 40 x 210) mm.
 - b) Plexiglas wall with SJ array: *length (length with start) x width x thickness* = (860 (880) x 200 x 10) mm. The SJ array was placed 520mm from the beginning.
- The resonance frequency of the developed actuator was theoretically analyzed as 19.7Hz and during the hot wire anemometry experiments obtained as 15Hz.
- Auxiliary experiments prepared and carried out:
 - Flow visualization was performed using two methods:

- a) Ink visualization for laminar channel flow was used at TU/e because of its simplicity and the impossibility to use the tin ion method. The ink was put approx. 1m in front of the test section.
- b) Tin ion method for visualization of a single SJ and SJ array without laminar channel flow.
- Laser Doppler vibrometry was used to measure the velocity of the PCT membrane centre. LDV was also used to find PCTs that worked without phase shift for the SJ array.
- Hot wire anemometry in a constant temperature mode was used to determine SJ actuator natural frequency and to measure SJ velocity.
- The main part of experiments was performed by means of particle image velocimetry. The following were investigated using PIV:
 - Laminar channel flow itself,
 - Single SJ in quiescent fluid,
 - Single SJ in a laminar channel flow,
 - SJ array in quiescent fluid,
 - SJ array in a laminar channel flow.
- The obtained results were analyzed:
 - PCTs were fed with a sinusoidal signal. A single SJ was fed with a constant true rms AC voltage of 19.5 V; the true rms AC current was approx. 40 mA, and the apparent electric power was 0.8W. The SJ array was fed with a constant true rms AC voltage of 19.5 V; the true rms AC current was approx. 0.164 A, and the apparent electric power was 0.8W for each actuator (3.2W for the entire SJ array).
 - From LDV experiments and the continuity equation, the velocity in the orifice $u_0(t)$ was evaluated; the mean time orifice velocity and Reynolds number were calculated as $U_0 = 0.059\text{m/s}$ and $Re_{SJ} = 177$ for a single SJ and $U_{0_1} = 0.057\text{m/s}$, $U_{0_2} = 0.066\text{m/s}$, $U_{0_3} = 0.063\text{m/s}$, $U_{0_4} = 0.053\text{m/s}$ and $Re_{SJ_1} = 170$, $Re_{SJ_2} = 199$, $Re_{SJ_3} = 190$, $Re_{SJ_4} = 158$ for a SJ array.
 - Using HWA, velocity profile experiments in the horizontal plane (axis x) and in the flow direction (axis y) were performed. Results of these measurements were also used for setting the velocity range in the post-processing of PIV measurements (range validation in DynamicStudio v.2.30, DANTEC). The precise calibration of the hot film probe was performed using a towing tank at TUL.
 - The main experiments were performed using PIV. Two different PIV systems were used – one at TU/e and one at TUL. Since the first experiments were conducted at TU/e, all experimental conditions (Plexiglas channel dimensions and the setting of channel flow velocity) were adapted to possibilities offered by their laboratory. Subsequent experiments at TUL and IT CAS were adjusted to these conditions. SJ and SJ array experiments without channel flow were performed. The channel flow with and without interaction of a SJ and SJ array was measured. The experiments investigated how the laminar velocity profile in a channel was disturbed by the interaction of a SJ/SJ array.
 - Based on the performed experiments, it can be stated that this configuration (on a micro-scale) is very useful for (micro) cooling applications.
 - Despite the experiments being carried out in three different laboratories, with different systems and setups, the results corresponded closely with each other and provided a perfect view of the SJ problem.

4.2 FUTURE WORK

Based on this work, further possibilities of future research in the field of SJs can be planned.

The results of the experiments are affected by fact that the influenced flow was not stabilized back to laminar due to the insufficient length of the test channel. It would be wise to carry out the experiments with new longer test channel.

In a task of a channel flow with a single SJ, the angle of the SJ and the influence of the channel width can be investigated. The issue of SJ array affection, the influence of various arrangements of SJs (location, shape, or even angle) orifices, can be investigated.

Measurements can be performed on micro-dimensions using a micro-PIV system.

This arrangement is very suitable for heat and mass transfer. Mass transfer in air, with the help of a SJ, using the naphthalene method has been investigated by Trávníček *et al* e.g. in works [41, 42, 44, 45, 46 and A18]. Heat transfer can be investigated using a glue film probe (e.g. from DANTEC, type 55R47). Nevertheless, this type of probe only enables the investigation to be conducted in air. For measurements in water, a different probe must be used, or an entirely new probe must be designed and constructed.

REFERENCES

- [1] Noskievič, J et *al.*: *Mechanika tekutin*. SNTL, Praha (1987), in Czech.
- [2] Dyban E.P., and Mazur A.I.: *Convection Heat Transfer in Impinging Jets (Konvektivnyj teploobmen pri strujnom obtekanii tel)*. 1st ed., Naukova dumka, Kiev (1982), in Russian.
- [3] Martin H.: Heat and mass transfer between impinging gas jets and solid surfaces. *Adv. Heat Transfer*, Vol. 13 (1977) pp. 1–60.
- [4] B.L. Smith, A. Glezer: The formation and evolution of synthetic jets. *Phys. Fluids* 10 (1998) 2281-2297.
- [5] J.E. Cater, J. Soria, The evolution of round zero-net-mass-flux jets. *J. Fluid Mech.* 472 (2002) 167–200.
- [6] A. Glezer, M. Amitay: Synthetic jets. *Annu. Rev. Fluid Mech.* 34 (2002) 503–529.
- [7] T.M. Dauphinee: Acoustic air pump. *The Review of Scientific Instruments*, 28, No.6 (1957) 456.
- [8] Y. Yassour, J. Stricker, M. Wolfshtein: Heat transfer from a small pulsating jet. *Proceedings of the 8th International Heat Transfer Conference*, Vol. 3, Hemisphere Publ., San Francisco, USA (1986) 1183-1186.
- [9] H.U. Meier, M.D. Zhou: The development of acoustic generators and their application as a boundary layer transition control device. *Exp. Fluid* 11 (1991) 93-104.
- [10] E.P. Mednikov, B.G. Novitskii: Experimental study of intense acoustic streaming. *Sov. Phys. Acoust.* 21 (1975) 152-154.
- [11] V. Tesař: Fluidic Jet-Type Rectifier: Experimental Study of Generated Output Pressure. *Fluidics Quarterly, An Arbour U.S.A.*, Vol. 14, Nr. 4 (1982).
- [12] V. Tesař: Entrainment action of an alternating inflow into and outflow from a nozzle. *Acta Polytechnica – Práce ČVUT v Praze* (1991) 43-61 (in Czech).
- [13] A. Meissner: Über piezo-elektrische Kristalle bei Hoch-frequenz. *Zeitschrift für technische Physik*, Vol. 7, No. 12 (1926) 585-592.
- [14] M.J. Lighthill: Acoustic Streaming. *J. Sound Vib.* 61 (1978) 391-418.
- [15] J.T. Stuart: Double boundary layers in oscillatory viscous flow. *J. Fluid Mech.* 24 (1966) 673-687.
- [16] B.J. Davidson, N. Riley: Jets induced by oscillatory motion. *J. Fluid Mech.* 53 (1972) 287.
- [17] U. Ingard: On the theory and design of acoustic resonators. *J. Acoustical Soc. of America*, Vol. 25, No. 6 (1953) 1037-1060.
- [18] V. Lebedeva: Experimental study of acoustic streaming in the vicinity of orifices. *Sov. Phys. Acoust.* 26 (1980) 331.
- [19] Z. Trávníček, Annular impinging jet with acoustic actuation - flow visualization and mass transfer on exposed walls, (Anulární impaktní proud s akustickým buzením - vizualizace proudového pole a přestup hmoty na obtékané stěně). *Research Report IT CAS CR, Prague, Z-1310/01, 2001.*
- [20] Z. Trávníček: Příklady použití kouřové vizualizace proudění v experimentální mechanice tekutin. *Vytápění větrání instalace*, Vol. 11, No. 5 (2002) 230-233.

- [21] B.L. Smith, A. Glezer: Jet vectoring using synthetic jet. *J. Fluid Mech.* 458 (2002) 1-34.
- [22] M.W. Bettridge, R.E. Spall, B.L. Smith: Aerodynamic jet vectoring using steady blowing and suction. 42nd AIAA Aerospace Sciences Meeting, Reno, NV (2004) AIAA 2004-0921.
- [23] D.A. Tamburelo, M. Amitay: Three-dimensional interactions of free jet with a perpendicular synthetic jet. *J. of Turbulence*, Vol. 8, No. 38 (2007).
- [24] M. Amitay, D. R. Smith, V.Kibens, D. E. Parekh, A. Glezer: Aerodynamic flow control over an unconventional airfoil using synthetic jet actuators. *AIAA J.* 39 (2001) (3) 361 – 370.
- [25] M. Amitay, A. Glezer: Controlled transients of flow reattachment over stalled airfoils. *Int. J. Heat Fluid Flow* 23 (2002) 690-699.
- [26] Renault Altica: 44MPG Diesel Concept with Active Airflow Management. [http://www.greencarcongress.com/2006/02/renault_altica_html_\(cited 16/03/2007\)](http://www.greencarcongress.com/2006/02/renault_altica_html_(cited%2016/03/2007).).
- [27] A. Nishizava, S. Takagi, H. Abe, R. Maeda, and H. Yoshida: Toward smart control of separation around a wing – Active separation control system part 2. *Proc. 5th Symp. Smart Control of Turbulence*, Tokyo (2004) 7-14.
- [28] R. Mittal, P. Rampungoon: On the virtual aeroshaping effect of synthetic jets. *Phys. Fluids* 14 (2002) 1533-1536.
- [29] F.J. Chen, G.B. Beeler: Virtual shaping of a two-dimensional NACA 0015 airfoil using synthetic jet actuator. *AIAA Paper* (2002) 3273.
- [30] C.C. Chen, C.C. Chou, S.S. Hsu., A.B. Wang: Visualization of new synthetic jet actuator for underwater vehicles. In: *Proc. 12th Inter. Symp. on Flow visualization ISFV-12*, Sept. 10-14, 2006, Göttingen, Germany, No. 864.
- [31] V. Tesař: Fluidics applied to flow control by synthetic jets. In: *Topical Problems of Fluid mechanics 2006*, Feb. 22-24, 2006, Institute of Thermomechanics, Prague, 171-174.
- [32] V. Tesař, J. Kordík, M. Daněk, Lift and separation control on wind turbine blades by vortices having streamwise oriented axes. *Colloquium Fluids Dynamics 2008*, Institute of Thermomechanics AS CR, Prague, October 22 – 24, 2008.
- [33] V. Tesař, C.H. Hung and W.B. Zimmerman: No-moving-part hybrid-synthetic jet actuator. *Sensors and Actuators A* 125 (2), (2006) 159–169.
- [34] H. Choi: Active control of flows over bluff bodies for drag reduction. In: *6th Symposium on Smart Control of Turbulence*, March 6-9, 2005. National Maritime Research Institute 6-38-1, Shinkawa, Mitaka, Japan.
www.nmri.go.jp/turbulence/PDF/symposium/FY2002/Choi.pdf (cited 17/08/2012).
- [35] M. Ben Chiekh, J.C. Bera, M. Sunyach: Synthetic jet control for flow in a diffuser: vectoring, spreading and mixing enhancement. *J. Turbulence* 4, No. 032 (2003).
- [36] H. Wang, S. Menon: Fuel-air mixing enhancement by synthetic microjets. *AIAA J.* 39 (12) (2001) 2308-2319.
- [37] V. Timchenko, J.A. Reizes, E. Leonardi, F. Stella: Synthetic jet forced convection heat transfer enhancement in micro-channels. In: *Proc. 13th International Heat Transfer Conference IHTC-13*, Sydney, NSW Australia, Aug. 13-18, 2006, Eds. G. de V. Davis and E. Leonardi, MIC-21.
- [38] Z. Trávníček, A.I. Fedorchenko, A.B. Wang: Enhancement of synthetic jets by means of an integrated valve-less pump, Part I: Design of the actuator. *Sensors and Actuators A* 120 (1) (2005) 232–240.

- [39] Z. Trávníček, V. Tesař, A.B. Wang: Enhancement of synthetic jets by means of an integrated valve-less pump, Part II: Numerical and experimental studies. *Sensors and Actuators A* 125 (1) (2005) 50–58.
- [40] Z. Trávníček, T. Vít, V. Tesař: Hybrid synthetic jet as the non-zero-net-mass-flux jet. *Physics of Fluids*, 18 (8) (2006).
- [41] Z. Trávníček, T. Vít: Hybrid synthetic jet intended for enhanced jet impingement heat/mass transfer. In.: *Proc. 13th International Heat Transfer Conference IHTC-13*, Sydney, NSW Australia (2006).
- [42] Z. Trávníček, T. Vít, T. Hyhlík, F. Maršík: Heat/mass transfer of the pulsatile impinging jets. In: *Proc. 5th International Symposium on Turbulence, Heat and Mass Transfer (THMT-5)*, Dubrovnik, Croatia (2006) 437–440.
- [43] D.S. Kercher, J.B. Lee, O. Brand, M.G. Allen, A. Glezer: Microjet cooling devices for thermal management of electronics. *IEEE Trans. Compon. Packaging Technol.* 26 (2), (2003) 359–366.
- [44] Z. Trávníček, V. Tesař: Annular synthetic jet used for impinging flow mass–transfer. *Int. J. Heat Mass Transfer* 46, (2003) 3291–3297.
- [45] Z. Trávníček, J. Vogel, T. Vít, F. Maršík: Flow field and mass transfer experimental and numerical studies of a synthetic impinging jet. In: *Proc. 4th International Conference on Heat Transfer, Fluid Mechanics and Thermodynamics (HEFAT2005)*, Cairo, Egypt, No. ZT4 (2005).
- [46] Z. Trávníček, T. Hyhlík, F. Maršík: Synthetic jet impingement heat/mass transfer (2005), *Journal of Flow Visualization and Image Processing*, Vol. 13, 2006.
- [47] M.B. Gillespie, W.Z. Black, C. Rinehart, A. Glezer: Local convective heat transfer from a constant heat flux flat plate cooled by synthetic air jets. *Trans. ASME, J. Heat Transfer* 128 (2006) 990–1000.
- [48] R. Mahalingam, A. Glezer: An Actively cooled heat sink integrated with synthetic jets. In: *Proc. 35th National Heat Transfer Conference*, Anaheim, California, USA (2001) NHTC 2001-2025.
- [49] A. Olsson, G. Stemme, E. Stemme: A valve-less planar fluid pump with two pump chambers. *Sensors and Actuators A* 46-47 (1995) 549-556.
- [50] Z. Trávníček, V. Tesař: Hybridní syntetizované proudy. In: *Anotace významných výsledků pracovišť AV ČR za rok 2005*, I. Oblast věd o neživé přírodě, 2. sekce aplikované fyziky, 2.16. http://www.cas.cz/anotace_txt.php?ID=89#2.16 (cited 16/03/2006).
- [51] E. Gutmark, Y. Yassour, M. Wolfshtein, Acoustic enhancement of heat transfer in plane channels. *Proceedings of the 7th int. Heat Transfer Conference*, Munchen, Germany, Vol. 3, 1982, MC7, 441-444.
- [52] V. Timchenko, J.A. Reizes, E. Leonardi: An Evaluation of Synthetic Jets for Heat Transfer Enhancement in Air Cooled Micro-Channels. *Int. J. Numer. Methods Heat Fluid Flow*, 17 (3) (2007), 263-283.
- [53] V. Tesař, S. Zhong, Efficiency of synthetic jets generation. *Transactions of the Aeronautical and Astronautical Society of the Republic of China* 35 (1) (2003), 45–53.
- [54] Z. Trávníček: Anulární impaktní proud s akustickým buzením (vizualizace proudového pole a přestup hmoty na obtékané stěně). *Výzkumná zpráva ÚT AV ČR, Z-1310/01* (2002).
- [55] H.H. Bruun: *Hot wire anemometry*. Oxford Univ. Press (1995).
- [56] www.dantecdynamics.com

- [57] F.E. Jørgensen: How to measure turbulence with hot-wire anemometers – a practical guide. Dantec Dynamics (2002).
- [58] L.V. King: On the convection of heat from small cylinders in a stream of fluid: Determination of the convection constants of small platinum wires with applications to hot-wire anemometry. *Phil. Trans. Roy. Soc.*, A214 (1914), 373-432.
- [59] B.G. van der Hegge Zijnen: Modified correlation for the heat transfer by natural and by forced convection from horizontal cylinders. *Appl. Sci. Res*, A6 (1956), 129-140.
- [60] P.D. Richardson: Convection from heated wires at moderate and low Reynolds numbers. *AIAA J.* 3 (1965), 537-538.
- [61] R.M. Fand, K.K. Keswani: A continuous correlation equation for heat transfer from cylinders to air in cross-flow for Reynolds numbers from 10^{-2} to 2×10^5 . *Int. J. Heat Mass Transf.* 15 (1972), 559-562.
- [62] T.W. Davies, M.A. Patrick: A simplified method of improving the accuracy of hot-wire anemometry. *Proc. Conf. on Fluid Dynamic Measurements in the Industrial and Medical Environment*, Leicester University (1972), 152-155.
- [63] M.K. Swaminathan, G.W. Rankin, K. Sridhar: A note on the response equations for hot-wire anemometry. *ASME, J. Fluids Eng.* 108 (1986), 115-118.
- [64] W.K. George, P.D. Beuher, M. Ahmad: Polynomial calibration and quasi-linearization of hot-wires. *Turbulence Research Laboratory Report*, Sunny Buffalo, USA (1981).
- [65] <http://www.ometron.com>
- [66] Portable vibrometer VH-1000-D. User manual, Ometron (2005).
- [67] H. Honji, S. Taneda, M. Tatasuno: Some practical details of the electrolytic precipitation method of flow visualization. *Rep. Res. Inst. Appl. Mech.* 28, Kyushu Univ. (1980), 83.
- [68] T. Vít: An investigation into selected types of flow. Habilitation thesis, Technical university of Liberec (2009).
- [69] FlowManager software and introduction to PIV instrumentation. Software user's guide, Dantec Dynamics (2000).
- [70] M. Kotek: Experimentální studium proudových polí prohozu vzduchového tkacího stroje metodami laserové anemometrie. Ph.D. thesis, Technical university of Liberec (2010), (in Czech language).
- [71] http://en.wikipedia.org/wiki/Helmholtz_resonance (cited 17/08/2012)
- [72] Q. Li, Y.M. Xuan, F. Yu, J. Tan: Experimental investigation of submerged impinging jet using Cu-water nanofluids. In: 14th International Heat Transfer Conference (IHTC14), Washington DC, August 7–13, 2010.
- [73] D. Rylatt, T.S. O' Donovan: Heat transfer to a ducted, semi-confined impinging synthetic air jet. In: 14th International Heat Transfer Conference (IHTC14), Washington DC, August 7–13, 2010.
- [74] R. Fang, W. Jiang, J. Khan, R. Dougal: Experimental heat transfer enhancement in single-phase liquid microchannel cooling with cross-flow synthetic jet. In: 14th International Heat Transfer Conference (IHTC14), Washington DC, August 7–13, 2010.
- [75] J.W. Zhou, L.P. Geng, Y.G. Wang, F.F. Hong: Experimental and numerical study on flow field and heat transfer characteristics for a periodically unsteady impinging jet. In: 14th International Heat Transfer Conference (IHTC14), Washington DC, August 7–13, 2010.

- [76] M. Liu, Ch. Xie, X. Zhang, Y. Chen: Numerical simulation on micromixer based on synthetic jet. *Acta Mech. Sin* 24 (2008), 629-636.
- [77] T. Mautner: Application of the synthetic jet concept to low Reynolds number biosensor microfluidic flows for enhanced mixing: a numerical study using the lattice Boltzmann method. *Biosensors and Bioelectronics* 19 (2004), 1409-1419.
- [78] M. Chaudhari, B. Puranik, A. Agrawal: Heat transfer analysis in a rectangular duct without and with cross-flow and an impinging synthetic jet. *IEEE Transactions on Components and Packaging Technologies*, Vol. 33 (2010), 488-497.
- [79] D.I.R. Raichel: *The science and applications of acoustics*. Springer-Verlag, New York (2000).
- [80] R.K. Shah, A.L. London: *Laminar flow forced convection in ducts*. Academic press, Inc. New York (1978).
- [81] D.B. Holmes, J.R. Vermeulen: Velocity profiles in ducts with rectangular cross sections. *Chemical Engineering Science*, Vol. 23 (1968), 717-722.
- [82] M. Spiga, G.L. Morini: A symmetric solution for velocity profile in laminar flow through rectangular ducts. *International Communications in Heat and Mass Transfer*, Vol. 21, No. 4 (1994), 469-475.
- [83] M.S. Elbisy, H.A. Ghulman: Flow velocity profiles distribution in the entrance region of straight rectangular duct. *Canadian Journal on Mechanical Sciences & Engineering*, Vol. 2, No. 5 (2011), 111-115.
- [84] R.D. James, J.W. Jacobs, A. Glezer: A round turbulent jet produced by an oscillating diaphragm. *Phys. Fluids*, Vol. 8, No. 9 (1996), 2484-2495.
- [85] Z. Trávníček, F. Maršík, T. Vít, P. de Boer: Synthetic jets actuation at the resonance frequency. *IUTAM – 21st ICTAM*, Warsaw (2004).
- [86] Z. Trávníček, T. Vít, P. de Boer, F. Maršík: Synthetic jets – design and verification of the actuator. *Conference Topical Problems of Fluid Mechanics 2004*, Prague, February 25, 2004, 165-168.
- [87] V. Timchenko, J. Reizes, E. Leonardi: Heat transfer enhancement in micro-channels by synthetic jets. *4th International Conference on Computational Heat and Mass Transfer*, Paris-Cachan, May 17-20, 2005, 471-476.
- [88] V. Timchenko, J. Reizes, E. Leonardi, G. de Vahl Davis: A criterion for the formation of micro synthetic jets. *2004 ASME International Mechanical Engineering Congress and Exposition*, Anaheim, California USA, November 13-20, 2004, 197-203.
- [89] H. Schlichting, K. Gersten: *Boundary-Layer Theory*. Springer-Verlag, Berlin, 2000.
- [90] M. Gordon, J. Soria, PIV measurements of a zero-net-mass-flux jet in cross flow. *Exp. Fluids* 33 (6) (2002) 863 - 872.
- [91] M. Gordon, J.E. Carter, J. Soria: Investigation of the mean passive scalar field in zero-net-mass-flux jets in cross-flow using planar-laser-induced fluorescence. *Phys. of Fluid* 16 (3) (2004) 794-808.
- [92] A. Eroglu, R.E. Breidenthal: Structure, penetration, and mixing of pulsed jets in crossflow. *AIAA Journal* 39 (3) (2011) 417-423.
- [93] Z.U. Khan, J.P. Johnston: On vortex generating jets. *Int. Journal of Heat and Fluid Flow* 21(2000) 506-511.

- [94] A.C.H. Lai, J.H.W. Lee: Multiple tandem jet interaction in a crossflow. 9th Int. Conference on Hydrodynamics, Shanghai, China, October 11-15, 2010, 639-643.
- [95] R. Holman, Y. Utturkar, R. Mittal, B.L. Smith, L. Cattafesta, Formation criterion for synthetic jets. *AIAA Journal* 43 (10) (2005) 2110-2116.
- [96] C.Y. Lee, D.B. Goldstein, Two-dimensional synthetic jet simulation, *AIAA J.* 40 (3) (2002) 510-516.
- [97] S.G. Mallinson, J.A. Reizes, G. Hong, An experimental and numerical study of synthetic jet flow, *The Aeronautical Journal* 105 (1043) (2001) 41–49.
- [98] B.L. Smith, G.W. Swift, A comparison between synthetic jets and continuous jets, *Exp. Fluids* 34 (2003) 467–472.
- [99] Q. Gallas, R. Holman, T. Nishida, B. Carroll, M. Sheplak, L. Cattafesta, Lumped element modeling of piezoelectric-driven synthetic jet actuators, *AIAA Journal* 41 (2) (2003) 240–247.
- [100] J.L. Gilarranz, L.W. Traub, O.K. Rediniotis, A new class of synthetic jet actuators—Part I: Design, fabrication and bench top characterization. *J. Fluids Eng.-Trans. ASME* 127 (2005) 367-376.
- [101] D.A. Tamburello, M. Amitay, Interaction of a free jet with a perpendicular control jet. *J. Turbul.* 8 (21) (2007) 1–27.
- [102] J. Tensi, I. Boué, F. Paillé, G. Dury, Modification of the wake behind a circular cylinder by using synthetic jets, *Journal of Visualization* 5 (1) (2002) 37–44.
- [103] R. Mahalingam, N. Rumigny, A. Glezer, Thermal management using synthetic jet ejectors. *IEEE Transactions on Components and Packaging Technologies* 27 (3) (2004) 439–444.
- [104] J. Garg, M. Arik, S. Weaver, T. Wetzel, S. Saddoughi, Advanced localized air cooling with synthetic jets, *ASME Journal of Electronics Packaging* 127 (2005) 503–511.

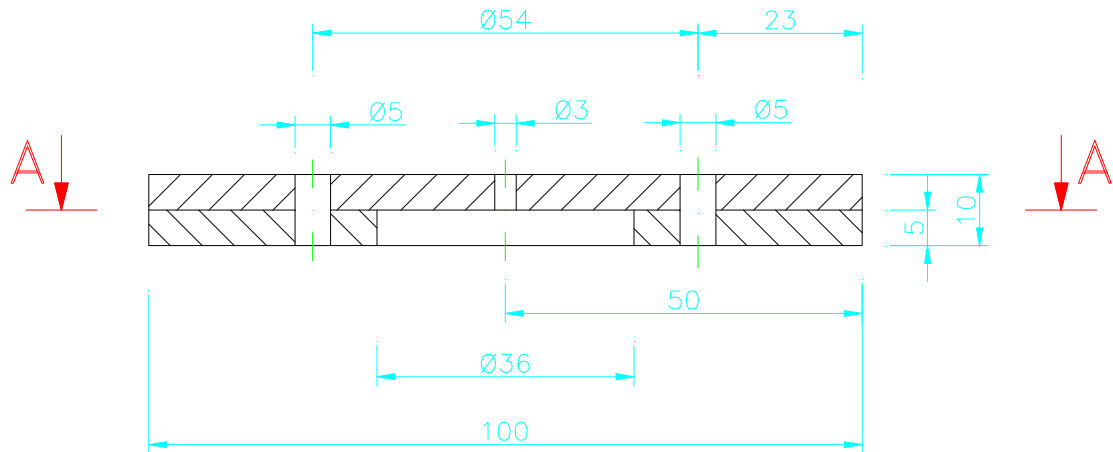
PUBLICATIONS OF AUTHOR

- [A1] T. Vít, P. Dančová: Použití různých experimentálních metod pro analýzu proudění typu "Synthetic Jet". XXIV mezinárodní vědecká konference kateder a pracovišť mech. tek. a termomech., Blansko (2005).
- [A2] P. Dančová: Studie proudění typu "Synthetic Jet" (Analysis of the "Synthetic Jet"). Diplomová práce, TUL (2006), in Czech.
- [A3] P. Dančová, T. Vít: Analysis of the "Synthetic Jet" in the water. Int. conference Experimental Fluid Mechanics 2006, TUL, Liberec (2006) 44-50.
- [A4] P. Dančová, T. Vít, Z. Trávníček: Analysis of SJ Piezo-Ceramic Pulsation Generator. Conf.: Developments in Machinery Design and Control, Slovensko, (2007) 15-16, full text CD.
- [A5] P. Dančová, Z. Trávníček, T. Vít: Synthetic jet. Conf.: Engineering mechanics 2007, Svratka (2007) 35-36, full text CD.
- [A6] P. Dančová, T. Vít, Z. Trávníček: The Piezoceramic Generator for SJ. International Conference „XXVI. Setkání kateder mechaniky tekutin a termomechaniky“, Herbertov (2007) 19-20, full text CD.
- [A7] M. Kotek, P. Dančová: Influence of the temperature on the critical Reynolds number for the laminar vortex shedding. Int. conference Experimental Fluid Mechanics 2007, TUL, Liberec (2007) 52-56.
- [A8] T. Vít, P. Dančová, Z. Trávníček: Syntetizovaný proud (Synthetic Jet). MM Průmyslové spektrum, č.3/2007, (2007) 104-106.
- [A9] P. Dančová, T. Vít: Numerical simulation of Heat Transfer of Synthetic Jet. International conference „XXVII. Setkání kateder mechaniky tekutin a termomechaniky“, Plzeň (2008) 61-66.
- [A10] P. Dančová, H.C. de Lange, Z. Trávníček, T. Vít: PIV Measurements of a Synthetic Jet in a Channel Flow. 12th International Conference: Developments in Machinery Design and Control, Nowogród, Poland (2008) 23-24, full text CD.
- [A11] P. Dančová, T. Vít: Analysis of the Synthetic Jet. Journal of Applied Science in the Thermodynamics and Fluid Mechanics (JASTFM), 1st issue 2008 (2008) (web version).
- [A12] P. Dančová, T. Vít: Analysis of the Synthetic Jet. Journal of Applied Science in the Thermodynamics and Fluid Mechanics (JASTFM), 2nd issue 2009 (2009) 11-18.
- [A13] P. Dančová, H.C. de Lange, T. Vít, D. Šponiar, Z. Trávníček: A laminar channel flow effected by Synthetic Jet – Experimental and numerical studies. International conference ExHFT-7, Krakow, Poland (2009) 75-76, full text CD.
- [A14] P. Dančová, H.C. de Lange, T. Vít, D. Šponiar, Z. Trávníček: A Channel Flow controlled by a Synthetic Jet Array. International conference THMT - 09, Roma, Italy (2009) 935-938, full text CD.
- [A15] P. Dančová, T. Vít: Numerical simulation of a channel flow affected by a synthetic jet. International Scientific - Practical Conference "Computer Aided Industrial Design Training for Ukrainian Engineers", Kyeu, Ukraine (2009).

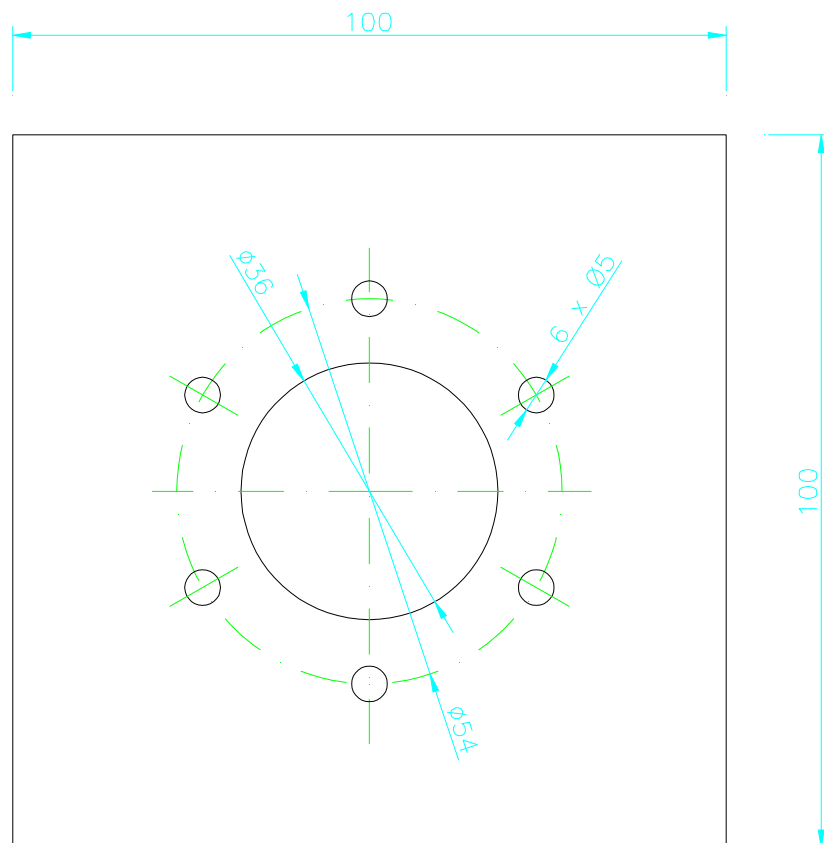
- [A16]Z. Trávníček, P. Dančová, T. Vít: Visualization and heat/mass transfer study of laminar channel flow controlled by synthetic jet array. The 7th Pacific Symposium on Flow Visualization and Image Processing, Nov. 16-19, 2009 Kaohsiung, Taiwan, R.O.C. (2009).
- [A17]V. Dvořák, P. Dančová: Experimental investigation into flow in an ejector with perpendicular synthetic jet. Int. conference Experimental Fluid Mechanics 2009, TUL, Liberec (2009), 44-51.
- [A18]Z. Trávníček, P. Dančová, J. Kordík, T. Vít, M. Pavelka: Heat and mass transfer caused by a laminar channel flow equipped with a synthetic jet array. 14th International Heat Transfer Conference (IHTC14), Washington DC, August 7–13, 2010.
- [A19]P. Dančová, T. Vít, M. Kotek: PIV measurement of synthetic jet array. 24th symposium on anemometry, Holany – Litice, 1.-2.6.2010.
- [A20]P. Dančová, Z. Trávníček: Behavior of piezoceramic transducer for synthetic jet array. Setkání kateder mechaniky tekutin a termomechaniky - mezinárodní konference /29/. Rožnov pod Radhoštěm (CZ), 23.06.2010-25.06.2010.
- [A21]V. Dvořák, P. Dančová, P. Švarc: Experimental investigation into flow in an ejector with four synthetic jets. Int. conference Experimental Fluid Mechanics 2010, TUL, Liberec (2010), Volume 1, 107-114.
- [A22]P. Dančová, T. Vít, M. Kotek: Experimental investigation of synthetic jet array. Engineering Mechanics 2011, Svratka 9. - 12. May 2011. pp 439-442. ISBN 978-80-87012-33-8.
- [A23]P. Dančová, Z. Trávníček, T. Vít, M. Kotek: A channel flow affected by a synthetic jet array – an experimental study. 2nd International Conference on Fluid Mechanics and Heat and MassTransfer 2011, Corfu, Greece, July 14-16, 2011, ISBN 978-161804-020-6.
- [A24]V. Dvořák, P. Dančová: An investigation into air ejector with pulsating primary flow. 7th World Academy of Science, Engineering and Technology, Singapore, September 2011, ISSN 2010-376X.
- [A25]V. Dvořák, P. Dančová: Processes in an air ejector with pulsating primary flow. 4th International Meeting on Advances in Thermofluids, Melaka, Malaysia, 2011, ISBN 978-967-0194-07-3.
- [A26]Z. Trávníček, P. Dančová, J.H. Lam, V. Timchenko, J. Reizes: Numerical and experimental studies of a channel flow with multiple circular synthetic jets. International Conference Experimentsal Fluid Mechanics 2011, Jičín, Czech Republic, November 22-25, 2011, ISBN 978-80-7372-784-0.
- [A27]P. Dančová, T. Vít, Z. Trávníček, V. Lédl: Measurement of temperature fields in fluids. 7th International Symposium on Turbulence, Heat and Mass Transfer, Palermo, Italy (2012), in preparation.

APPENDIX 1

DIMENSIONS OF A SYNTHETIC JET ACTUATOR

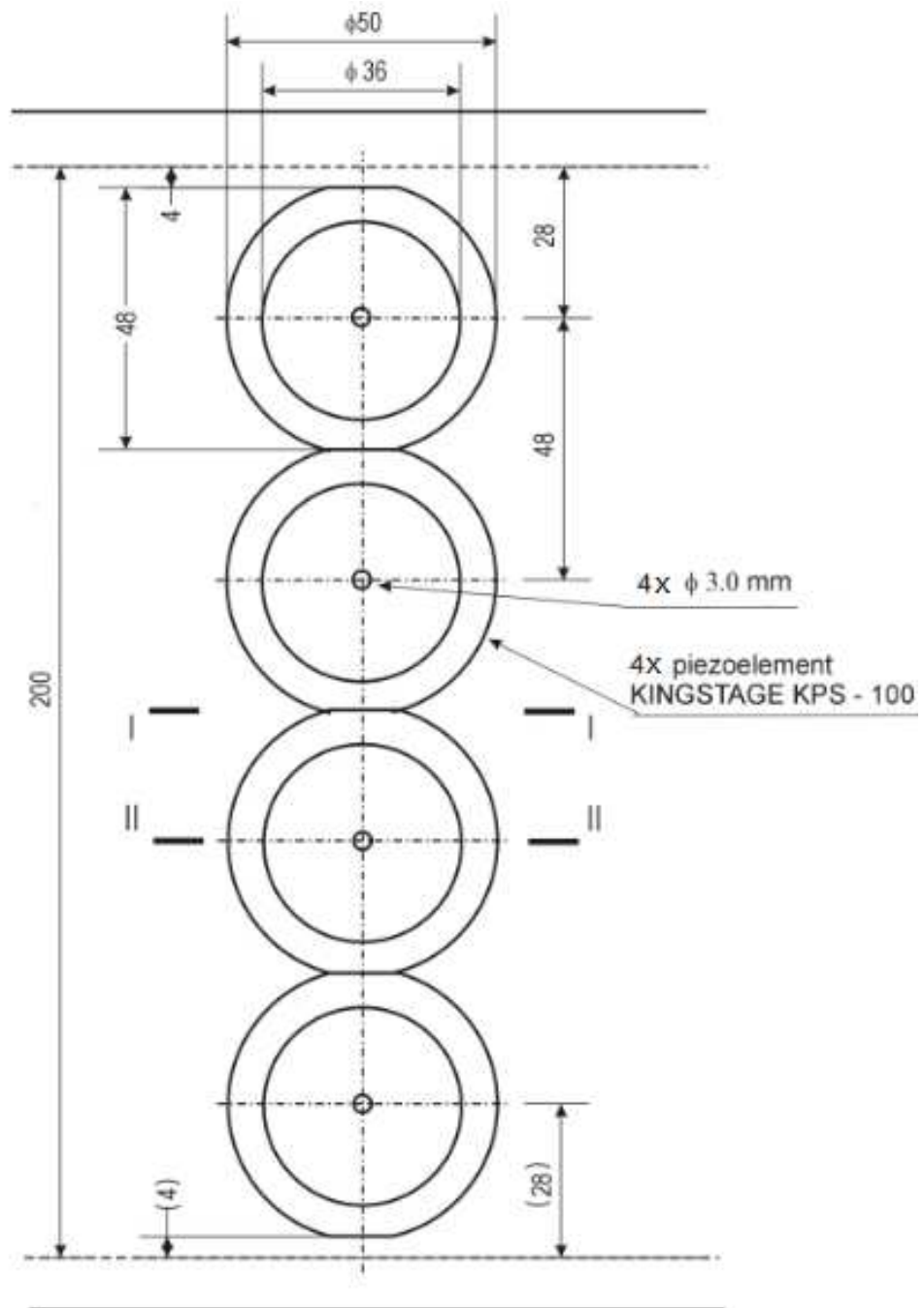


A - A



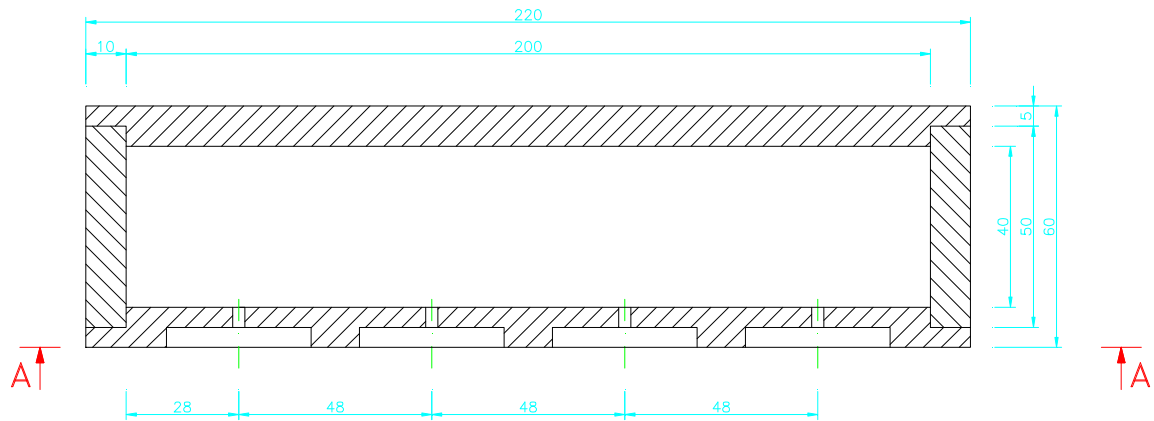
APPENDIX 2

DIMENSIONS OF A SYNTHETIC JET ARRAY

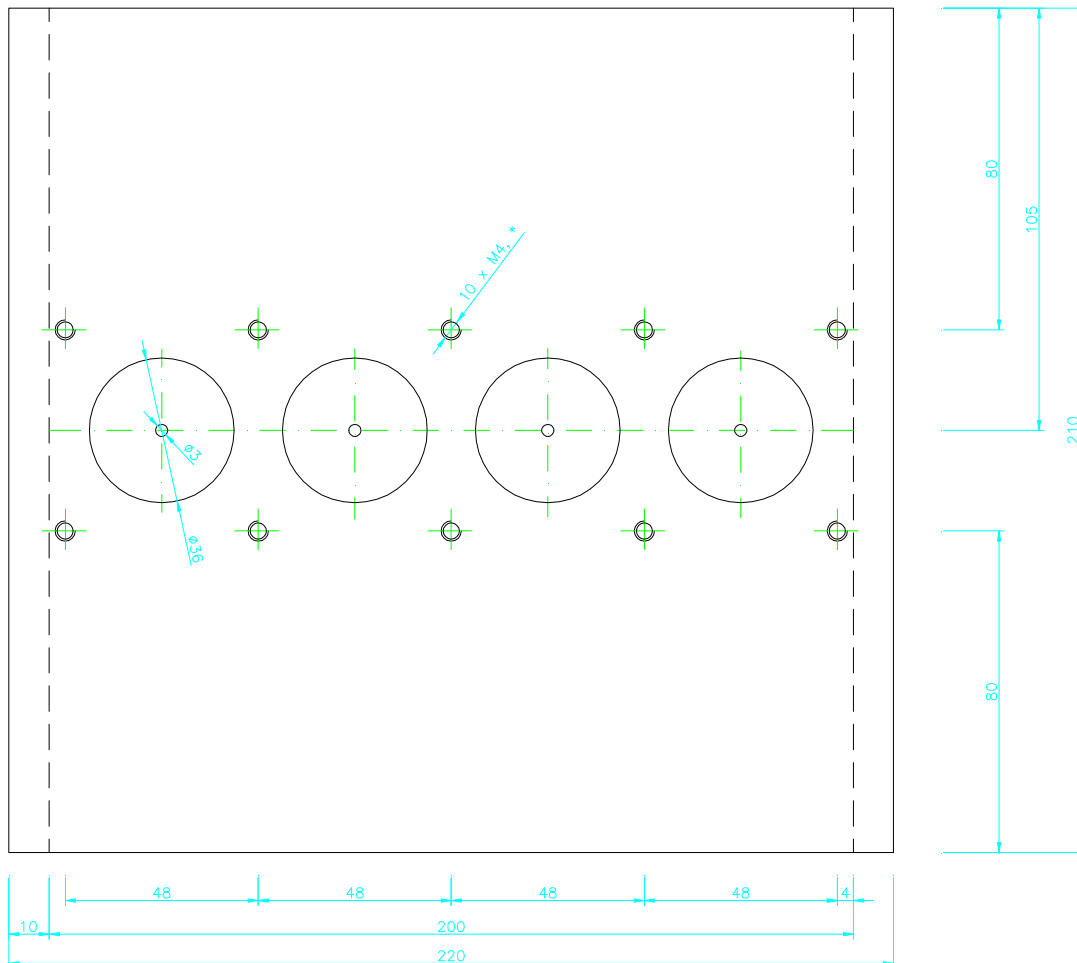


APPENDIX 3

DIMENSIONS OF A SYNTHETIC JET ARRAY EQUIPMENT



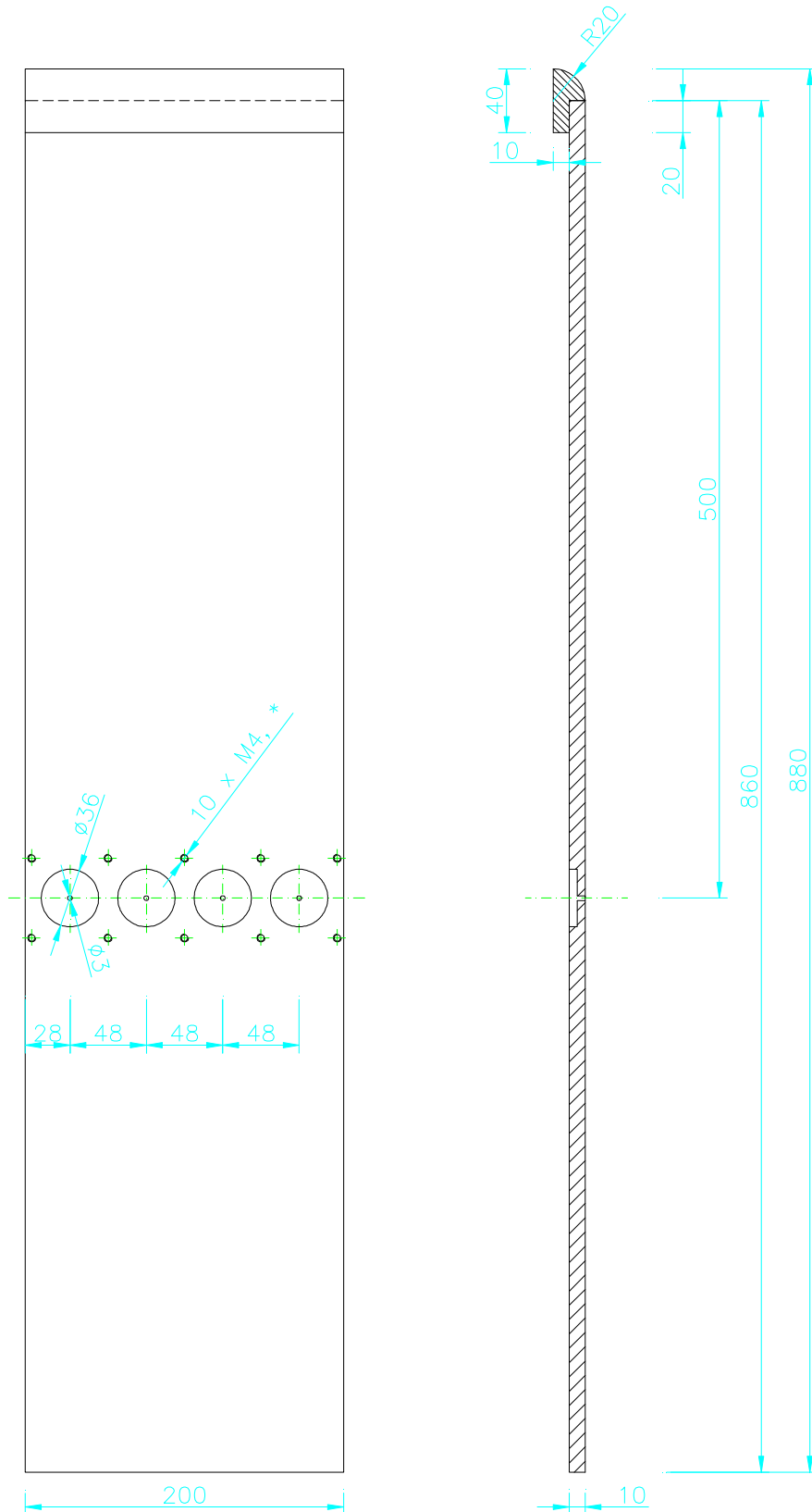
A-A



* length of the screw into plexi max 7mm

APPENDIX 4

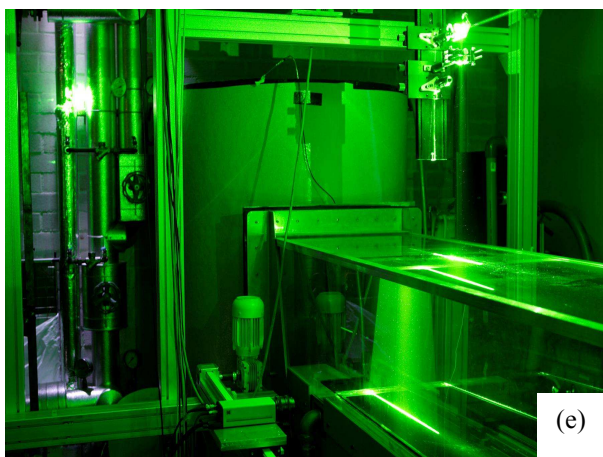
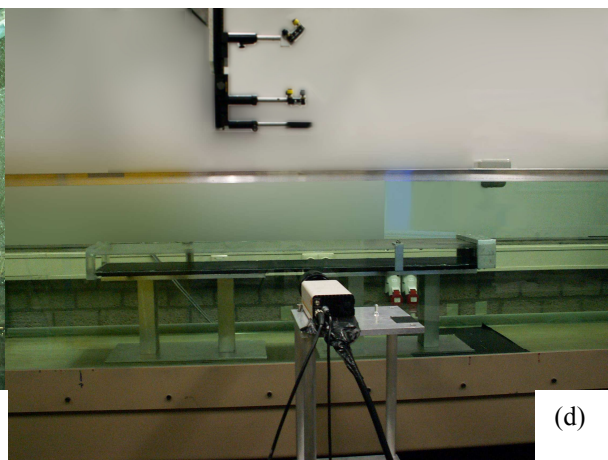
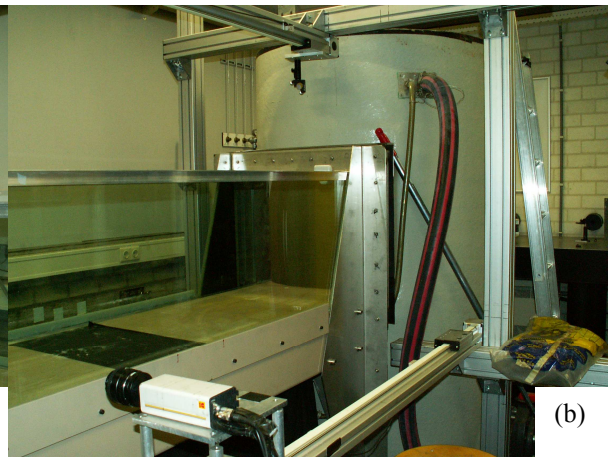
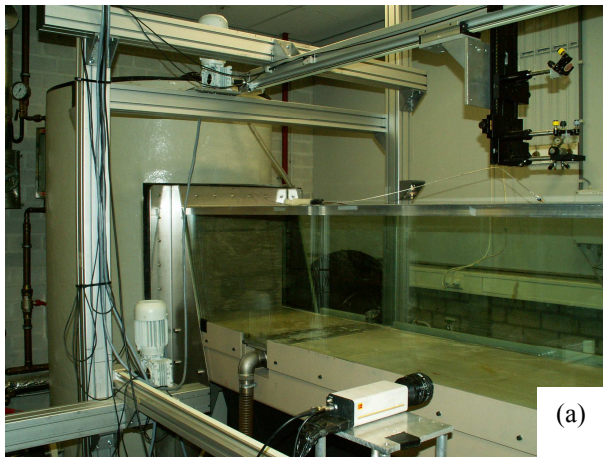
DIMENSIONS OF A PLEXIGLASS WALL



* length of the screw into plexi max 7mm

APPENDIX 5

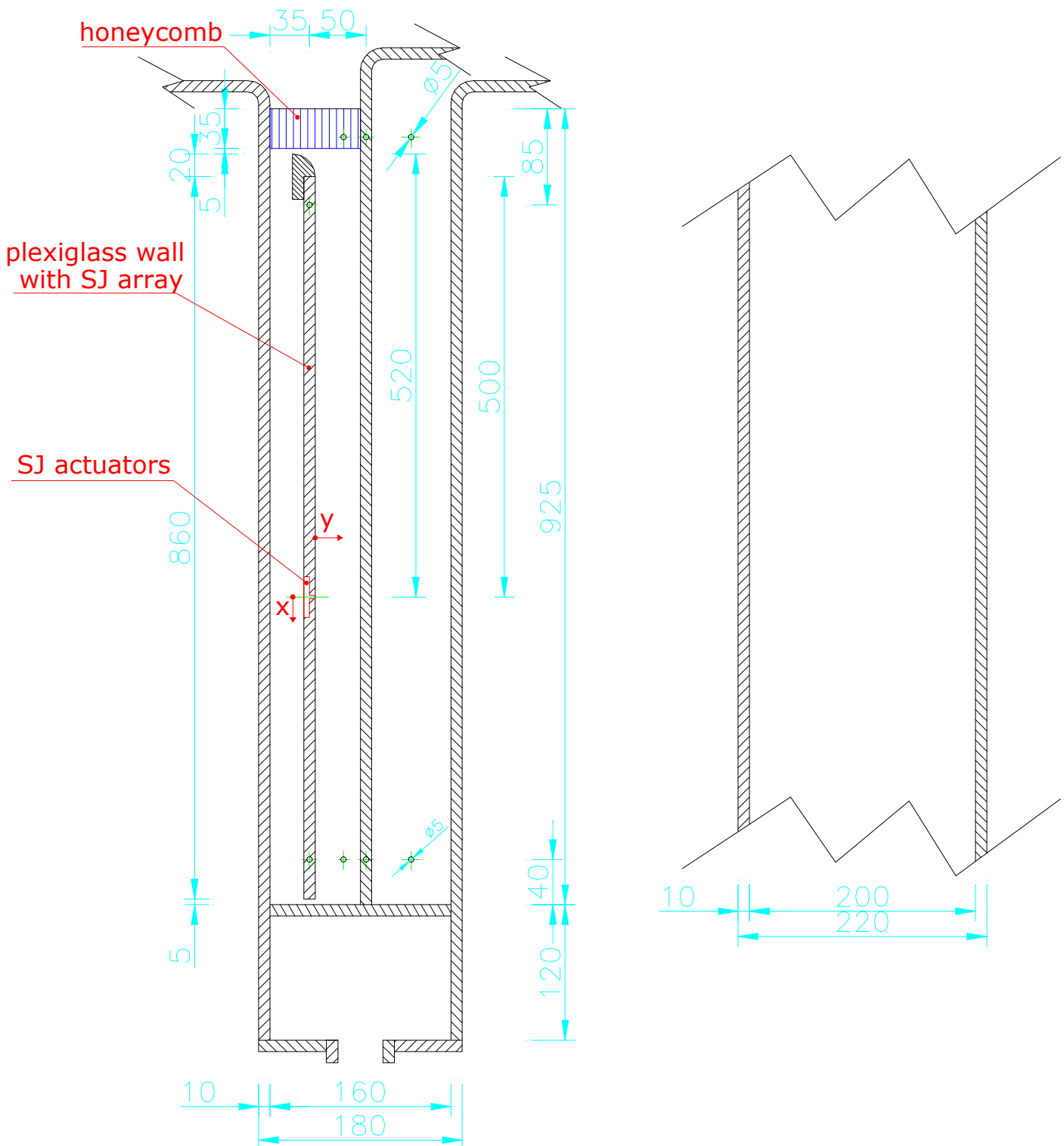
WATER CHANNEL AT TU EINDHOVEN



- (a) view on the water channel left side
- (b) view on the water channel right side
- (c) view from the channel inside
- (d) tested channel with aluminium bench inside water channel, camera, mirrors and lenses for PIV measurement
- (e) water channel with laser, PIV measurement

APPENDIX 6

DIMENSIONS OF WATER CHANNEL AT IT CAS



APPENDIX 7

TOWING TANK AT TU LIBEREC

Towing tank at TU Liberec



Detailed view on traverse system with motor



Detailed view on traverse motor

APPENDIX 8

PCT STIFFNES INVESTIGATION

To derive the natural frequency of SJ actuator, it is necessary to know the stiffness k_p of the PCT membrane, which is defined as:

$$k_p = \frac{p}{z} \quad (\text{A8.1}),$$

where p is static pressure [Pa] and z is membrane deflection [m].

Static pressure is measured with use of a water column, which places a load on the PCT membrane, defined as:

$$p = \rho g y \quad (\text{A8.2}),$$

where $\rho = 1000$ [kg/m³] is water density, $g = 9.81$ [m/s²] is gravity acceleration, and y is the water level height [m].

The experimental setup is shown in Figure F1; for the setup drawing, see Figure F2. Measurement of membrane stiffness is described in Table T1. In the measured range of loads, the setup can be considered as linear. Therefore, the stiffness is represented by the average of the measured values. The results of a numerical simulation of PCT membrane deflection are shown in Graph G1. Equation (1.24) from Chapter 1 is used for natural frequency calculation:

$$f = \frac{1}{2\pi \cdot C} \frac{D}{D_m} \sqrt{\frac{k_p}{\rho L_e}} \quad (1.29),$$

where C is a constant, which is influenced by a deformed membrane shape. D and D_m are orifice diameter and membrane diameter, respectively. L_e is a so-called “equivalent length”, defined in Equation (1.24), Chapter 1. The constant C is calculated from the results of the numerical simulation in Graph G1, [A4]. After substituting, $k_p = 4139443 \text{ N/m}^3$, $L_e = 0.00755 \text{ m}$, $(D/D_m) = (0.003/0.044)$ and $C = 0.41$, the natural frequency is calculated as $f = 19.7 \text{ Hz}$. For smaller deflections, i.e. for a smaller $k_p = 1.962 \cdot 10^6 \text{ N/m}^3$, Eq. (1.29) gives a smaller value of $f \approx 13.5 \text{ Hz}$. The experimental value of 15Hz is between these.

Table T1 Experimental results of PCT membrane stiffness

Water level height y [m]	Pressure p [Pa]	Max. membrane deflection z [mm]	PCT stiffness k_p [N/m ³]
0	0	0.191	
0.041	402	0.205	1962000
0.088	863	0.230	3753391
0.139	1364	0.274	4976606
0.174	1707	0.291	5865773
Average value			4139443
Mean-root-square deviation			1463844

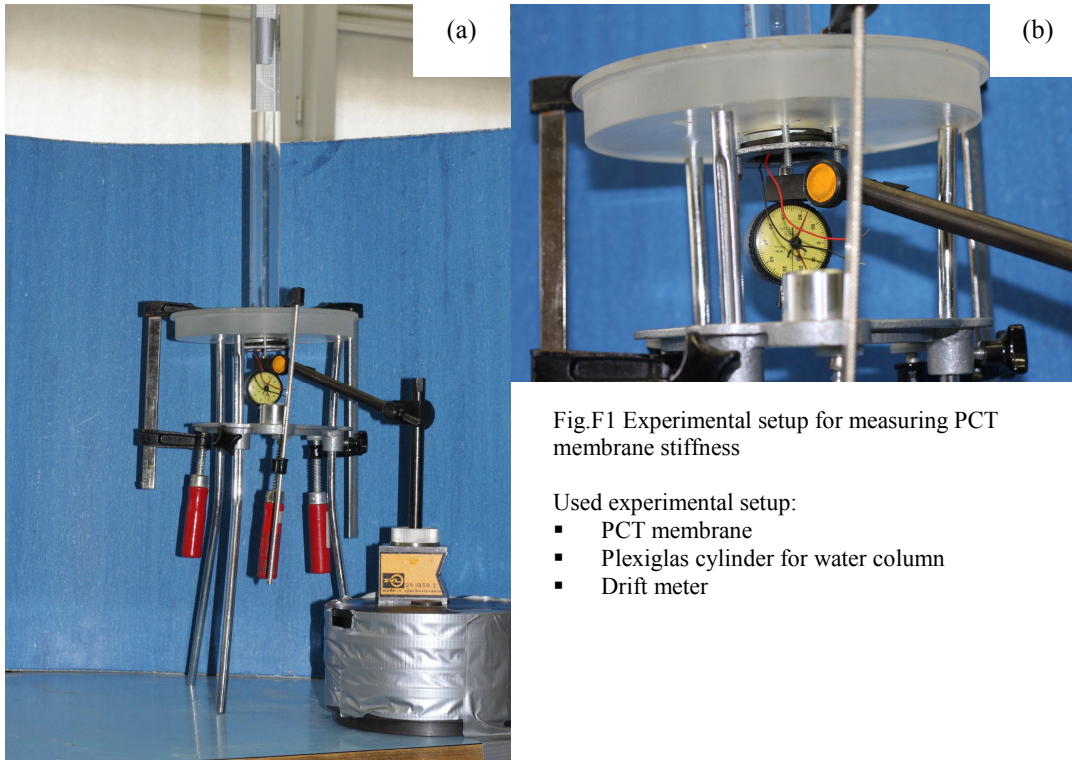
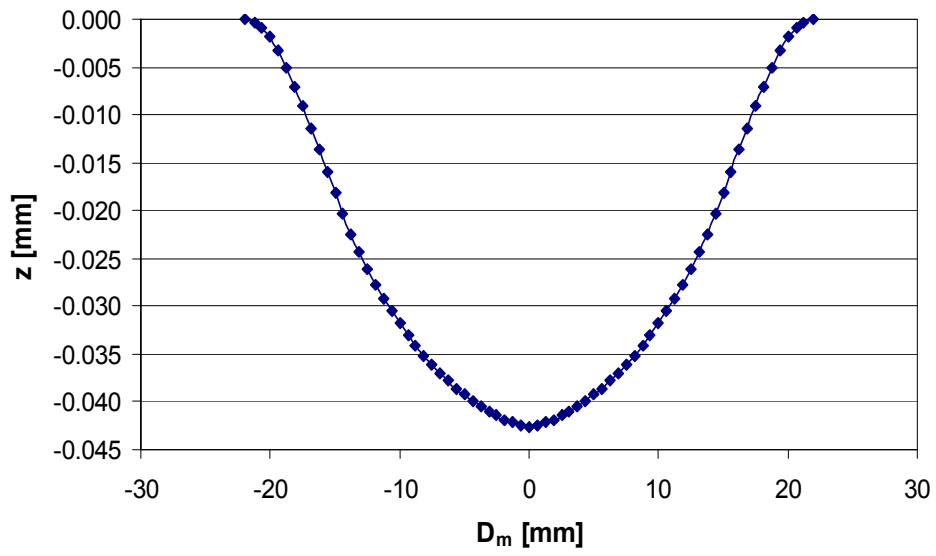


Fig.F1 Experimental setup for measuring PCT membrane stiffness

Used experimental setup:

- PCT membrane
- Plexiglas cylinder for water column
- Drift meter



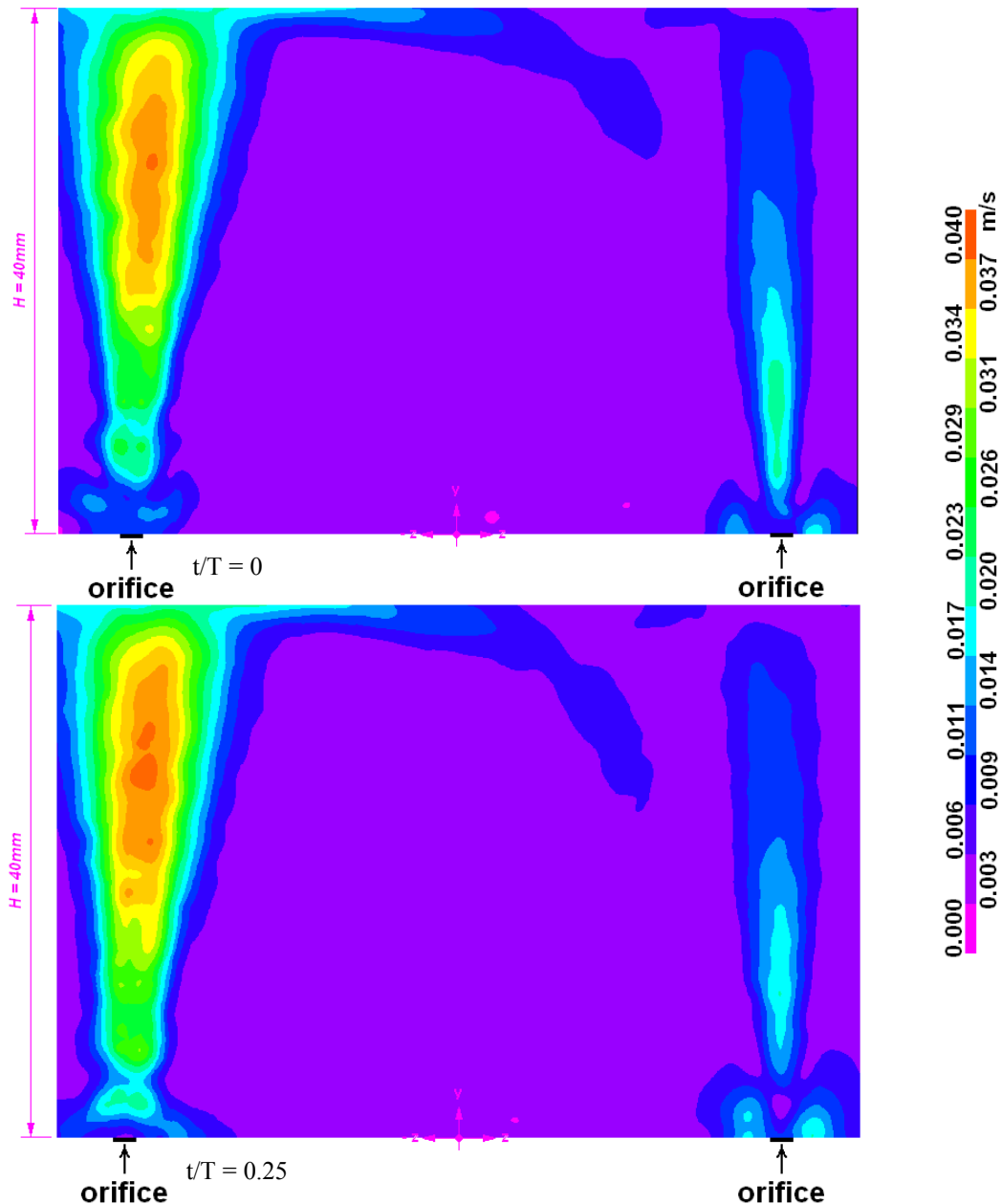
Graph G1 Result of numerical simulation of PCT membrane deflection, [A4]

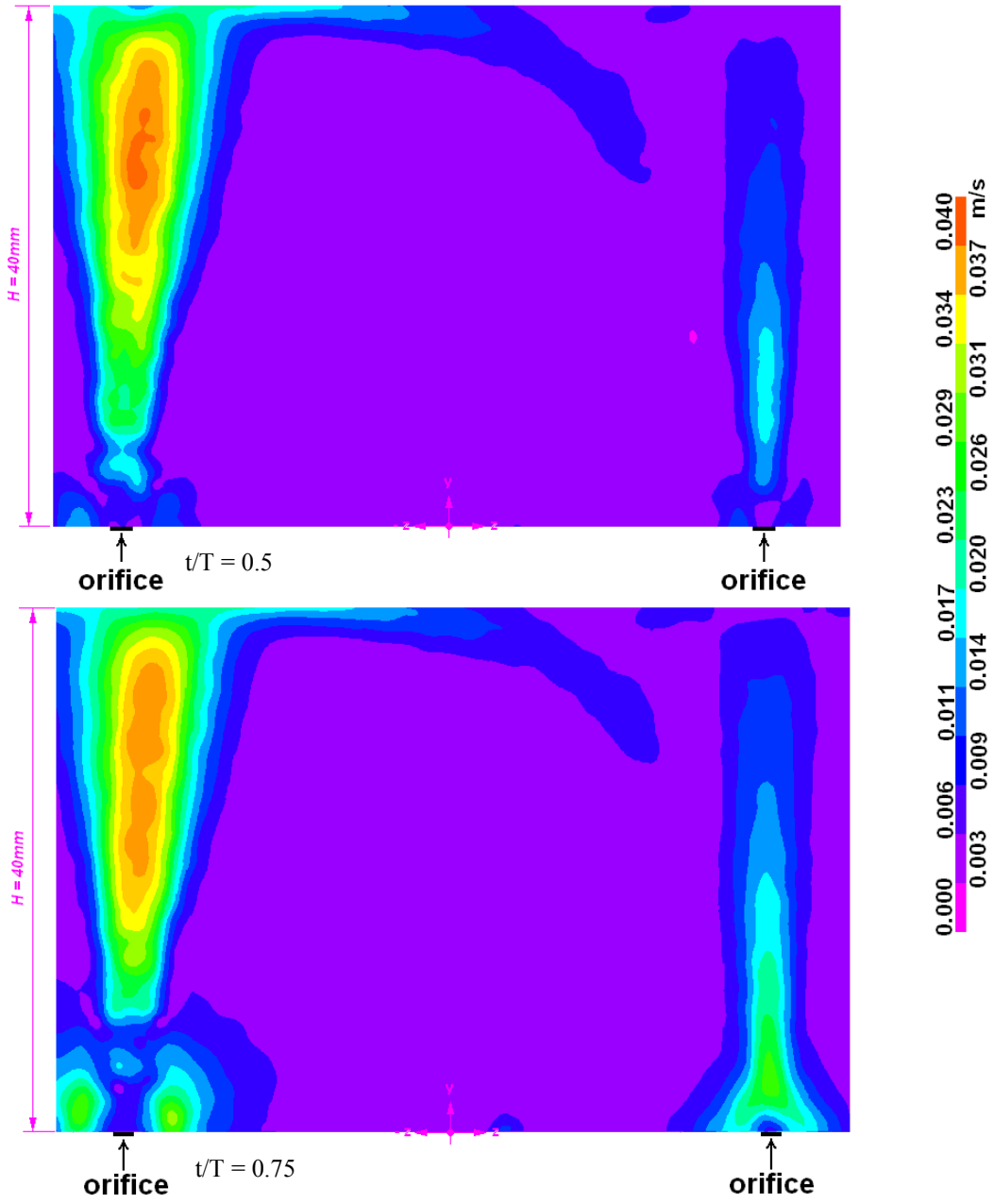
APPENDIX 9

PIV EXPERIMENTS OF UNSELECTED PCTs

These figures show PIV measurement of a SJ array with unselected PCTs at different times during the period. The monitored plane was aligned to the collective centerline of all orifices. Measurement was focused on the two middle orifices. The typical delay time between two pulses was 5 ms to achieve maximum particle displacement of (5-6) pixels. The outlet velocity from the SJ orifice was determined to be 6 cm/s. These (5-6) pixels correspond to the orifice velocity recorded with the relevant scale factor.

The results are presented in the form of velocity magnitude contours. It is evident that PCTs work with phase shift and at different power levels.



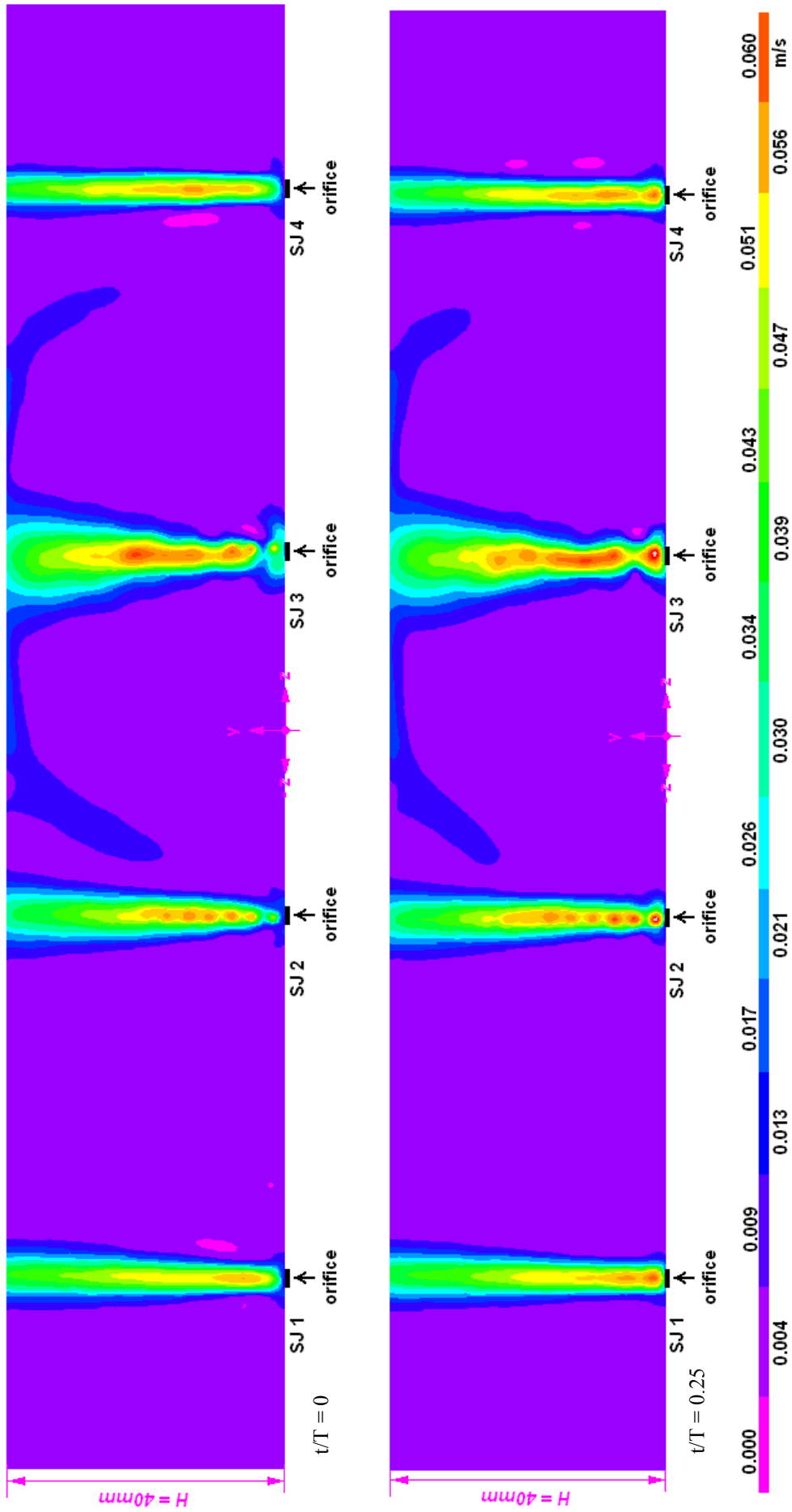


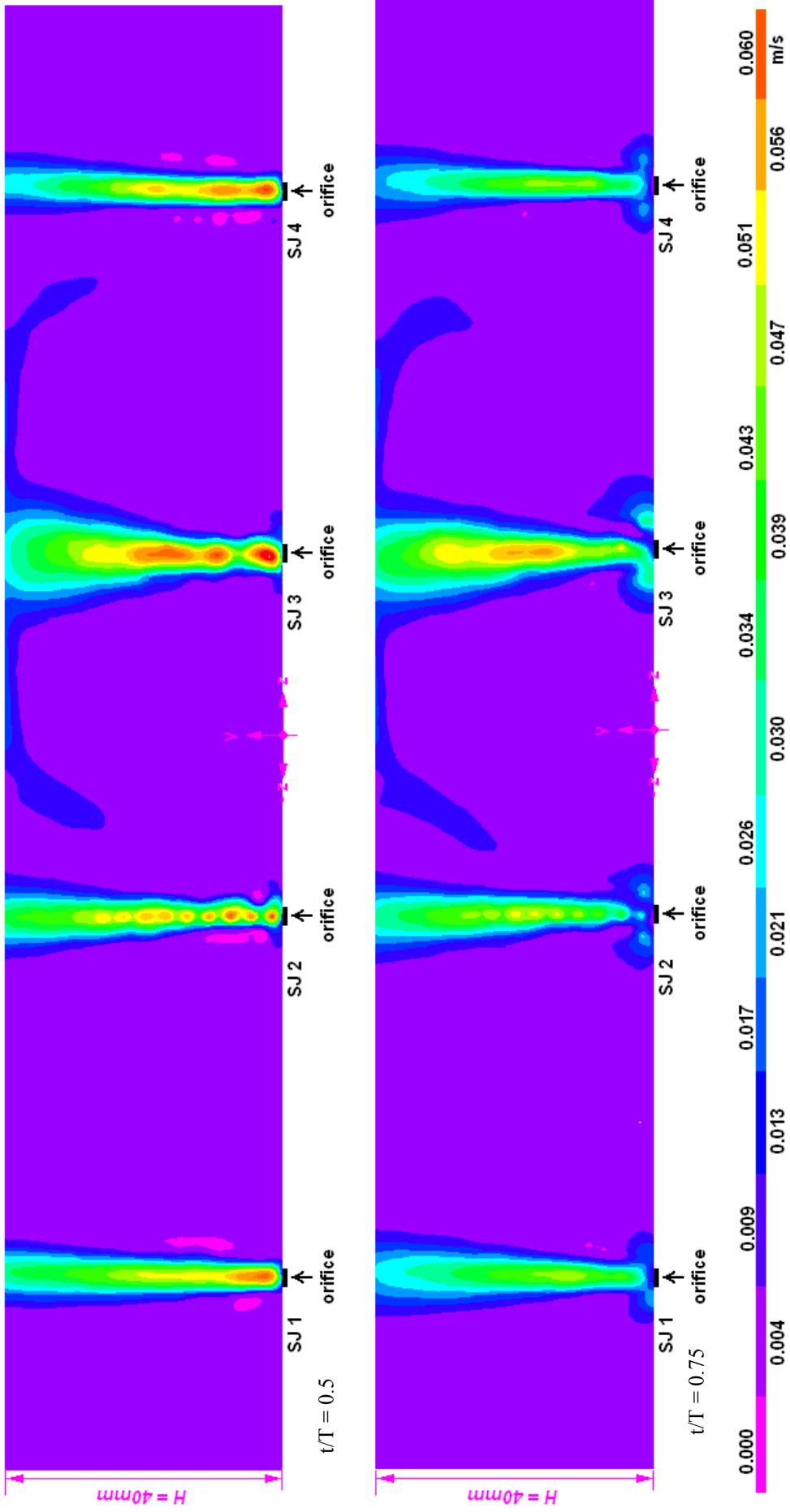
APPENDIX 10

EXPERIMENTS OF SELECTED PCTs – DIFFERENT POWER OF ACTUATORS

PIV experiments of SJ array with the equipment upper wall

Figures show PIV result of SJ array in different time during the period. There is visible that PCTs work in same phase (i.e. without phase shift), but SJ 3 has higher power than the other three.





APPENDIX 11

PROGRAM IN MATLAB FOR COMPOSING OF PICTURES RECORDED WITH TWO CAMERAS DURING PIV MEASUREMENT

```
% clear all;close all;clc;

global TempInput;
global TempDataset;
global Output;
Output.type = 'image';
Output.name = 'Spojeni';

pocetsnimku=size(Input{1,1}.dataset);

Output.timeBtwPulses=Input{1,1}.timeBtwPulses;
Output.pixelPitch=Input{1,1}.pixelPitch;
Output.scaleFactor=Input{1,1}.scaleFactor;
Output.pixelDepth=double(Input{1,1}.pixelDepth);
Output.sensorSize=Input{1,1}.sensorSize;
Output.cameraName=Input{1,1}.cameraName;
Output.cameraIndex=Input{1,1}.cameraIndex;
Output.gridSize=Input{1,1}.gridSize;
Output.imageOffset=Input{1,1}.imageOffset;
Output.imageSize=Input{1,1}.imageSize;
Output.startTime=Input{1,1}.startTime;
Output.datasetCount=Input{1,1}.datasetCount;
Output.fromMethod=Input{1,1}.fromMethod;
Output.dataType=Input{1,1}.dataType;

for i=1:1:pocetsnimku(2)

Leva1=Input{1,1}.dataset(1,i).frame1;
Leva2=Input{1,1}.dataset(1,i).frame2;
Prava1=Input{1,2}.dataset(1,i).frame1;
Prava2=Input{1,2}.dataset(1,i).frame2;

yT1=905;%vzdalenost horniho okraje
yD1=415;%vzdalenost dolniho okraje
xL1=0;%vzdalenost leveho okraje
xR1=123;%vzdalenost praveho okraje
yT2=905;%vzdalenost horniho okraje
yD2=415;%vzdalenost dolniho okraje
xL2=44;%vzdalenost leveho okraje
xR2=0;%vzdalenost praveho okraje
```

```

%spojeni prava leva.....
x=1; %x-ova druhy index
y=1;
%for yy=170:1:625
for yy=(1025-yT1):1:(1024-yD1)    %zvlastni prepocet
    for xx=1+xL1:1:1280-xR1
        Spojeni1(y,x)=Leva1(yy,xx);
        Spojeni2(y,x)=Leva2(yy,xx);
        x=x+1;
    end
    x=1;
    y=y+1;
end

x=1280-xL1-xR1;
y=1;

for xx=1+xL2:1:1280-xR2
%   for yy=165:1:620
    for yy=(1025-yT2):1:(1024-yD2)
        Spojeni1(y,x)=Prava1(yy,xx);
        Spojeni2(y,x)=Prava2(yy,xx);
        y=y+1;
    end
    y=1;
    x=x+1;
end

....zapis dat.....
Output.dataset(1,i).index = i;
Output.dataset(1,i).timeStamp = 250*(i-1);
Output.dataset(1,i).frame1 = Spojeni1;
Output.dataset(1,i).frame2 = Spojeni2;
end

```